

Superhydrophobic Properties of Replicated Laser Microtextured Surfaces

A Dissertation

Presented to

the faculty of the School of Engineering and Applied Science

University of Virginia

in partial fulfillment

of the requirements for the degree

Doctor of Philosophy

by

Paul O. Caffrey

August

2015

APPROVAL SHEET

The dissertation
is submitted in partial fulfillment of the requirements
for the degree of
Doctor of Philosophy



AUTHOR

The dissertation has been read and approved by the examining committee:

Mool C. Gupta

Advisor

Robert M. Weikle

Tatiana Globus

Archie Holmes

Eric Loth

Accepted for the School of Engineering and Applied Science:



Dean, School of Engineering and Applied Science

August
2015

Copyright © 2015 by Paul O. Caffrey
All rights reserved

To my family. Thanks for waiting, let's have that vacation!

Abstract

The fields of anti-icing technology, aviation, solar energy, wind energy, various corrosion susceptible systems and EMI shielding etc. would greatly benefit with the development of superhydrophobic surfaces and materials. Consequently, the synthesis, fabrication and characterization of superhydrophobic coatings and materials have seen rapid expansion recently. It is difficult to obtain a water contact angle greater than 150° and a sliding angle of less than 10° (superhydrophobic surfaces) through surface treatments, by the application of environmentally stable chemical coatings or by choice of materials. However, the combination of hydrophobic material properties with surface roughness at micro/nano scale could provide very high water contact angles typically greater than 160 degrees.

In this dissertation a laser processing method is investigated to generate a microtextured surface that is then replicated on a polymer surface (PDMS). This replicated microtextured surface is then characterized for its optical and superhydrophobic properties. No additional coatings on the polymer are necessary to deliver contact angles greater than 161° . Multiwall Carbon nanotubes are then added to the polymer matrix to produce an electrically conductive nanomaterial with microtexture surface roughness and this resulting conductive nanocomposite is characterized for its superhydrophobic properties and its electrical resistivity. The electrical conductivity was controlled by changing the amount of MWCNT that is added to the polymer matrix. A conductivity improvement over pure PDMS of more than 10^{11} is found with a resistivity of $\rho = 761 \Omega \text{ cm}$. Both the microtextured PDMS and conducting nanocomposite were investigated for electrowetting control of contact angle and it was discovered that reversible electrowetting can be demonstrated in the Cassie-Baxter region of more than ten degrees with no additional oil or other surface treatments. These replicated microtextured polymer surfaces have great potential for various commercial applications that require water repellency for anti-icing, corrosion protection and others.

Acknowledgments

I would like to thank my advisor, Dr. Mool C. Gupta for his help, guidance and patience in pursuing my Ph.D. This work would not have been possible without the ongoing support of the post-doctoral research associates in the research group namely Dr. B.K. Nayak and Dr. Sharad Bhagat.

I would also like to thank my fellow graduate students first for the group meetings where I learned so much. I would especially thank Christian Rothenbach, Tyson Baldrige and Keye Sun for their support and help with many SEM imaging sessions in the late evenings.

Finally, I thank my wife and family, to whom there are not enough thanks to be given. This work was supported by the NASA Langley Professor program, the NSF I/UCRC and the Virginia Innovation Partnership (VIP) i6 program.

Contents

Chapter 1. Introduction, literature review and motivation	1
1.1. Introduction and outline	1
1.2. Literature Review.....	2
1.2.1. Superhydrophobic properties of microtextured surface.....	2
1.2.2. Replication of pulsed laser microtextured surface.....	3
1.2.3. Replication of pulsed laser generated microtexture on conductive nanocomposite surface.....	4
1.2.4. Electrowetting properties of pulsed laser generated microtextured surface ...	4
1.2.5. Anti-icing properties and superhydrophobicity	6
1.3. Motivation.....	6
1.4. Research objectives.....	7
Chapter 2. Theory of Surface Wetting.....	8
2.1. Young's Theory	8
2.2. Wenzel's Theory.....	9
2.3. Cassie-Baxter Model.....	10
2.4. The effect of surface roughness on contact angle.....	11
2.5. Surface energy and the lotus effect.....	13
2.6. Measurement of contact angle	14
2.6.1. Static contact angle	14
2.6.2. Advancing and receding contact angle and contact angle hysteresis	15
2.6.3. Sliding angle	16
2.7. Electrowetting.....	16
Chapter 3. Experimental.....	19
3.1. PDMS: key properties and suitability for replication medium	19

3.2.	Pulsed laser and microtexture fabrication.....	21
3.3.	Replication of pulsed laser generated microtexture.....	22
3.4.	Optical Characterization of replicated microtextured surface	24
3.5.	Fabrication of carbon nanotube based electrically conducting superhydrophobic nanocomposite with microtextured surface	24
3.6.	Electrical conductivity measurement of MWCNT-PDMS nanocomposite..	26
3.7.	Contact angle goniometer setup.....	27
3.8.	Electrowetting contact angle goniometer setup	34
Chapter 4. Results and Discussion		38
4.1.	Morphology of laser microtextured surfaces and their replicants.	38
4.2.	Optical properties.....	40
4.3.	Contact angle measurement results and analysis	44
4.4.	Electrical conductivity measurement results and analysis.....	50
4.5.	Electrowetting results and analysis.....	54
4.6.	Contact angle measurements for different fluids	61
4.7.	Durability of microtextured surfaces	63
Chapter 5. Conclusions and Future work		65
5.1.	Key findings.....	65
5.2.	Future work.....	66
List of Publications		68
Patents.....		68
Presentations		69
References.....		70
Appendix 1 - MATLAB® program listings for models.....		80
Appendix 2 – C code program to control GPIB power supply.....		85

Appendix 3 – Experimental details of future electrowetting fixture.....	90
Appendix 4 – Published papers.	92

Chapter 1. Introduction, literature review and motivation

1.1. Introduction and outline

This dissertation studies the optical and wetting properties of pulsed laser microtextured poly(dimethylsiloxane) (PDMS) surfaces. Surface texture or surface roughness and in particular microtexture has been shown to be an important component for the creation of superhydrophobic surfaces [1]. A surface is considered superhydrophobic if it has a static (water) contact angle of greater than 150° [2]. Other predictors of superhydrophobic properties include contact angle hysteresis [3], where the contact angle is measured as the volume of the water drop is increased and decreased, and low sliding angle, where a drop of water is placed on the surface to be measured and the surface is tilted and the sliding angle is the tilt angle where the water is seen to begin to slide off the sample [4]. Superhydrophobic surfaces are inspired by nature with the most common example being the lotus leaf which exhibits a self-cleaning surface that water droplets roll off [5]. Potential applications include water repellency in fabrics [6, 7], anti-icing [8, 9] and anti-fouling for marine applications [10, 11] and electrowetting applications where the contact angle can be controlled electrically [12, 13].

The general outline of this work begins with the literature review in section 1.2, followed by the motivation and research objectives. Chapter 2 follows with an introduction to the theory of wetting; covering the main theories of wetting for smooth and rough surfaces and an introduction to electrowetting is also included. Chapter 3 is the experimental section and covers the materials, test fixtures and methods used to create the microtextured surfaces and how the wetting characteristics of these surfaces are measured. In Chapter 4 we discuss the results of the analysis of the optical and wetting properties of the microtextured surfaces including detailed analysis of the contact angle measurement results. Also in chapter 4 we discuss the conductivity measurements of the electrically conducting nanocomposite followed by the experimental results on electrowetting. Chapter 5 closes with the key findings of the research and a brief discussion of potential future work in this area.

1.2. Literature Review

The literature review is organized in four sections. The superhydrophobic properties of microtextured surfaces are discussed first, followed by a review of replication of pulsed laser microtextured surfaces. The review is expanded to cover replication of pulsed laser microtextured surfaces using conductive PDMS nanocomposite and finally the review of electrowetting properties of pulsed laser microtextured surfaces is presented.

1.2.1. Superhydrophobic properties of microtextured surface

Surface microtexture or surface roughness on the micro/nano scale has been shown to be an important component for the creation of superhydrophobic surfaces [1]. Many approaches have been used to create surface microtexture with the goal of creating superhydrophobic surfaces including lithographic techniques in combination with surface treatments [14-16], aligned carbon nanotubes and nanofibers [17-19]. Other popular methods include the sol-gel method [20-22], vapor deposition [23-25] and other methods [26-31]. Each of these techniques creates surface roughness on the micro/nano scale. Recent work shows that for extreme superhydrophobic performance hierarchical surface microtexture is desired [32-35]. Pulsed laser radiation has been shown to be an effective method for producing surface microtexture in metals, semiconductors and insulators [36-40]. Baldacchini et al. reported the creation of superhydrophobic surfaces by coating fluoro-silane on femtosecond irradiated silicon [41]. Yoon et al. similarly reported superhydrophobic surface creation on PDMS by ultrafast laser irradiation [42]. More recently Dong et al. demonstrates a hybrid laser microtexture-chemical etching process to create superhydrophobic copper surfaces with nano-scale structures [43]. The process reported in this dissertation uses inexpensive techniques to fabricate superhydrophobic surfaces on PDMS by directly replicating the self-organized microfeatures obtained by pulsed laser irradiation with no additional surface treatment being necessary to achieve superhydrophobic properties on the replicated PDMS surface. The master can be used multiple times for replication without measurable degradation of the surface [44].

1.2.2. Replication of pulsed laser microtextured surface

Surface microtexturing has become an area of great interest lately due to the phenomenal growth in the photovoltaic solar energy industry [45] and the drive for more efficient and cost effective solar cells [46-48]. Surface microtexture has been demonstrated to increase the efficiency of the solar cell module [49]. An antireflective surface layer is typically used where losses due to reflection amount to 5 – 10% [48, 50, 51]. There are many methods of creating surface microtexture [51-53] , but most typical is the use of a chemical isotropic or anisotropic etching process [54-56] but is not effective for polycrystalline and thin film silicon solar cells. Poly(dimethylsiloxane) (PDMS) using molding techniques have recently been demonstrated for solar cell applications using a variety of polymers such as PMMA [57, 58] and also on UV curable lacquer [59]. Antireflective coatings have also been reported to have been made using nanoimprint replication techniques to produce nanotextured “moth-eye” structures in Yamada et al. [60]. Recently Chen et al. [57] demonstrated nanoscale replicated detail using a multi-step nanoimprint lithography process on PMMA. Also Yao et al. [61] demonstrated replication of simple periodic nanostructures from stainless steel on polycarbonate film. These methods are simpler and cheaper than the more traditional chemical etching processes, however, the method demonstrated in this work shows a simpler single-step process for replicating microtexture. Pivotal in the development of this new microtexture replication process is the recently developed methods for producing microtextured surfaces using pulsed laser radiation [38, 39, 62]. This process can produce microtexture and/or nanotexture on surfaces of metals and semiconductors. This work uses the pulsed laser process for fabrication of master which is then used for replication of surface microtexture.

1.2.3. Replication of pulsed laser generated microtexture on conductive nanocomposite surface

The effect of the addition of multi-walled carbon nanotubes (MWCNTs) in the polymer matrix was investigated for microtextured surfaces. The motivation for this is rapid growth of high-speed electronic equipment operating in the 1 – 10 GHz frequency range and in particular computing equipment driving an ever increasing need for effective shielding both for and from this equipment. The FCC specifically regulates emissions in the range 30 MHz – 5 GHz [63, 64] and in addition, space, shape, and weight are primary design factors for this class of enclosures and equipment of this class tend to be manufactured from polymer materials [65]. Normally such EMI shielding is provided by adding a layer of metal foil either inside the enclosure if permissible or embedded as a layer in the polymer [66]. Other methods to provide EMI shielding include the addition of conductive particles into the polymer matrix or the addition of a conductive finish coating [65, 66]. More and more it is necessary that the protected computing equipment operate in harsh environments where there may be exposure to water. There has been work reported on the use of conductive nanomaterials for EMI shielding [67-69] and structural applications [70] but clearly there is need for a light weight material that is not only provides EMI shielding but also has superhydrophobic properties. Wang et al. [71, 72] and Madaeni et al. [73] have demonstrated the addition of MWCNTs in PDMS to produce a superhydrophobic nanocomposite. Zhao et al. [74], Talaemashhadi et al. [75] and Bayer et al. [76] have also reported electrically conducting superhydrophobic materials by embedding MWCNT's on copolymers. Yao et al. [77] reports electrically conductive superhydrophobic film by functionalized MWCNTs and Park et al. [78] demonstrated replication of a complex surface using PDMS-MWCNT nanocomposite with both superhydrophobic and conductive properties.

The superhydrophobic conductive nanocomposite demonstrated in this work display a negative temperature coefficient (NTC) of resistance similar to that of a thermistor [79]. These NTC thermistor devices find uses in many circuits where temperature sensing and control is required [80].

The electrically conductive, superhydrophobic nanocomposite was achieved with low loading of MWCNT (less than 5 wt %) and has wide applications in many industries.

1.2.4. Electrowetting properties of pulsed laser generated microtextured surface

The recent publication by Zorpette in IEEE spectrum [12] and the recent acquisition of Samsung's electrowetting display division, Liquavista [13] illustrates the importance of electrowetting and controllable wettability in general as a fast growing technology. Zorpette[12] proposes electrowetting displays as a commercial and economic alternative to LCD displays in the near future. Han [81] shows transition from Cassie-Baxter to Wenzel wetting regions for CNT-based nanocomposites (amorphous carbon nanoparticles capped on carbon nanotubes). Londe, [82] shows models of Cassie-Baxter to Wenzel transition, Bormashenko [83] shows transition from Cassie-Baxter to Wenzel based on excitation from vibration, Wang [84] has analysis of impact response in Cassie-Baxter region and demonstrates use of high speed video for analysis which helped us in the design of the second phase contact angle goniometer discussed in section 3.6. Revilla [85] measures electrical resistance of electrowetting apparatus. Lee [86] shows dynamic electrowetting on dielectric analysis on stretched Teflon. Beni and Hackwood [87, 88] from Bell Labs were the first to report of electrowetting technology as early as 1980 and also suggest the use of electrowetting for use in display technology. Berge and Peseux [89] demonstrate a variable focal length lens controlled by electrowetting. Lapierre [90], Seyrat [91] Verplanck [92], Dhindsa [93] and Cahill [94] report on reversible electrowetting on double-nanotextured surfaces, amorphous fluoropolymers, silicon nanowires, vertically aligned carbon nanofibers and silanized silicon nitride respectively.

Comparing Electrowetting to other display technology, Siengenthaler [95] has performed a study of usability of various display technology and Katayama [96] from Sharp provides a comprehensive survey of TFT-LCD technology. Comiskey [97] is the creator of electrophoretic ink (e-ink) technology used in e-ink readers. Hayes and Feenstra [98, 99] the founders of Liquavista demonstrate video-speed electronic paper based on electrowetting.

Zhu et al. [100] shows electrowetting on aligned CNT and introduces the Lippmann equation. Lippmann's [101] 1875 paper [102], translated in [103] demonstrates how electric charge could be utilized to change capillary forces and continued to demonstrate use of a capillary motor and capillary electrometer.

Previously we demonstrated replication of micro/nano textured surfaces on PDMS [104] and later demonstrated the superhydrophobic properties of that replicated surface [44]. Our research group has also recently demonstrated microtexture replication on polycarbonate [105]. We now extend that work by demonstrating reversible electrowetting properties of the replicated surface

and contrast with the electrowetting behavior of our PDMS based electrically conducting nanocomposite [106]. The replicated microtextured PDMS surface shows this reversible electrowetting behavior without the addition of any coatings, oils or other mechanical means.

1.2.5. Anti-icing properties and superhydrophobicity

Superhydrophobic surfaces can minimize the formation of ice due to the non-wetting properties to water. However if ice is formed then superhydrophobic properties do not guarantee that ice will have a lower adhesion. Specialty coatings have been developed to weaken the adhesion of ice to the surface. Wang et al. studied the thickness dependence of ice adhesion for PDMS [107]. Yeong et al. performed ice adhesion testing of superhydrophobic coatings for application in the aerospace industry. The high-speed droplet impact testing showed significant droplet adhesion at higher speeds (>50 m/s) [108].

1.3. Motivation

Twelve percent of fatal weather related aviation accidents between 1990 and 2002 involved icing [109]. A busy airport can spend over \$1,000,000 per day on de-icing equipment, manpower and fluid [110]. General aviation rules disallow flying into “Known Icing Conditions” and require immediate action if the pilot gets into “Known Icing Conditions”.

The current US Wind Energy Capacity is approximately 50 GW, that’s about 40,000 wind turbines [111]. Loss in revenue for a typical wind farm (that’s approx. 250 MW or 150 wind turbines) when shut down due to icing conditions can be over \$30K per day [112], it is not unusual to take several weeks for ice buildup to dissipate, with the wind turbine idle and out of production. The turbine control system typically shuts down to prevent equipment damage. Ice buildup of the blades can cause rotor imbalance which then can cause increased wear and tear of bearings and gearbox and can place additional stress on the structural components of the wind turbine and therefore can reduce the lifetime of the machine. Ice-throw has recently become more of an issue with wind energy opposition groups.

A recent federal study on the cost of corrosion to the US economy placed the total cost at \$276B annually [113]. Of this \$276B the annual cost of corrosion for the US military is estimated at \$20B [113, 114]. Market research shows the size of the corrosion inhibitor business to be as large as \$6B in 2015 with a growth rate of 4.5% [115].

2013 was a record year for the installation of photovoltaic solar power in the US [45]. The US PV market installed 4751 MW in 2013 (a 41% increase) [45]. Installed efficiencies for crystalline silicon, CIGS, and CdTe solar cells remain at 22.9 %, 15.7 % and 12.8 % respectively. An increase in efficiency of 1 % or a decrease in cost of 1 % would have phenomenal impact to this growing industry.

Wetting properties can be predicted by high contact angle (in what's known as the Cassie-Baxter region, see section 2.3), a small contact angle hysteresis and a small sliding angle. So a high contact angle, in the Cassie-Baxter region is much sought for various applications.

Electrowetting gives us the ability to control the movement of small droplets on a surface electrically and has many applications in microelectromechanical systems (MEMS) [116], displays [87, 88] and has potential for low inertia and high speed actuators [89].

The above are but a few of the potential applications of the combination of surface microtexture, superhydrophobic surfaces and conductive polymers and electrowetting. Other potential applications include the electronics industry where surface microtexture can be applied to novel sensors and devices [117].

The use of pulsed laser techniques to produce microtextured surfaces has been demonstrated successfully, however the process is relatively time consuming and takes hours to texture relatively small areas (< a few cm²). Although through the use of newer laser technologies such as nanosecond lasers has shortened the production time significantly, there is certainly a need for a faster, simpler and industrially scalable method for creating surface microtexture with all of the wonderful applications described above in section 1.3. This research investigates the applications of replicated microtexture for superhydrophobic and conductive nanocomposite applications. The above discussion clearly shows the motivation for further research in superhydrophobic surfaces and their applications.

1.4. Research objectives

The overall objective of this research is to demonstrate a low cost method of producing a microtextured superhydrophobic surface that can be made electrically conductive by the addition of multi-walled carbon nanotubes and to investigate the electrowetting properties so that this concept can be considered for various active control of wetting properties applications.

To achieve this objective, this research demonstrates replication of pulsed laser microtextured surface on PDMS and develop an experimental setup to measure the superhydrophobic properties of replicated microtextured surfaces such as water contact angle, advancing and receding contact angles, contact angle hysteresis and sliding angle. Analysis of results using Wenzel and Cassie-Baxter models were performed as well as the measurement of optical properties of the replicated microtextured PDMS surface. We examine the hydrophobic properties of the replicated microtextured surface for a variety of liquids such as distilled water, kerosene, alcohols, naphtha etc.

This research also demonstrates replication of laser generated microtexture on multi-walled carbon nanotube (MW-CNT)-PDMS electrically conductive nanocomposites and measures the electrical conductivity and superhydrophobic properties. Applications of the conductive nanocomposite as a temperature measurement sensor were explored.

Electrowetting properties of the microtextured PDMS and the microtextured MW-CNT/PDMS nanocomposites were investigated at various voltages and the results were also analyzed using Wenzel and Cassie-Baxter models expanded for electrowetting. The microtextured PDMS and microtextured MW-CNT/PDMS nanocomposites were evaluated for reversible electrowetting behavior.

Chapter 2. Theory of Surface Wetting

2.1. Young's Theory

Thomas Young, in his 1805 paper to the Royal society of London, described the forces acting on a liquid drop resting on a solid surface [118]. This description contains no mathematical equations but nonetheless describes the equivalence of the forces acting on the interfacial boundaries between the solid, the liquid and the air. This has become known as Young's Equation and is shown below in (1) and is shown in Figure 2-1-1.

$$\gamma_{SL} + \gamma_{LG} \cos \theta_c = \gamma_{SG} \tag{2.1-1}$$

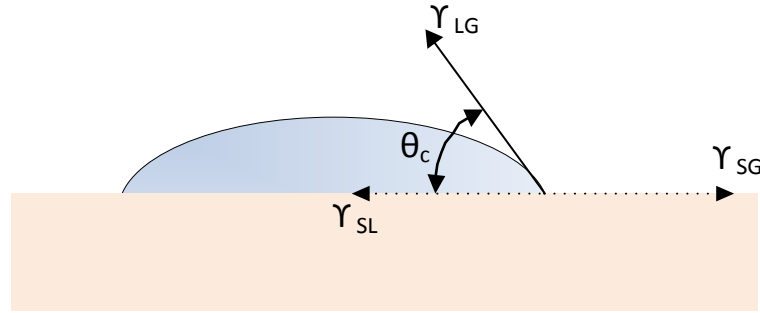


Figure 2.1-1. Schematic showing the forces acting on the interfacial boundaries of the solid-liquid γ_{SL} , liquid-gas γ_{LG} and solid-gas γ_{SG}

In Figure 2.1-1 γ_{SL} is the interfacial force between the solid and liquid, γ_{SG} is the interfacial force between the solid and gas, γ_{LG} is the interfacial force between the liquid and the gas. θ_c is known as the equilibrium contact angle between the liquid and the solid and is also known as the Young's contact angle. The equilibrium contact angle is the mean of the advancing and receding contact angles [119]. Young's equation assumes the surface is perfectly flat and that the liquid is in contact with the solid at all points and therefore cannot be used for surfaces with texture or roughness.

Young's theory and the associated equation 2.1-1 have the advantage of simplicity and predictability. It is relatively easy to place numeric values for a PDMS solid and a distilled water liquid into Young's equation using values of γ_{SG} (Solid-Gas) of 24 mN/m from [120], γ_{SL} (Solid-Liquid) of 41 mN/m from [120], and γ_{LG} (Liquid-Gas) of 72.8 mN/m from [100] we obtain a distilled water-PDMS contact angle of 102.7° which is very consistent with measurements made throughout this work.

2.2. Wenzel's Theory

Wenzel in 1936 [121] extended Young's formulation to take a rough surface into account. Wenzel called the measured contact angle the apparent contact angle and came up with the below formulation that equates the observed contact angle (θ^*) with the equilibrium contact angle (θ_c) that is modified by the roughness factor (r). What Wenzel found was that the roughness had the effect of increasing the effective surface area so there was more solid in contact with the liquid.

$$\cos \theta^* = r \cos \theta_c \quad (2.2-1)$$

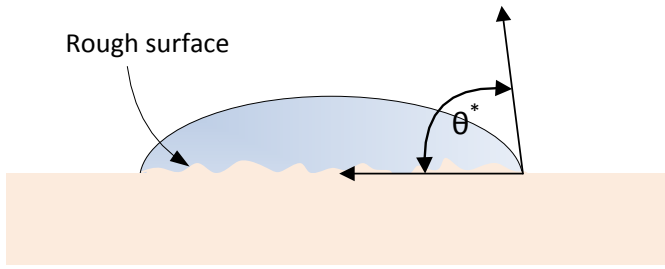


Figure 2.2-1. Wenzel model showing equivalent contact angle θ^*

Figure 2.2-1 shows how surface roughness affects the apparent contact angle. The roughness factor which Wenzel defines as the actual rough area divided by the geometric surface area and is the factor of the increase in surface area caused by the roughness of the surface. In the Wenzel model, the liquid is in contact with the surface at all points and the hydrophobicity is enhanced due to an increase in the interfacial area between solid and liquid causing an increase in the force per unit area. Similar to Young's model, Wenzel's model is limited to applications where the liquid is in contact with the solid at all points and the practical limit to the Wenzel factor r seems to be around 20.

As with Young's theory an example helps make the application of Wenzel's model clear. The microtextured surface of interest in this work may be approximated crudely by a pyramidal surface with a lateral surface area (LSA) given by $LSA = \frac{1}{2} \rho l$ where ρ is the length of the perimeter of the base and l is the slant height. In our case, the typical sample area was 1 cm^2 and thus for a perfectly smooth surface the value of r would be one. Assuming a very rough texture of 100 pyramids with each pyramid 0.1 cm per side and assuming a height of 0.1 cm we get a per unit area and r value of 2. For this case, the observed contact angle would be given by $\theta^* = \cos^{-1}(2 \cdot \cos(102.7^\circ)) = 116.1^\circ$. The microtexture observed in our present research is significantly rougher; our previous work reported roughness factor of 18 [44]. As can be seen from the Wenzel model above values of $r \cos \theta_c < -1$ are meaningless and the model is inapplicable for high values of roughness [120].

2.3. Cassie-Baxter Model

Cassie and Baxter in 1944 further extended the theory of wettability by developing a framework that accounted for the case where the surface features are densely packed and the

water droplet is supported, or partially supported on air trapped between the individual surface features. Figure 2.3-1 shows a drop in the Cassie-Baxter state.

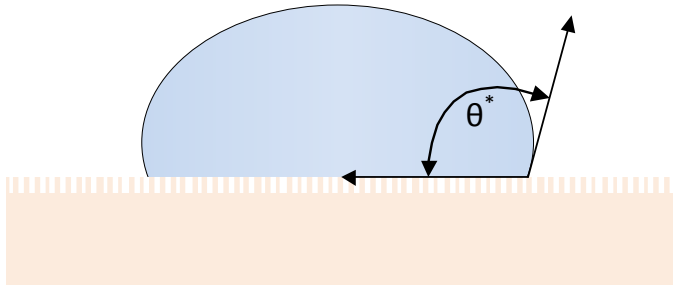


Figure 2.3-1. Cassie-Baxter model showing equivalent contact angle θ^*

The formula below shows how the observed contact angle is calculated.

$$\cos \theta^* = -1 + \phi_s (1 + \cos \theta_c) \quad (2.3-1)$$

Here θ^* is the observed contact angle, θ_c is the equilibrium contact angle and Φ_s is the fraction of solid in contact with liquid, a dimensionless quantity smaller than 1. In the Young's and Wenzel model the liquid is in contact with the surface at all points, here the liquid is no longer completely in contact with the solid and is partly supported by the surface tension and by the air trapped in the spaces between the surface features. Assuming an equilibrium contact angle of 102.7° and a value of 0.4 for Φ_s meaning 40 % of the liquid is in contact with the solid, we get a value for the observed contact angle of $\cos^{-1}(-1 + 0.4(1 + \cos(102.7^\circ))) = 133.5^\circ$. If we decrease that value to 0.1 for Φ_s meaning only 10 % of the liquid is in contact with the solid, we get a value for the observed contact angle of $\cos^{-1}(-1 + 0.1(1 + \cos(102.7^\circ))) = 157.2^\circ$ which is similar to what we reported previously [44].

2.4. The effect of surface roughness on contact angle

Looking at the Wenzel formula for calculating the apparent contact angle, equation 2.2-1, it can be seen that depending on whether the equilibrium contact angle is above (hydrophobic) or below (hydrophilic) 90° the apparent contact angle gets modified by the roughness factor to enhance either the hydrophobic or hydrophilic effect depending on the initial wetting state. A MATLAB® program (see appendix 1) was written that produces a graph of the observed contact angle θ^* versus the equilibrium contact angle θ_c for various values of the Wenzel roughness

factor r . This is demonstrated in Figure 2.4-1. The area on the graph to the left of 90° shows the increase in hydrophilic behavior with increasing roughness whereas the area to the right shows the increase in hydrophobic behavior with increasing roughness.

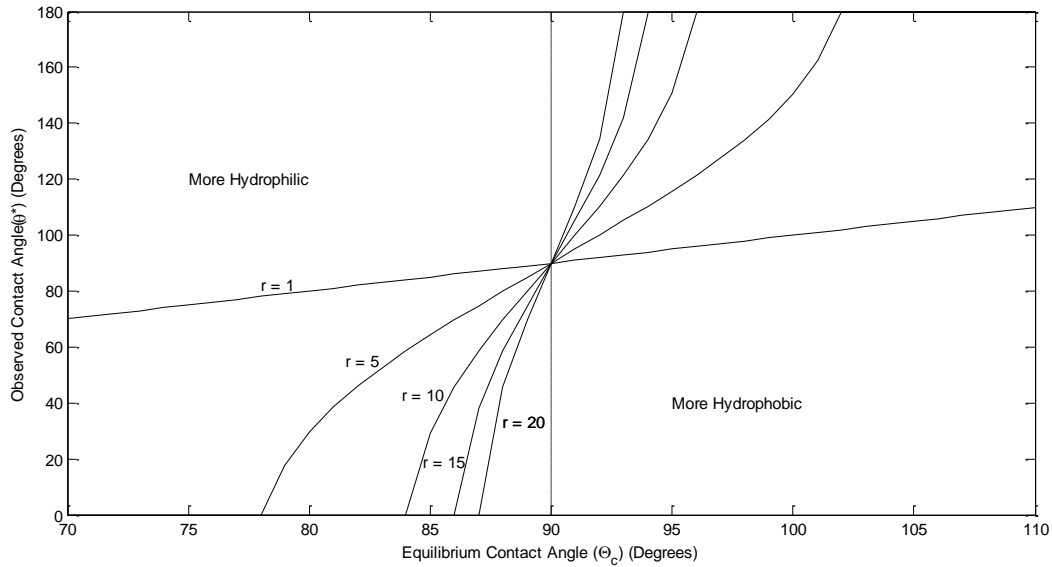


Figure 2.4-1. Observed contact angle vs. equilibrium contact angle for various values of Wenzel roughness (r)

The above graph in figure 2.4-1 shows how the Wenzel equation can be applied with limitations described above in section 2.2.

A similar MATLAB® program (see appendix 1) was written to examine the effect of the Cassie-Baxter wetness factor ϕ_s on observed contact angle and the graph of figure 2.4-2 was produced. Here the observed contact angle is graphed against the equilibrium contact angle for various settings for the Cassie-Baxter wetting factor (ϕ_s). Unlike the Wenzel graph of figure 2.4-1 where the behavior changes as the apparent contact angle passes through 90° , the Cassie-Baxter observed contact angle rises in a continuous manner from 0° through to 180° .

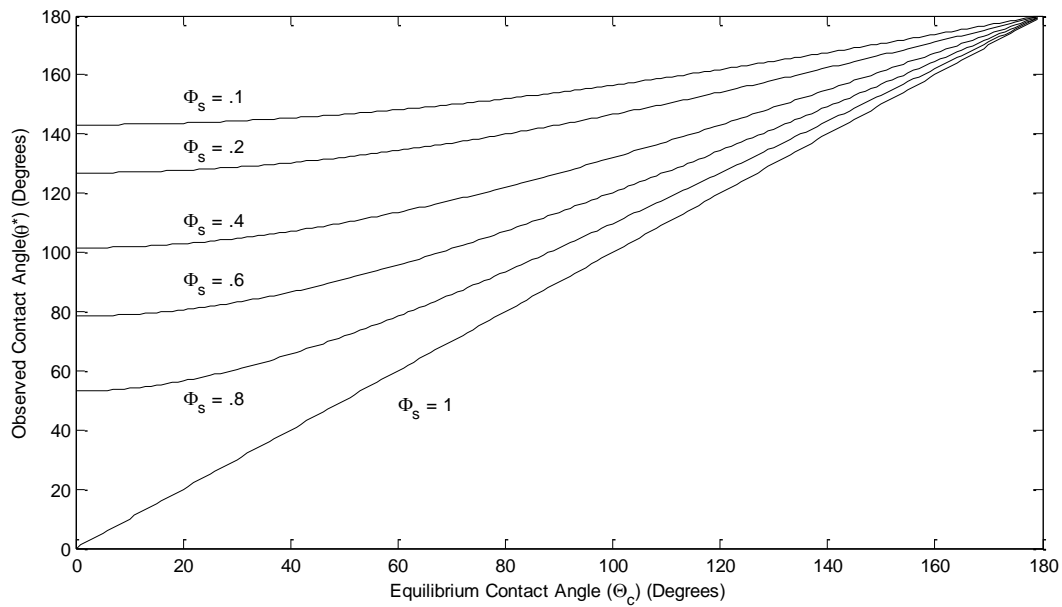


Figure 2.4-2. Observed contact angle vs. equilibrium contact angle for various values of Cassie-Baxter factor (ϕ_s)

2.5. Surface energy and the lotus effect

The wetting properties of a material surface have been shown to depend on both its surface energy and surface roughness [1]. Although lowering the surface energy will enhance its hydrophobicity [122] either by the application of chemical coatings or by choice of low surface energy substrate [123], it is difficult to obtain a water contact angle greater than 150° and a sliding contact angle of less than 10°. Low sliding contact angle, a high static contact angle (>150°) and a low contact angle hysteresis are the elements needed for superhydrophobic surfaces [4, 124].

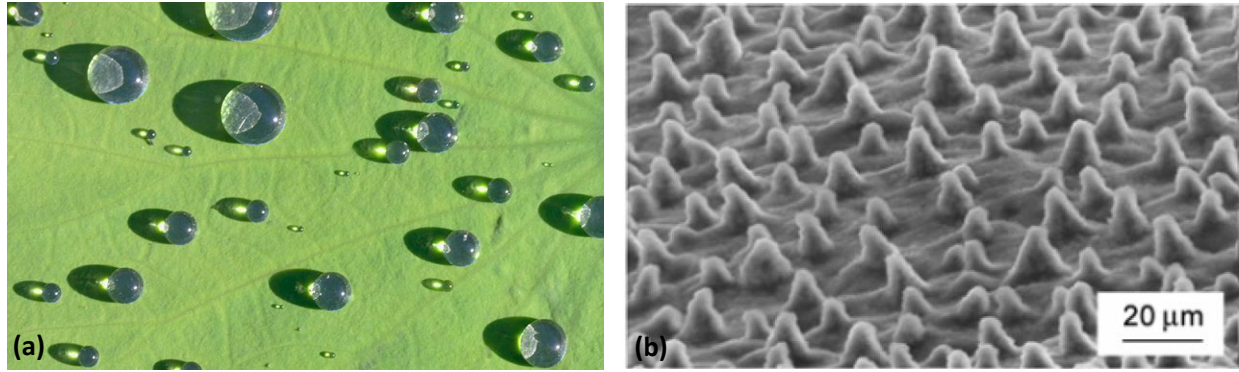


Figure 2.5-1. Images of lotus leaf showing (a) water droplet on American Lotus, *Nelumbo lutea* (image by permission of Henry Domke Fine Art) and (b) SEM image of surface microtexture of *Nelumbo nucifera* (image by permission of Dr. Bharat Bhushan, Ohio State University) [15].

In nature, one of the most commonly seen examples of a superhydrophobic surface is the lotus leaf [125]. When water falls on the lotus leaf, the drops bead-up on the surface and roll off the surface of the leaf carrying dirt and dust particles away with the drop as shown in figure 2.5-1 (a). This effect is referred to as the “Lotus Effect” [5, 126]. This superhydrophobic behavior of the lotus leaf is accredited to the combined effects of microtexture features and nanoscale hairs as can be seen in the SEM image of figure 2.5-1 (b) [15]. The water droplets are supported on the top of these features as described by the Cassie-Baxter model presented above in section 2.3.

2.6. Measurement of contact angle

There are three basic measurements that are used to characterize wetting behavior of a surface and are also used to quantify the degree of hydrophobicity of surfaces. These are the static contact angle, the advancing and receding contact angles and the sliding angle.

2.6.1. Static contact angle

The static contact angle can be measured using what is known as the sessile drop method. As can be seen from the figure 2.6.1-1, a drop of liquid is dispensed on the surface using a syringe or micro-pipette. A manual goniometer or high-resolution camera is used to either, read-off the contact angle, or a snapshot is taken and a protractor can be used to measure contact angle directly off the image. The experimental section of this thesis demonstrates use of the ImageJ software and the drop-snake plugin [127, 128] to measure contact angle. The drop-snake plugin allows the user to place an outline of points on the drop in the digital image itself and then when

the drop is completely outlined the plugin produces a measurement of the left and right contact angles which are then averaged to produce the contact angle. The sessile drop method is described in ASTM D7334 [129] and specifies that the drop size should be between 5 μL and 20 μL . Typically a drop size of 10 μL is used for contact angle measurements [44, 130].

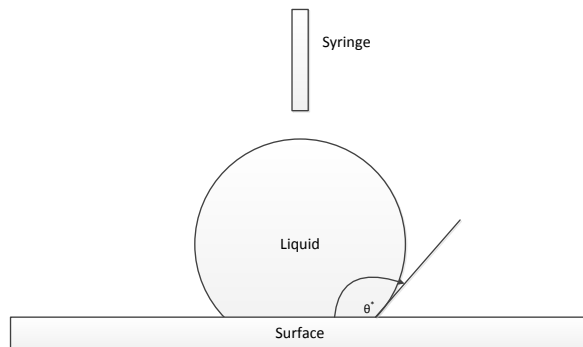


Figure 2.6.1-1. Sessile drop method for measuring contact angle

2.6.2. Advancing and receding contact angle and contact angle hysteresis

The procedure described above can be enhanced in such a way that the syringe remains in contact with the liquid drop and the contact angle measurements are performed dynamically while loading and unloading small quantities of liquid. This allows for measurement of contact angle as liquid is added to the drop in small increments. This contact angle is called the advancing contact angle. Similarly the contact angle is measured as liquid is removed from the drop in small increments to give what is known as the receding contact angle. The difference between the advancing and the receding contact angle is known as the contact angle hysteresis. A small contact angle hysteresis (less than 10°) is a strong predictor of superhydrophobic properties and has become one of the preferred measurements for characterizing these surfaces [3, 131]. As with the sessile drop method a drop size of between 5 μL and 20 μL is maintained.

2.6.3. Sliding angle

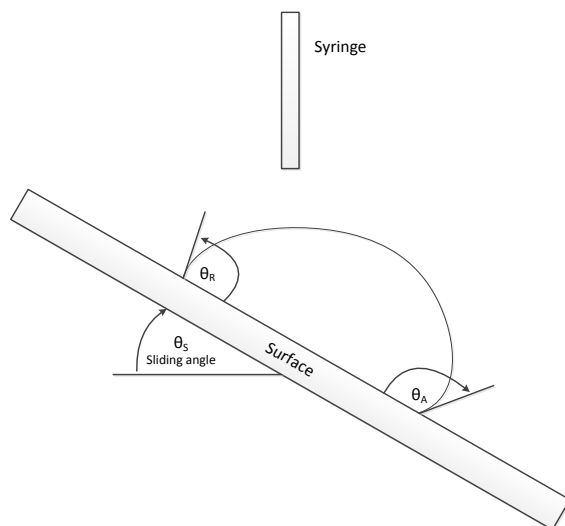


Figure 2.6.3-1. Schematic of sliding angle measurement.

A liquid drop is placed on a leveled superhydrophobic surface under investigation and it is then mounted on an apparatus similar to one shown in Figure 2.6.3-1. In order to measure the sliding angle, the surface is tilted gradually and the angle of tilt is measured when the drop begins to slide off the surface. This angle is known as the sliding angle. In addition to contact angle hysteresis, sliding angle is considered as another preferred measurement for characterizing superhydrophobic surfaces [4, 122, 132]. A small contact angle hysteresis and low sliding angle have been shown to be a predictor of anti-icing properties [8, 9]. This experimental setup can also be used to measure advancing and receding contact angles by examining the advancing (θ_A) and receding edges (θ_R) of the droplet simultaneously with the sliding angle measurement.

When a drop of water is placed on a plane surface and additional water is added to the drop, the contact angle increases until the drop begins to spread. This angle where the drop begins to spread is called the advancing contact angle. Similarly when water is removed from a drop on a surface the contact angle decreases. The angle at which the drop just starts to shrink is called the receding contact angle. When a drop starts to move under tilt the front of the drop gives the advancing angle and the back of the drop gives the receding angle [3, 131].

2.7. Electrowetting

Lippmann is credited [101] as being the first to report that an electrostatic charge can change the contact angle at a solid-liquid interface [102]. A simple electrowetting test fixture is shown below in figure 2.7-1. In this figure a drop of fluid is connected to a voltage source via a terminal, this is normally the syringe through which the fluid is deposited on the insulated surface. The insulator in turn is placed on some substrate electrode that is in turn connected to the negative electrode. When the switch is energized, depending on the voltage, the drop is seen to flatten and the contact angle θ is similarly seen to decrease.

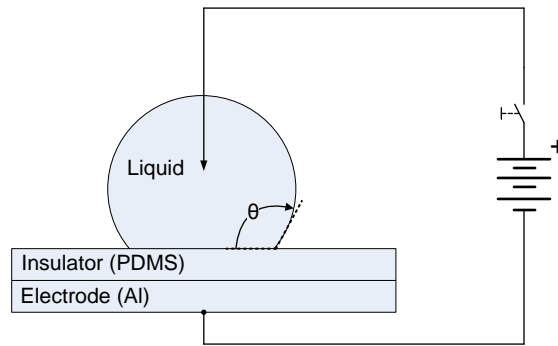


Figure 2.7-1. Electrowetting, showing contact angle θ .

For microtextured surfaces that have superhydrophobic water contact angle greater than 150° figure 2.7-2 shows a droplet resting on the hydrophobic pillars and the air trapped inside the pillars and below the droplet. According to Heikenfeld [133] this state is normally achieved when the advancing contact angle of the water on the pillar θ_Y is greater than 90° giving a convex meniscus between the pillars then this convex meniscus looks very similar to figure 2.1-1 Where, θ_c is the Young's contact angle. In this case the pressure is $2\gamma_{LG}/r$, where γ_{LG} is the liquid-gas surface tension from Young's equation, and r is the radius of curvature of the catenary of the drop between the pillars[133]. This Young-Laplace force prevents the liquid from entering the space between the pillars [133]. From the Cassie-Baxter model [134] the fraction of the liquid in contact with the solid surface (ϕ_s) should be much less than the fraction of the liquid in contact with the air ($1-\phi_s$). This reduced contact area is responsible for the initial high contact angle. A transition to the Wenzel state occurs when the electromechanical electrowetting force exceeds the combined effects of the Young-Laplace pressure and the contact-angle hysteresis [133].

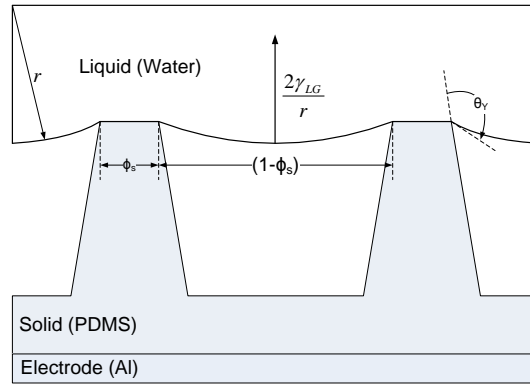


Figure 2.7-2. Electrowetting in the Cassie-Baxter region, adapted from Heikenfeld [133].

Chapter 3. Experimental

3.1. PDMS: key properties and suitability for replication medium

PDMS was obtained from Ellsworth Adhesives (Dow Corning® Sylgard® 184 Silicon Encapsulant) [135]. PDMS was chosen as the medium for replication due to its popular use in the fields of soft-lithography [136] and in the construction of microfluidic devices [137, 138]. As can be seen from table 3.1-1 Sylgard® 184 is a two part polymer that consists of a base that is mixed with a hardener at a 10:1 ratio. The resulting mixture is then cured per the curing schedule in table 3.2-1. Of particular interest in the table of properties is the low refractive index (similar to glass), it is colorless, has low thermal conductivity and the very large volume resistivity. Also PDMS has a wide operational temperature range. Dow Corning® Sylgard® 184 Silicon Encapsulant is specifically marketed to the solar power market segment as a solar cell encapsulant due to its environmental resistance to oxidation, UV light, and due to its thermal and Ozone resistance. PDMS is also easy to handle and is nonpoisonous (PDMS fluids are used as anti-foaming agent in the food preparation industry).

Table 3.1-1. Key properties of PDMS (Dow Corning® brand Sylgard® 184) from [135]

Property	Unit	Result
One or two part	-	Two
Color	-	Colorless
Viscosity (Base)	Pa-sec	5.1
Viscosity (Mixed)	Pa-sec	3.5
Thermal Conductivity	W/m °K	0.27
Specific Gravity (Cured)		1.03
Working Time at 25°C	Hours	1.5
Cure Time at 25°C	Hours	48
Cure Time at 100°C	minutes	35
Cure Time at 125°C	minutes	20
Cure Time at 150°C	minutes	10
Dielectric Strength	kV/mm	19
Volume Resistivity	ohm*cm	2.9E+14
Linear CTE	ppm/cm	340
Tensile Strength	MPa	6.7
Refractive Index	@ 589 nm	1.4118
Refractive Index	@ 632.8 nm	1.4225
Refractive Index	@ 1321 nm	1.4028
Refractive Index	@ 1554 nm	1.3997
Operational temperature	°C	-45 to 200

3.2. Pulsed laser and microtexture fabrication

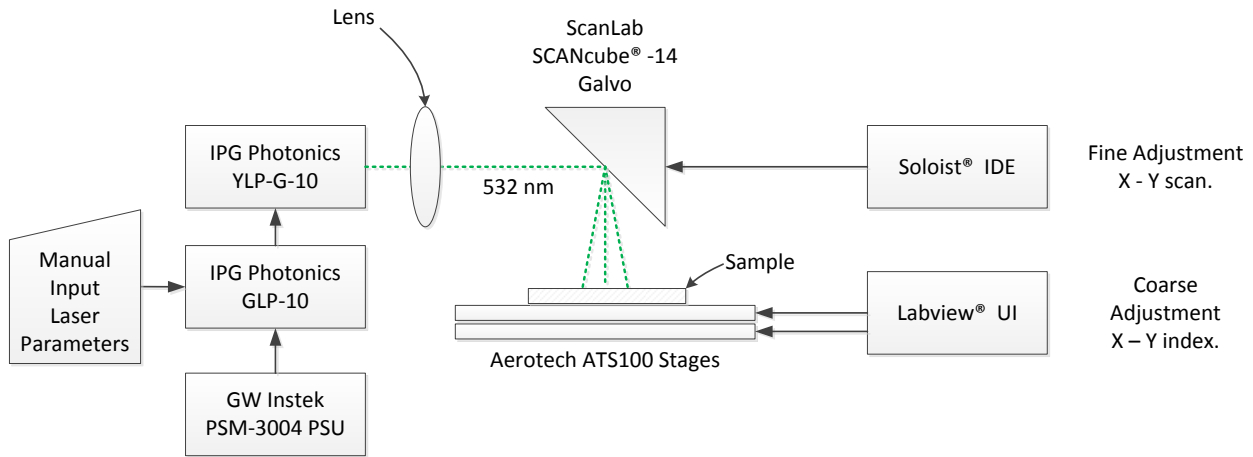


Figure 3.2-1. Pulsed laser and supporting equipment (IPG Photonics YLP-G-10 Pulsed Ytterbium Fiber Laser shown)

The original Ti and Si masters used in the replication section (Section 3.3) of this thesis were created using a regeneratively amplified Spectra Physics Ti-sapphire laser system. Later samples came from the IPG Photonics Fiber Laser shown above. A survey of pulsed-laser equipment was performed comparing various systems in the research group lab [139] that showed that the fixture above was capable of producing microtextured samples faster and cheaper than the earlier Ti-sapphire system. The settings for the laser controller are critical for producing microtexture and the optimum settings differ for different materials. The GW Instek power supply delivers a constant 5.0 V to the modulation input of the laser controller. As can be seen in figure 3.2-1 above there are three separate user interfaces to the test fixture, the laser controller (GLP-10 module) that controls the power and repetition rate of the laser, the Soloist® IDE that controls the Galvo and the Labview user interface that controls the X and Y stages.

To begin a microtexturing a new sample it is first necessary that the stages and galvo are aligned properly and that the system coordinates are set to the proper (0,0) point. For this initial setup the laser controller is set to the lowest power setting of 0 % and the repetition rate is set to 20 KHz. The laser can now be turned on and at this power level it is safe to focus (the stage height has a Z adjustment), the sample is positioned such that the beam is targeted at the exact

top left position of the sample. The galvo can then scan the beam across the target in the X axis while indexing the Y axis allowing for a small overlap in each scan to ensure coverage. Using the galvo we can scan an area of approximately 4 cm² in a time frame of about five minutes. To cover larger areas we must index the position using the ATS100 stages and re-zero at this new position and repeat. Using the galvo for scanning and the ATS100 for indexing between scanning sessions has allowed for samples of ~100 cm² to be produced. As can be seen from the above procedure the manufacturing process to produce the master is quite time consuming providing motivation the team to search for a simpler and scalable replication solution where a single master can be reused many times.

3.3. Replication of pulsed laser generated microtexture

Replication of surface microtexture begins with PDMS. This polymer is comprised of a two part mixture, part 1 being the base and part 2 being the hardener. The base and hardener are mixed at a 10:1 ratio. When dispensing and mixing it is easy to introduce air bubbles so vacuum desiccation may be necessary to eliminate bubbles after mixing. Ti and Si self-assembled microtexture masters were fabricated using the direct laser processing method described in section 3.2. The details of the self-assembled laser microtexture technique and the fabrication process can be found in the following references [37-39].

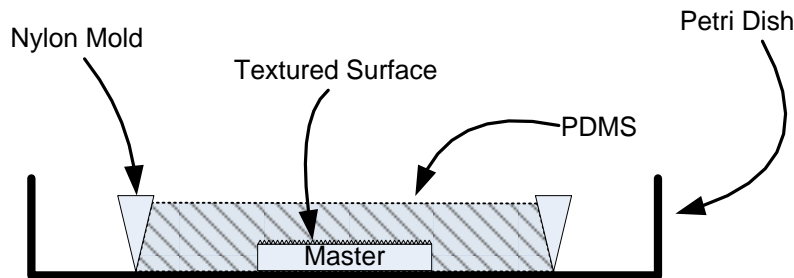


Figure 3.3-1. Initial PDMS microtexture replication apparatus.

Figure 3.3-1 above shows the initial apparatus used to investigate replication on PDMS. Referring to the diagram the master (either Ti or Si) is placed with the microtextured side up on a petri dish. A 50 mm diameter nylon washer forms the side of a mold into which PDMS is poured. The petri dish is then placed on a hotplate at 80 °C for a minimum of 1.5 hours. The process is explained in detail in [104].

Similarly, the method shown in Figure 3.3-2 below was developed that used an embossing process for replication. In this method a 190 μm layer of PDMS is spin coated on to the substrate (glass in this case) and is placed on a hot plate set to 70 $^{\circ}\text{C}$ for 3 minutes. The purpose of this pre-embossing cure is to allow the PDMS to thicken and to prevent PDMS from adhering to the master during the embossing process.

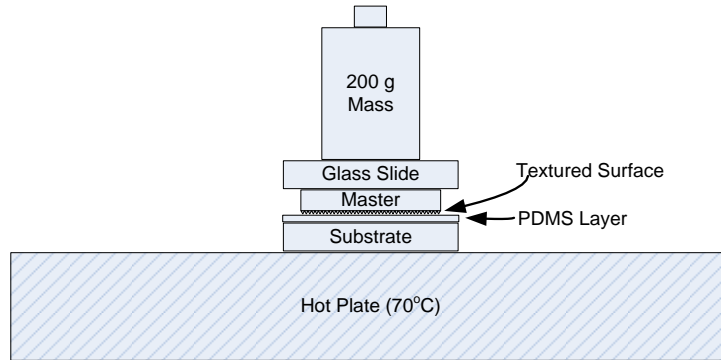


Figure 3.3-2. Microtexture replication on PDMS using embossing method.

After the pre-embossing cure time, the master is placed face-down on the substrate with a glass slide (to ensure flatness) and a 200 g mass for uniform force. This complete stack is then cured on the hot plate for an additional 15 minutes (or more). The mass is then removed along with the glass slide. The master can then be carefully removed from the PDMS and then the PDMS film can be removed from the glass substrate. Figure 3.3-3 shows a removed film that shows microtexture.



Figure 3.3-3. Microtextured PDMS film obtained from the embossing process.

3.4. Optical Characterization of replicated microtextured surface

Optical characterization of the replicated micro/nano textured surface were performed using light from a perpendicularly polarized helium-neon gas laser (JDS Uniphase Model 1508P-1, JDS Uniphase Inc., USA) and an integrating sphere (Model:RTC-060-SF from labSphere Inc.) with Spectrafect® coating. Surface cross section and scanning electron microscope (SEM) imaging was performed with a SUPRA 40 SEM (Carl Zeiss, Germany).

3.5. Fabrication of carbon nanotube based electrically conducting superhydrophobic nanocomposite with microtextured surface

Multiwall carbon nanotubes of dimensions shown in Table 1 below were obtained from NanoLab Inc. These multiwall carbon nanotube products were selected based on earlier work on carbon nanofibers [68] where it was expected that longer nanotubes would produce a nanocomposite with a lower conductivity.

Table 3.5-1. Multiwall carbon nanotube products from NanoLab Inc.

Product	Length (μm)	Diameter (nm)	Structure	Packing Density (g/cm ³)
PD15L15-20	15-20	15	Hollow	0.032
BPD30	20	30	Bamboo	0.025
PD30	20	30	Hollow	0.070
PD15L1-5	1-5	15	Hollow	0.100

The carbon nanotube – PDMS mixture was agitated using an ultrasonic processor (Qsonica Q500) and a small 300 rpm 3.2 V dc motor. Resistivity measurements were made using a Keithley 6105 Resistivity Adapter. Current measurements were made using either a Keithley 616 Digital Electrometer (p-Ammeter) or a UNI-T UT803 Multi-meter (μ-Ammeter). Voltage

measurements were made using a Fluke 8012A multi-meter. Voltage was applied using either a Keithley model 240 high voltage DC supply for voltages over 30 V and for less than 30 V, a Mwtech HY3005A DC power supply was used.

The process used to manufacture replicated microtexture on PDMS is further expanded to produce an electrically conductive nanocomposite by adding MWCNT to the mixture prior to the addition of the hardener. For the nanocomposite to be highly conductive the mixture must be uniformly mixed. Several different methods of mixing were investigated. First agitation using an ultrasonic processor was attempted, but it was found that the agitation process produces too much heat (even with cooling using ice) causing the nanocomposite to prematurely harden. Mixing by hand was attempted but the resulting mixture was not sufficiently uniform and the resulting resistivity was found to be higher than required and a bulk loading of 3 wt % was the limit for this method. Another method was investigated that required mixing the MWCNTs in toluene similar to Liu et al. [140] however a bulk loading of 2 wt % was found to be the achievable limit for this method. The method that was found to be the most effective and the method that allowed a bulk loading of 4.4 wt % was using a 300 rpm 3.2 V dc motor to mechanically mix the MWCNT – PDMS base mixture for up to one hour prior to the addition of the PDMS hardener. The conductive nanocomposite is fabricated by placing 20 g of the PDMS base (Sometimes referred to as part a) in a 50 ml flask. MWCNT is added to achieve the desired bulk loading and the mixture is agitated using the DC motor at low RPM for 60 minutes. To harden the polymer two grams of PDMS hardener (Sometimes referred to as part b) are added and mixed for an additional 5 minutes. To produce the samples used for the conductivity measurements using the Keithley 6105 resistivity adapter ten grams of the resultant polymer-MWCNT mixture are placed in a 75 mm diameter circular mold placed in a 90 mm diameter petri dish as shown in Figure 3.5-1.

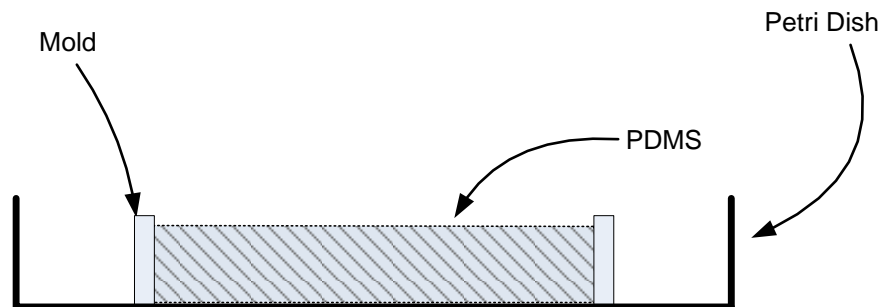


Figure 3.5-1. Conductive nanocomposite sample fabrication apparatus.

This mold was prepared in accordance with the earlier procedure outlined in section 3.2 and resulted in a sample thickness of 2.54 mm and a diameter of 70 mm which are within the specifications of the Keithley resistivity adapter [141].

For conductive nanocomposite experiments with microtexture the above procedure was modified to use the same nylon mold as Figure 3.4-1 and a Ti master was used as described in section 3.4 to replicate the microtexture surface using the conductive nanocomposite.

3.6. Electrical conductivity measurement of MWCNT-PDMS nanocomposite

Figure 3.6.1-1(a) and (b) shows details of the experimental fixtures used to determine the volume and surface resistivity respectively of the conductive nanocomposite produced by the incorporation of multiwall carbon nanotubes (MWCNT) in the PDMS polymer prior to curing.

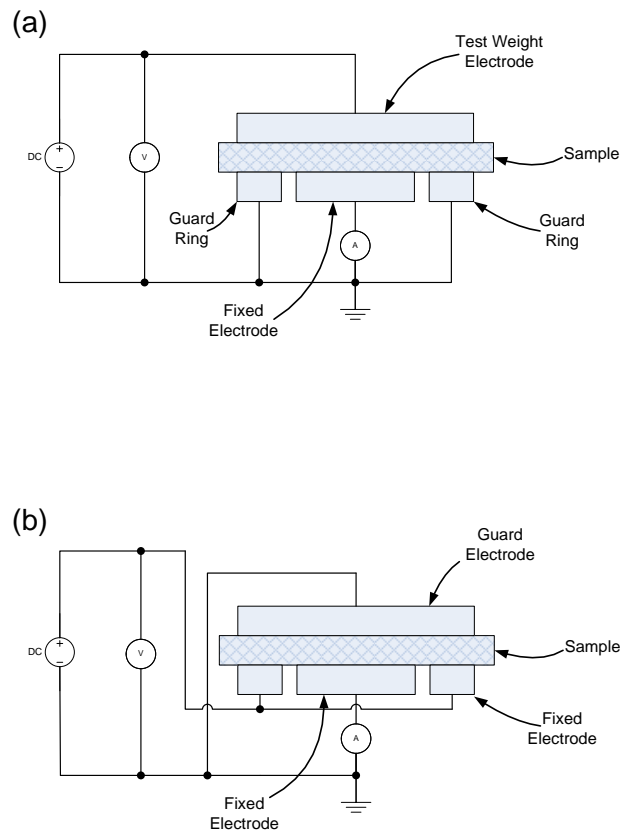


Figure 3.6-1. Test fixture used to measure (a) volume resistivity and (b) surface resistivity

Resistivity measurements are made in accordance with ASTM D 257 [142] and following the special instructions provided with the resistivity adapter [141]. Both volume and surface resistivity measurements were made using the test fixtures shown above in figure 3.6-1. Three measurements were made of each sample and were averaged. A high voltage power supply and electrometer combination was used for high resistivity samples and a multi-meter and bench-top power supply was used for lower resistivity samples.

3.7. Contact angle goniometer setup

A central part of this work involves the characterization of the wetting effects on a given surface to determine the degree of hydrophobicity of the surface and the effects of the surface microtexture treatments if applicable. The instrument typically used for these measurements is called a contact angle goniometer and when it was decided that these types of measurements were necessary three major suppliers in the field of CA goniometers were investigated for suitability. The main suppliers investigated were Attension (TheteLite model), Ramé-hart instrument co. (Model 190), and KRÜSS (Model DSA25B).

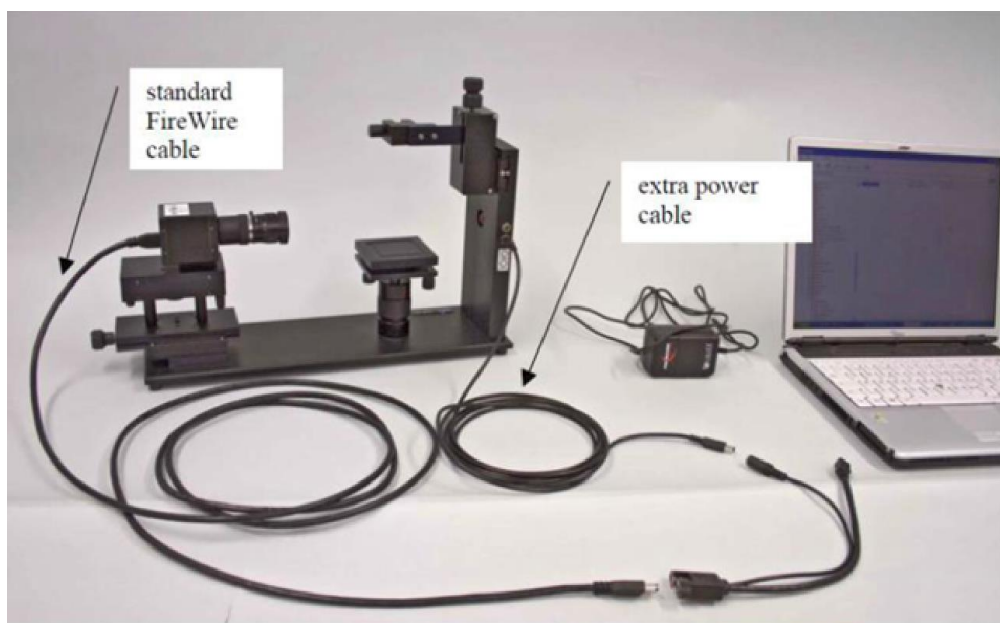


Figure 3.7-1. Commercial contact angle goniometer – Attension CAM100 model.

The above three suppliers were contacted and quotes were requested for their entry level products since we are primarily interested in measuring CA which is a basic feature of such a device. When the three quotes were gathered it was found that each quote was close to \$10K +/-

\$500. With extended and time consuming negotiations we could probably discount this to around \$6500; this was still more than what we thought we should have to pay for such an instrument. It was therefore decided that an instrument should be designed using commercial off-the-shelf (COTS) components.

To make this instrument the “Lean” and “Agile” development methodologies developed by Steve Blank[143] and Eric Ries [144] were followed and a prototype or minimum viable product (MVP) [143, 144] would be created so quick feedback of how the instrument works and rapid changes in the design could be made before too much time and money was committed in to the project, indeed the first instantiation of the CA goniometer was fashioned from parts available in the lab and from local commercial suppliers.



Figure 3.7-2. The first prototype CA goniometer

This first device consisted of a simple hardwood plywood base, a 10 ml syringe, two clamps, a penlight, a single lens reflex (SLR) digital camera and a set of extension rings to reduce the focal length allowing the camera to operate in macro mode.

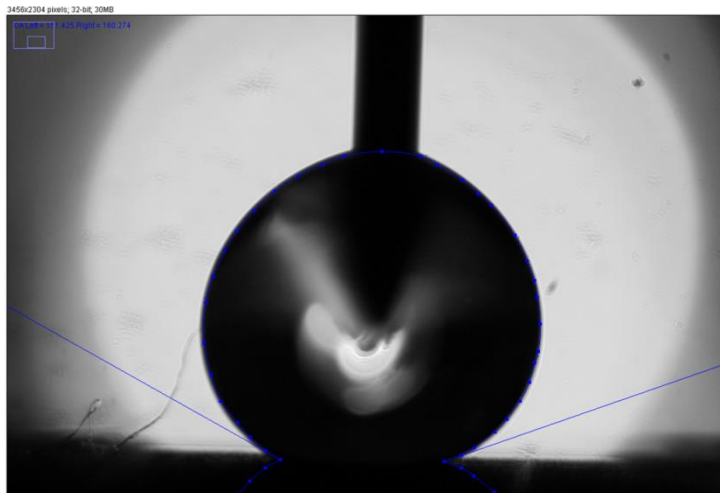


Figure 3.7-3. Results from the first prototype CA goniometer.

Processing the digital image from the SLR requires the use of the ImageJ software and the drop-snake plugin [127, 128]. The drop-snake plugin allows the user to place an outline of points on the drop in the digital image and then when the drop is completely outlined the plugin produces a measurement of the left and right contact angles as can be seen in figure 3.7-3 above. Typically the right and left contact angle measurements are averaged and the process is repeated several times (typically three).

The procedure for making a contact angle measurement using the first prototype CA Goniometer is as follows:

1. Set up digital camera paying close attention to tripod height so the image of the “stage” in centered and level.
2. Place sample material on stage.
3. Take sample image to verify lighting and focus, transfer image to PC to verify this.
4. Using syringe place 10 μl drop on surface (using the sessile drop method).
5. Take image, transfer image to PC to verify image is clear (see Figure 3.7-3).
6. For advancing and receding, rather than placing a single drop, allow the syringe to add volume to the drop as repeated images are taken (I took 7 advancing and 7 receding images), then take multiple images as volume is removed from the drop.
7. Dismantle equipment for storage.

As can be seen, this is a fairly lengthy procedure and it was difficult to obtain reproducible results from different tests due to the variability of setting up the equipment. Especially time consuming in the above procedure is the cycle of taking the static image using the digital camera (the first prototype used a Canon EOS 350D SLR) and connecting the camera to the laptop computer to view the image to either verify the framing of the sample or to save the image for analysis. Lighting was also identified as a problem area and although readings of CA could be made, the images were not considered “publication quality” and did not compare well with those taken with commercial equipment. In the first prototype it was difficult to manipulate the stage (the stage in this text fixture is immobile) such that sample was correctly framed and centered in the image. Making measurements of the sliding angle was not possible with this equipment and a separate test fixture with a tilting stage from Thorlabs was used to make the sliding angle measurements.

The next iteration of the contact angle goniometer was also modeled from commercial instruments similar to that of figure 3.7-1. For this iteration we integrated experience from one of our team members who was using video equipment for the purpose of accurately timing astronomical phenomena such as the occultation of a distant star by a nearby asteroid. For this occultation timing work a sensitive black and white video camera that produces an NTSC compatible signal is used to view the event through a telescope and the video signal is then time-stamped using a GPS device where the timestamp is integrated directly into the video frame. The attention was drawn to the availability of low cost high quality video camera and image capture equipment.

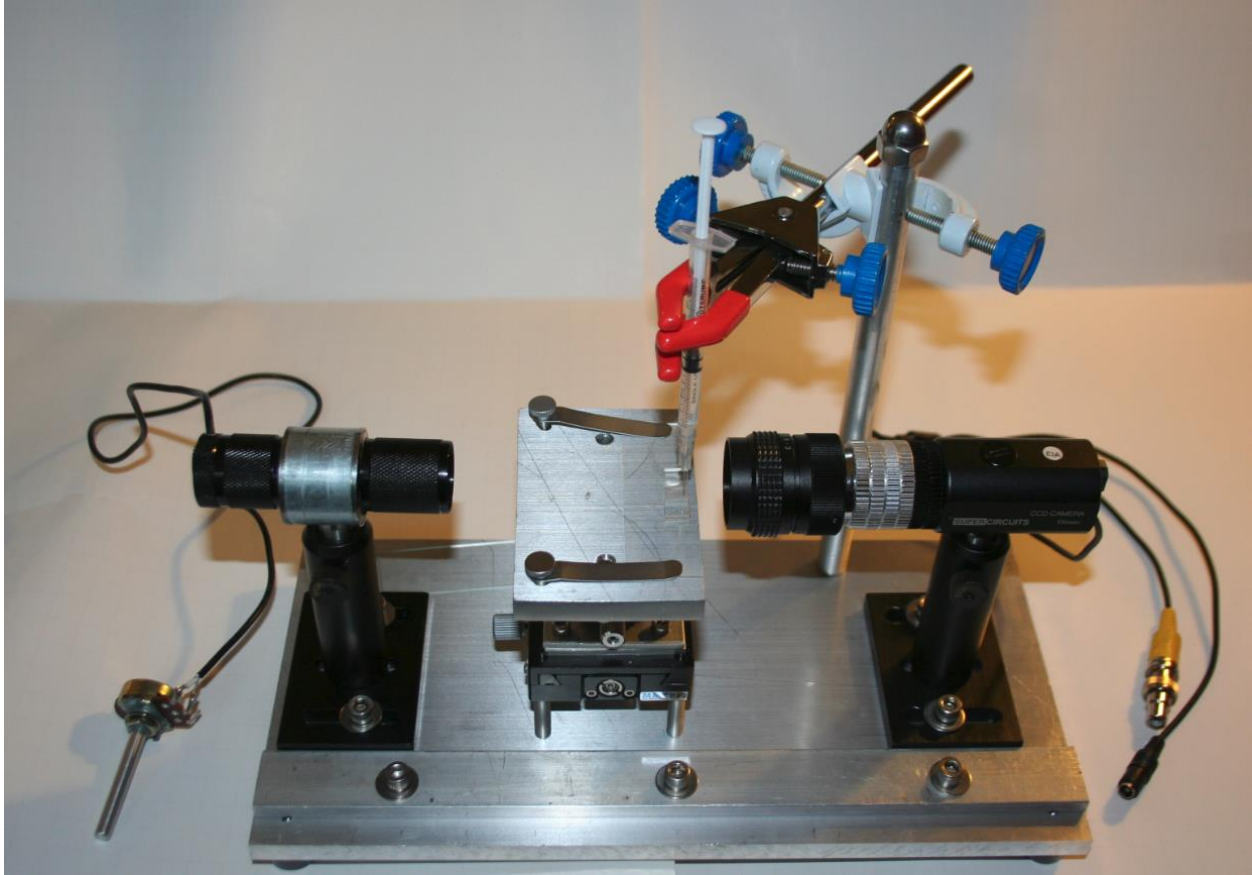


Figure 3.7-4. Second iteration of CA goniometer

Figure 3.7-4 shows the second iteration of the CA goniometer instrument. A solid aluminum base was used, a 6" x 12" section was cut from a 3/8" x 12" x 12" 6061 aluminum plate. Aluminum plate was chosen due to its rigidity and machinability (it was important to be able to drill and tap). Standard Thorlabs bases and optical posts were used to mount the light and video camera. A low-light C-Mount video surveillance camera was coupled to a 25 mm C-Mount lens. A total of six C-Mount optical rings were used so the lens could operate in "Macro" mode allowing for a very short focal length. The stage was constructed from a combination of a MT Compact Dovetail Linear XY Stage and an MMT 10° Tilting stage with some mounting hardware. The surface of the stage was manufactured from a 6 cm x 9 cm section of the aforementioned 3/8 inch aluminum plate with holes drilled to accept two Leitz microscope stage clips. Figure 3.7-5 shows a close-up of the stage assembly. Illumination of the stage is provided by an adjustable LED light source. An iris was later added to the light source to provide additional control of the illumination.

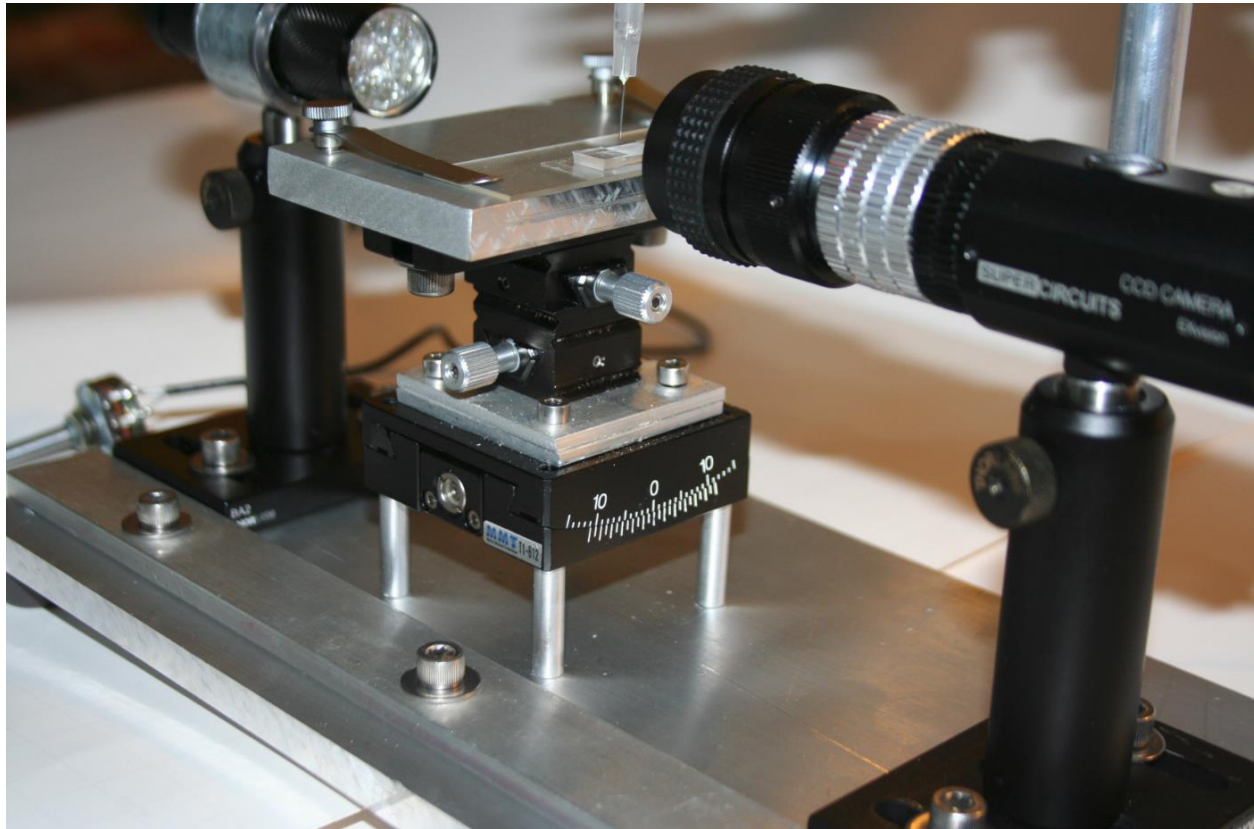


Figure 3.7-5. Close up of second iteration of CA goniometer

The assembled stage can move in slow motion in X and Y directions, and can tilt up to 20° in +Y or -Y direction. The tilting action allows for measurement of the sliding angle, a measurement impossible in the earlier iteration of the prototype. One advantage of having the tilting stage as an integral component of the contact angle goniometer is that a single process can now be used (if desired) to measure advancing and receding contact angles as well as obtaining a value for the sliding angle. This would be accomplished by placing the drop on the stage, recording video, and slowly tilting the stage until the drop begins to move. The value of the tilt angle is the sliding angle, whereas the value of the right contact angle and left contact angle just before the drop is seen to move (assuming we tilt clockwise) become the advancing and receding contact angles respectively.

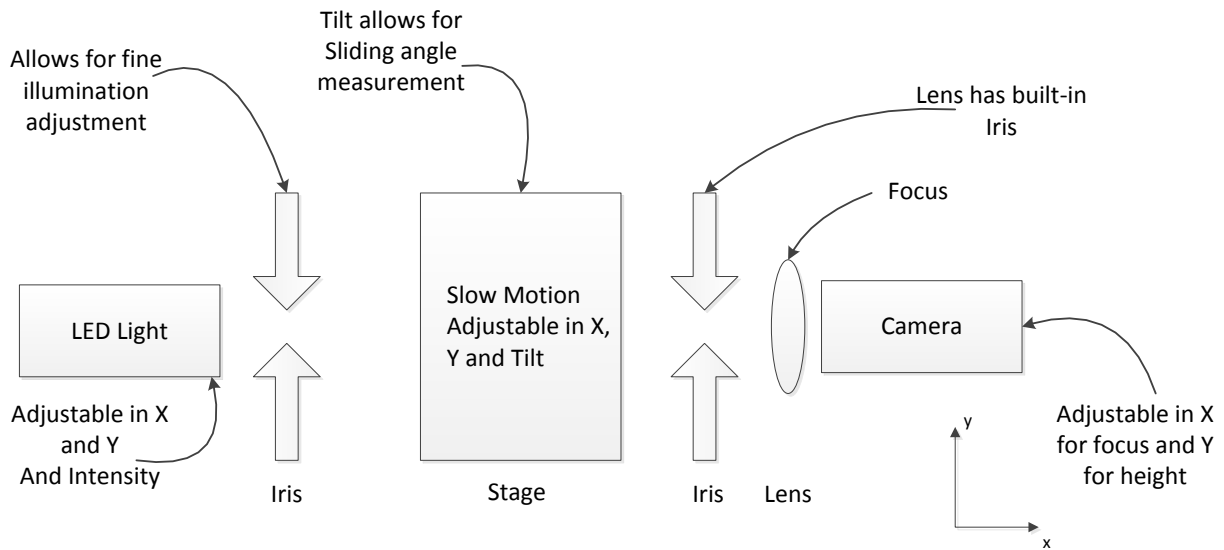


Figure 3.7-6. Schematic of the second prototype CA goniometer showing degrees of freedom

Figure 3.7-6 shows a schematic of this second prototype CA goniometer that shows the various degrees of freedom of the instrument. There are many adjustments that can be made in addition to those of the stage, namely the intensity and aperture for the LED light source can be adjusted and the CCD camera is adjustable in X, Y, height and aperture.

After assembly a sample was placed on the stage and a 10 μl drop was placed on it. Figure 3.7-8 shows the resulting image from this drop analysis. The text in the upper left in small font shows the CA to be 147° for this particular sample.

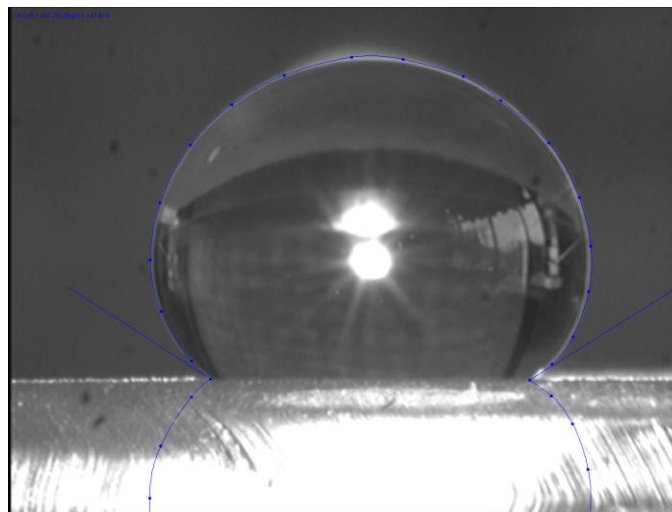


Figure 3.7-7. Results from the second prototype CA goniometer

The image in figure 3.6-8 is the result of adjusting the lighting power, lighting aperture, focus, lens aperture and careful framing of the drop on the sample. The second prototype has many degrees of freedom allowing many different uses. In addition to the measurement of contact angle and contact angle hysteresis (the difference between advancing and receding CA) the second prototype allows for the measurement of the sliding angle.

Static contact angle measurements were made in accordance with ASTM D7334 [129] using the sessile drop method and a 10 μl distilled water drop. The contact angle hysteresis measurements were made using drop volume between 5 μl and 20 μl . Digital imagery is utilized to capture the data and analysis is performed using the techniques and software [127, 128] outlined in section 3.7 with equipment similar to that shown in Figure 3.7-2. For measurement of sliding angle a tilting stage was used similar to that shown in figure 3.7-5 and is described in section 3.7.

3.8. Electrowetting contact angle goniometer setup

For electrowetting contact angle measurements the test apparatus shown in figure 3.7-4 and 3.7-5 is extended as shown in figure 3.8-1. This allows contact angle measurements to be made that can be correlated with power supply settings from the computer. The high voltage supply used was a Stanford Research Systems PS325 with the voltage output being controlled by a PC via the GPIB interface. A PC 164C video camera (Super Circuits Inc.) was used to gather 30 frames per second (FPS) video. A GPS video text overlay unit (PIC-OCD.com) was used to insert a GPS timestamp in the video stream and an application was written in C (see listing appendix 2) to interface to the GPIB card to control the power supply and to output a time-stamp when the voltage is set. After ramping the power supply to the desired output the program waits 100 ms to allow correlation of the 30 frames per second video with the power supply output. The PC's time was synchronized using NTP to NIST internet time servers. The clock was verified to be within 5 ms of UTC before each experiment. The voltage was also monitored on a DVM (Fluke 8012A). For later experiments a Stanford Research Systems DS345 function generator was used to modulate the high voltage supply from the PS325.

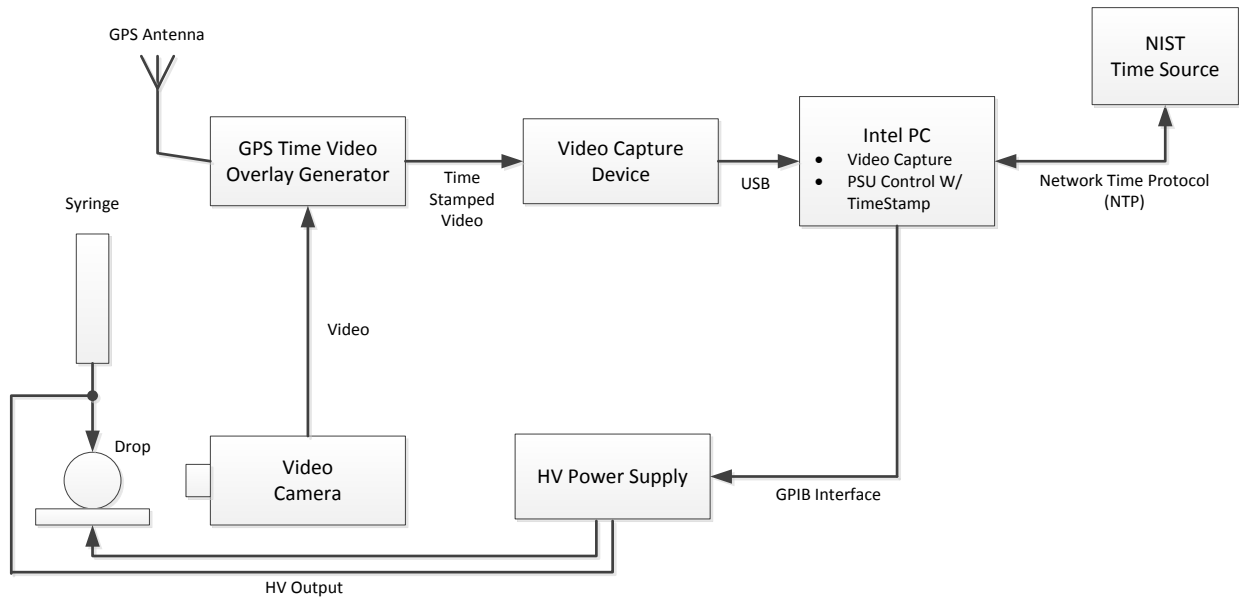
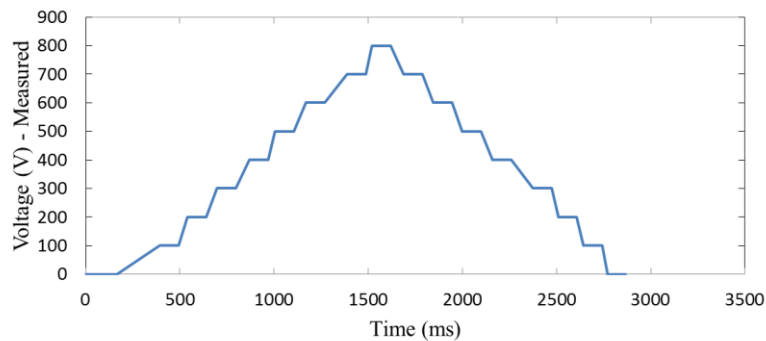


Figure 3.8-1. Test system used to measure electrowetting contact angles

The Video camera of figure 3.8-1 captures data at a rate of 30 FPS and to facilitate correlation between the power supply settings from the PC via the GPIB bus and the measured contact angle the application described earlier was written that ramped the voltage up and down, allowing the setting to remain stable for a 100 ms window to facilitate correlation with the timestamps in the video. Figure 3.8-2 below shows the measured and ideal output voltage from this program, and figure 3.8-3 shows a sample text file output.



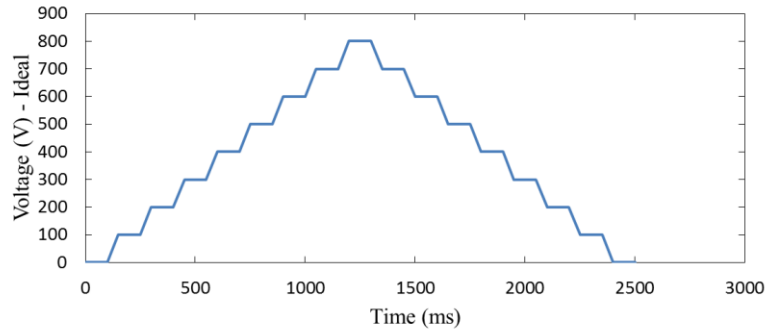


Figure 3.8-2. Power supply ramp generation from PC, measured above and ideal below.

Looking at the two graphs above it can be seen that the PC can introduce quite a bit of jitter which was the motivation for the 100 ms reading settling time introduced by the power supply application code. This 100 ms gives ample time to select the timestamp from the text file (figure 3.8-3) in the appropriate video frame from the video stream.

```

0V at Sat Feb 28 16:06:26.314
100V at Sat Feb 28 16:06:26.450
200V at Sat Feb 28 16:06:26.619
300V at Sat Feb 28 16:06:26.818
400V at Sat Feb 28 16:06:26.982
500V at Sat Feb 28 16:06:27.120
600V at Sat Feb 28 16:06:27.263
700V at Sat Feb 28 16:06:27.402
800V at Sat Feb 28 16:06:27.541
700V at Sat Feb 28 16:06:27.690
600V at Sat Feb 28 16:06:27.823
500V at Sat Feb 28 16:06:27.958
400V at Sat Feb 28 16:06:28.120
300V at Sat Feb 28 16:06:28.248
200V at Sat Feb 28 16:06:28.398
100V at Sat Feb 28 16:06:28.536
0V at Sat Feb 28 16:06:28.694

```

Figure 3.8-3. Power supply GPIB control program text file output showing timestamps.

The procedure to capture the raw experimental data can be separated in to two categories, capturing the data and analyzing the data as follows:

Capturing the data

1. Verify NTP delay using ntpq command (try to keep within 5 ms, restart PC if necessary)
2. Start capture of video verifying that the video stream is appropriately time stamped by the GPS video text overlay unit.

3. Run the program to ramp the high voltage power supply, recording the time stamps produced in a text file for later use.
4. Repeat for each experiment

Analyzing the data

1. Open the video file and locate the video frame with the appropriate time stamp from the text file.
2. For each power supply step when the time stamps match (within 30 ms), save the video frame as an image file (such as JPEG).
3. Repeat steps 1 through 2 for each Video file
4. Open each image with the ImageJ image processing software [127].
5. Set image type to 32 bit greyscale image
6. Load the Drop-Snake [128] analysis plugin
7. Analyze the drop using the Drop-Snake [128] analysis plugin and record the contact angle by contouring the image.
8. Exit the plugin, close the image.
9. Repeat for each image of the experiment.

Chapter 4. Results and Discussion

4.1. Morphology of laser microtextured surfaces and their replicants.

As discussed in section 3.3 pulsed laser microtexture fabrication is used to produce a replication master using either titanium or silicon. This master is then used as detailed in section 3.4 to replicate the surface microtexture on PDMS.

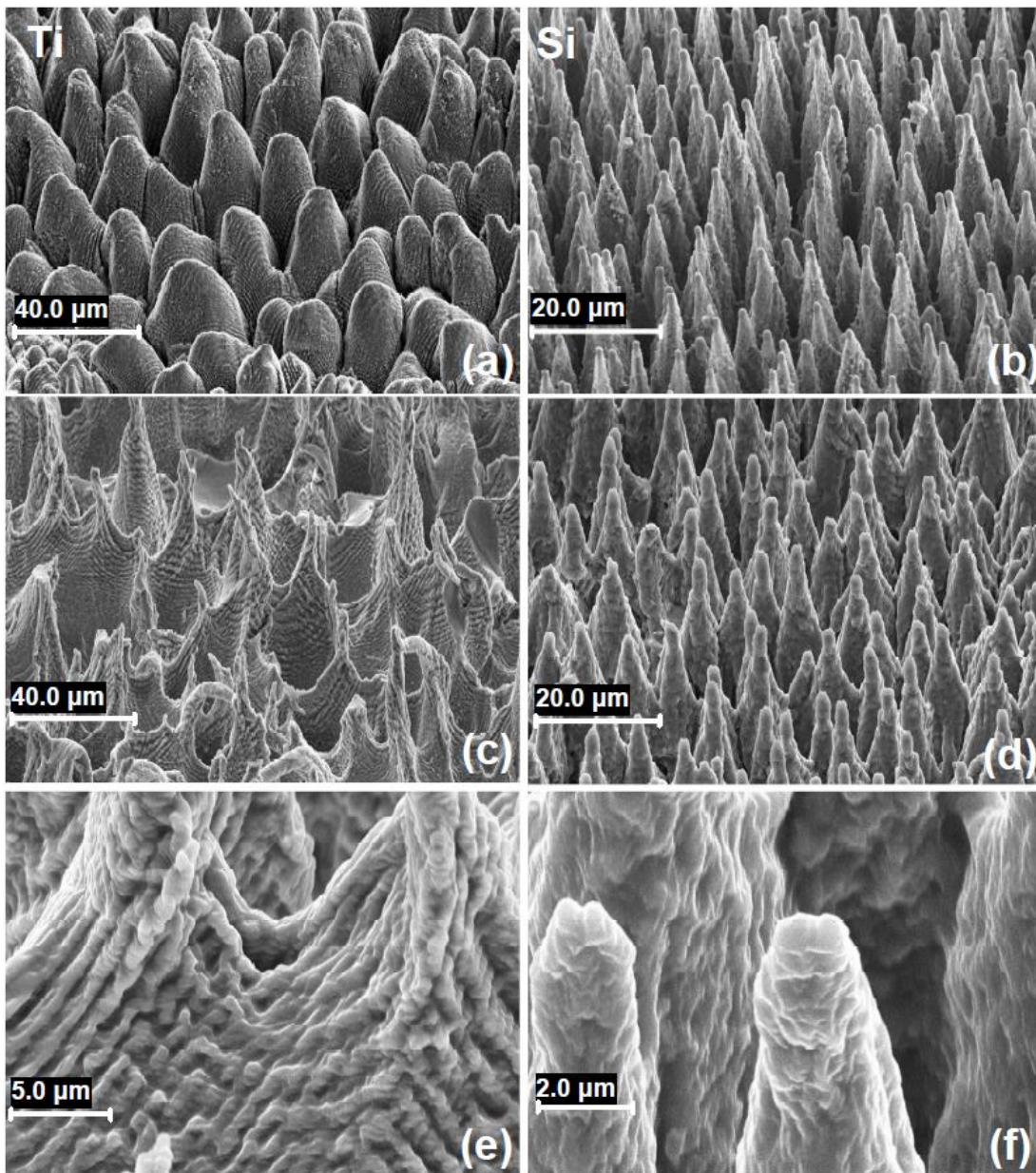


Figure 4.1-1. SEM image of: (a) Ultrafast laser treated surface showing the formation of micro/nano structures on Ti master, (b) Si master, (c) replication in PDMS of micro/nano structures that have been replicated from the Ti mold, (d) replication in PDMS of micro/nano structures from the Si master, (e) higher magnification image of PDMS showing detail micro/nano structures that have been replicated from the Ti mold, (f) higher magnification image of PDMS showing detail micro/nano structures that have been replicated from the Si mold.

As seen from figure 4.1-1 both Ti and Si master surfaces ((a) and (b)) were prepared by a Ti-Sapphire ultrafast laser system operating at wavelength of 800 nm and repetition rate of 1 KHz and a 130 fs pulse width. The laser fluence was kept constant at 0.8 J/cm² for the Si master and 1 J/cm² for the Ti master. Additional details of this self-assembled technique and the fabrication process can be found in the following references [37-39, 62]. The images in figure 4.1-1(c) and (d) respectively show the replicated PDMS surfaces fabricated from the Ti and Si masters. These results were produced using the simple replication technique discussed in Chapter 3 (see Figure 3-1). When comparing the replicated microtextured surfaces with their associated masters it can be seen that even the fine detail on the sides of the features are copied and that the detail copied is a mirror image of the microtexture from the master. This is especially evident in the case of Ti master and replicant where the conical boulder-like features of the master are copied as cup-shaped features on the replicant. When the samples of figure 4.1-1(c) and (d) are examined at higher magnification detail is seen at both the micron and nano scale as seen in figure 4.1-1(e) and (f).

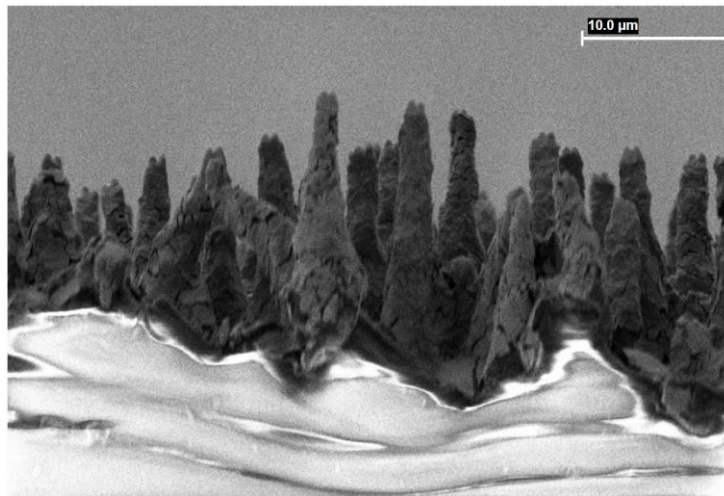


Figure 4.1-2. SEM image of cross section of PDMS microtexture replicated from Si master.

In order to quantify the dimensions of replicated microstructure a sample was prepared for cross section analysis under the SEM by coating 10 nm thin layer of gold and palladium and the image of figure 4.1-2 was obtained. The SEM image shows that the distance between the conical features is approximately 20 μm with height varying between 10 μm and 15 μm . Morphology of the replicated surface is controlled by controlling the morphology of the master. The master can be produced with varying microtexture heights. The heights varied from $\sim 1 \mu\text{m}$ to $\sim 35 \mu\text{m}$ which corresponded to Ti masters prepared according to [38, 39, 62] as outlined in section 4.3 where the fluence is held constant at 1.0 J/cm² for different number of laser shots between 0 and 450 [44] with the corresponding structure height between zero and 35.8 μm .

4.2. Optical properties

Optical measurements and characterization require a thin sample to minimize scattering effect so a sample was prepared using the PDMS embossing technique discussed in section 3-3 and shown in figure 3.2-2. As discussed earlier a representative sample produced using this technique is shown in figure 3.3-3. The replicated microtextured area is shown in the center of the sample.

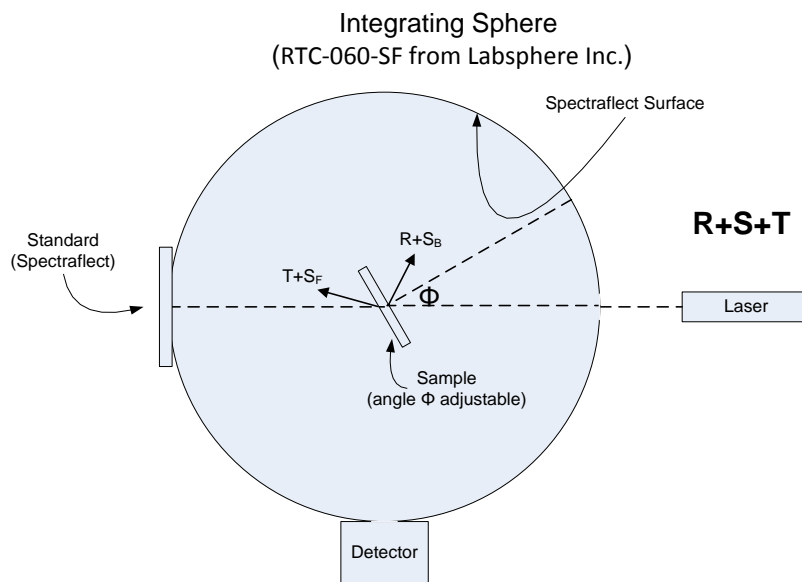


Figure 4.2-1. Optical characterization using integrating sphere showing total unabsorbed power transmitted (T) plus scattered (S_F) and reflected (R) plus scattered (S_B)

The optical properties of the PDMS microtextured surface were measured using an integrating sphere. The experimental setup is shown in figure 4-2-1. Using this apparatus the Total Integrated Light Scattering (TILS) power can be measured as shown. The light scattering power can be further broken down into the reflected plus backscattered power ($R+S_B$) as shown in Figure 4.2-2(a) below and the transmitted plus forward scattered power ($T+S_F$) as shown in Figure 4-4(c).

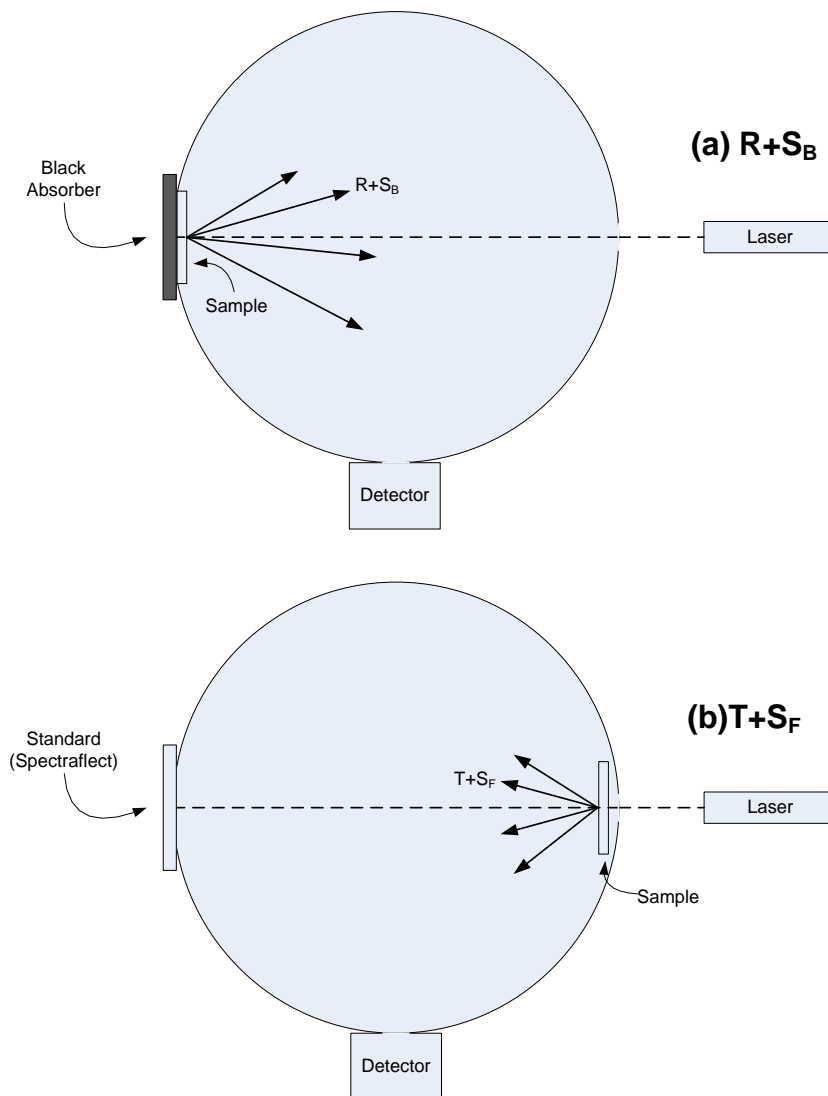


Figure 4.2-2. Optical characterization using integrating sphere showing: (a) the reflected (R) power plus the back scattered power (S_B), and (b) the transmitted (T) plus the forward scattered power (S_F).

The integrating sphere also allows the angle of incidence to be adjusted to determine the effect of the angle of incidence on the various reflected and transmitted components. The properties of the microtextured PDMS material are characterized to determine the dependence of reflectance on angle of incidence. For this experiment the transmitted light component is absorbed by a black absorber that was independently characterized. The black absorber reflected component is subtracted from the result for PDMS, and microtextured PDMS. A second experiment using the integrating sphere examines the light reflecting properties of the microtextured PDMS surface that was applied to a polished silicon surface. The results of these integrating sphere experiments are summarized in table 4.2-1.

Table 4.2-1. Optical characterization results from integrating sphere measurements carried out at 633 nm wavelength at normal incidence. The measurement error is 1-2%. The microtextured PDMS was placed with the microtextured side facing up on the Si substrate.

Sample type	T + S _F (%)	R + S _B (%)
PDMS Texture	96.2	4.9
Glass + microtextured PDMS	93.1	5.2
Silicon + PDMS	0	25.6
Silicon + microtextured PDMS	0	15.7
Textured Titanium	0	1.87
Textured Silicon	0	2.04

Of particular interest in Table 4.2-1 is the R+S_B data. The results for PDMS with microtexture on a polished silicon substrate are noteworthy since the reflectivity of uncoated polished Si is measured at 35% and is reduced to 25% with the addition of a 200 μm layer of PDMS. The reflectivity of Si is further reduced to 16% with the addition of PDMS microtextured film and

therefore reflection of the Si substrate is decreased by more than 55% by the application of this simple PDMS microtextured coating.

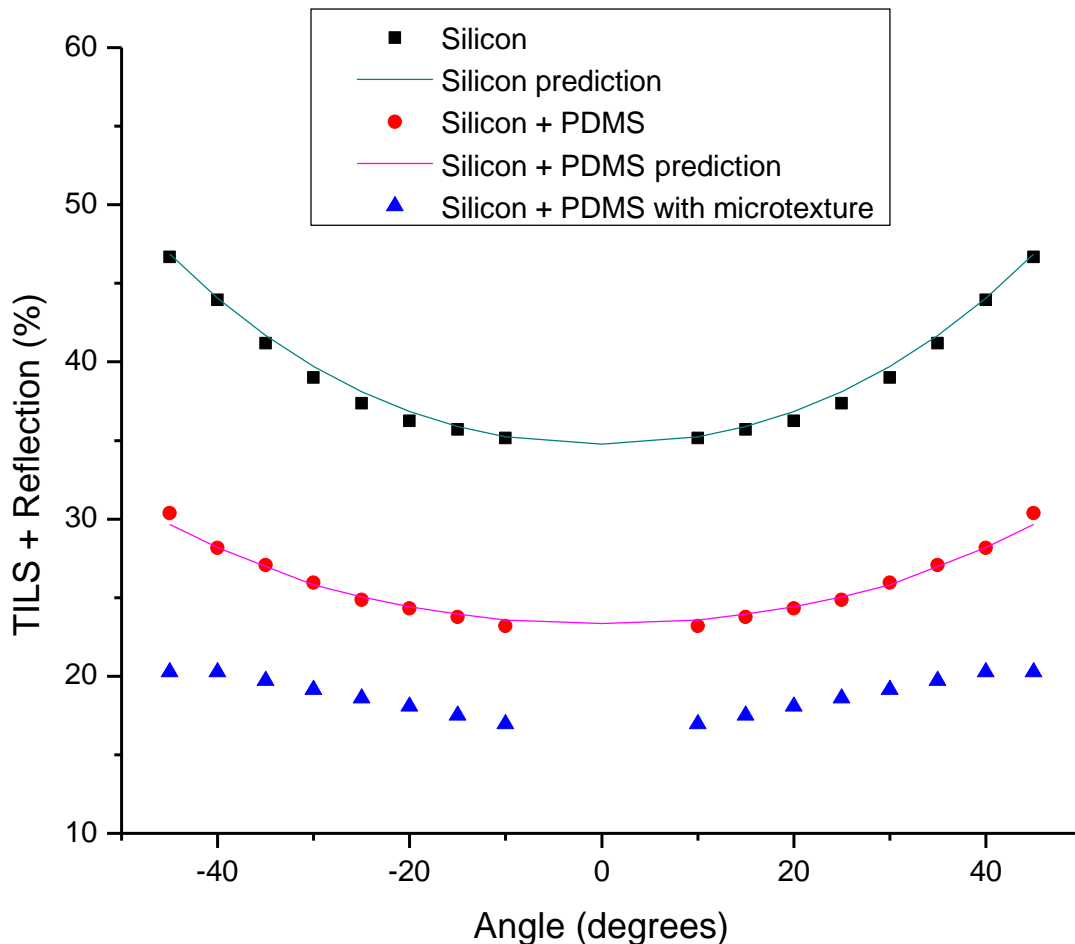


Figure 4.2-3. Total integrated light scattering and reflection as a function of angle at 633 nm wavelength for polished silicon, polished silicon prediction, silicon with PDMS film, silicon with PDMS film prediction, and silicon plus microtextured PDMS.

A microtextured PDMS sample was applied to a polished silicon substrate and was evaluated as a candidate for an antireflection coating for use in photovoltaic solar cells. The microtextured side of the PDMS was placed with the microtextured side face-up on the silicon substrate and TILS measurements are made using the integrating sphere apparatus. The results of this experiment are shown in figure 4.2-3 and the measured values are seen to compare well with the

values calculated from both a PV Optics model simulation [145] and MATLAB® program (see appendix 1). The data shows that the reflectivity is flat over a wide range of angles of incidence and the measured values are very close to the predicted values.

4.3. Contact angle measurement results and analysis

Figure 4.3-1 below (a-f) shows SEM imaging of replicated microtextured PDMS surfaces produced from masters with varying microtexture heights. The heights varied from $\sim 1 \mu\text{m}$ to $\sim 35 \mu\text{m}$ which corresponded to Ti masters prepared according to [38, 39, 62] as outlined in section 4.3.

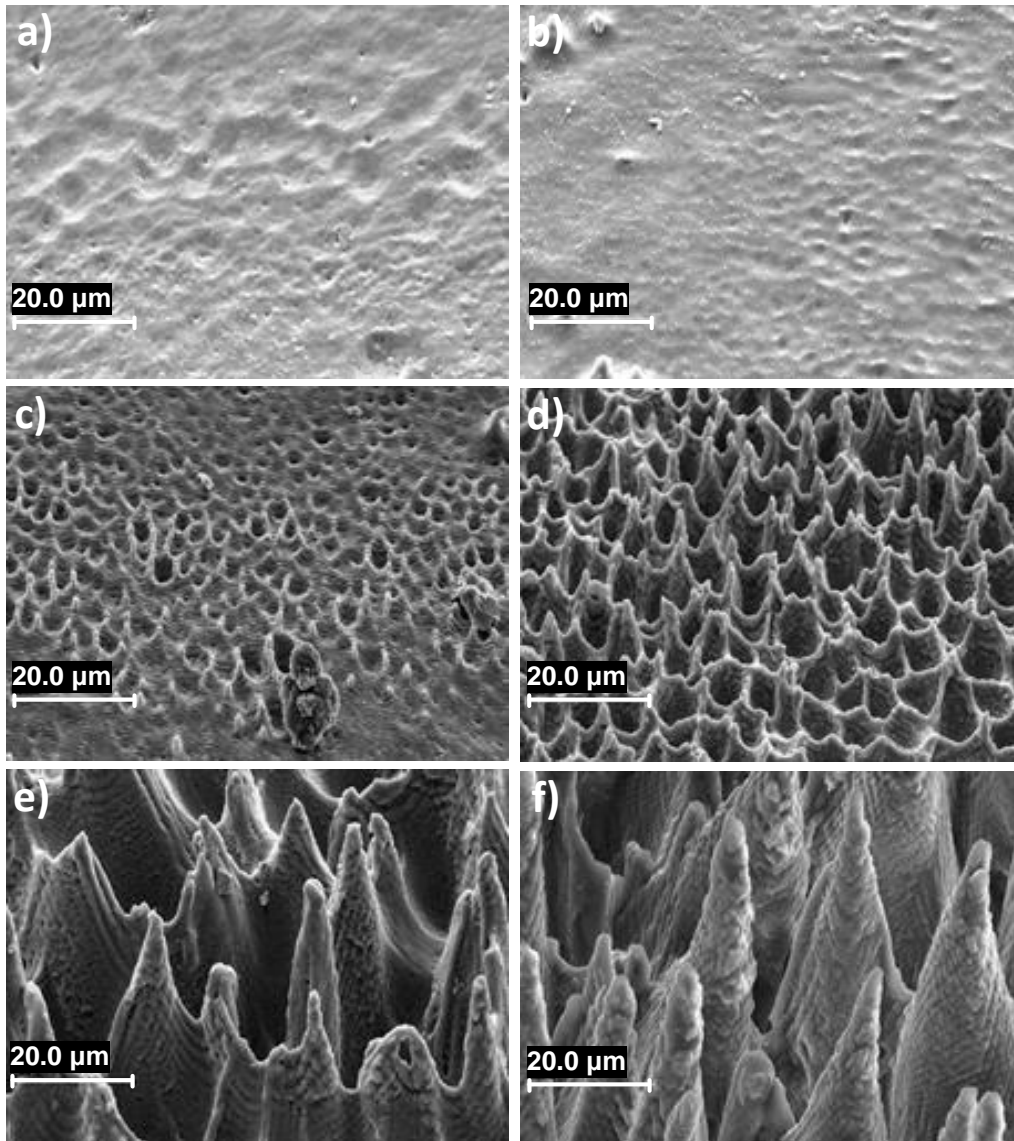


Figure 4.3-1. SEM images of replicated PDMS surfaces created from microtextured Ti masters prepared at laser fluence of 1.2 J/cm^2 for different number of laser shots (a) 60 (b) 125 (c) 175 (d) 250 (e) 350 (f) 450 [44].

The contact angle was measured on each of these surfaces according to the procedures outlined in section 3.3 and a plot is obtained that shows the relationship between microtexture height and contact angle as shown in Figure 4.3-2. Microtexture enhances the contact angle of the surface. For example the measured contact angle for plane PDMS surface was found to be 92° and after microtexture it increased to 154° for a microtexture height of $35.8 \mu\text{m}$. It is seen in this figure that there exists two distinct regions: a steep rising region for relatively lower height microtexture feature samples and a slower rising region for higher microtexture feature samples. It is known that appropriate surface roughness plays an important role in producing superhydrophobic surfaces [1, 2, 146] and that the addition of microtexture to a surface can increase or decrease the contact angle depending on the initial contact angle of the non-textured surface as was shown in section 2.4.

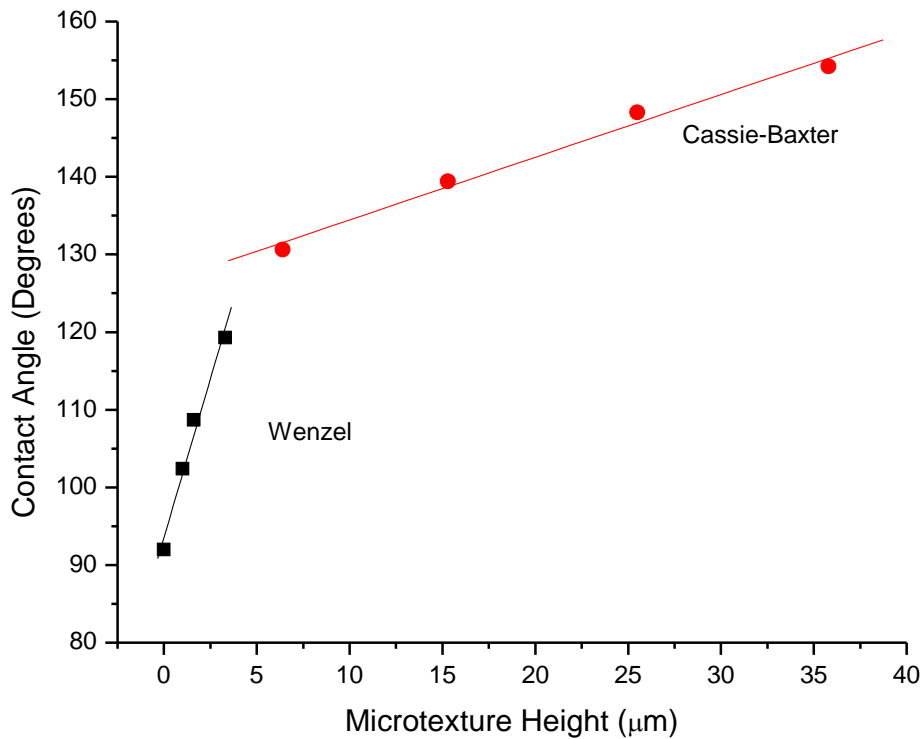


Figure 4.3-2. Variation of contact angle with microtexture height.

In chapter 2 Young's theory of surface wetting was introduced along with the Wenzel and Cassie-Baxter model. The Wenzel and Cassie-Baxter model can be employed to explain the two distinct regions in figure 4.3-2. These models repeated below in equations 4.3-1 and 4.3-2.

$$\cos \theta^* = r \cos \theta \quad (4.3-1)$$

$$\cos \theta^* = -1 + \Phi_s (1 + \cos \theta) \quad (4.3-2)$$

As before from chapter 2 in the Wenzel model θ^* is the observed contact angle for a drop on the surface, θ is called the equilibrium contact angle (the contact angle on a flat non-textured surface, and is also referred to as the Young's contact angle), r is the ratio of the surface area of the microtextured surface divided by the flat surface area. For the Cassie-Baxter model Φ_s is the fraction on the solid that is in contact with the liquid. With the Wenzel model, the liquid is in contact with the surface at all points and the hydrophobicity is increased because the interfacial area between the solid and the liquid increases. In the Cassie-Baxter model case the microtexture on the surface provides traps where the liquid is unable to penetrate so microtexture surface with features that are taller will behave according to the Cassie-Baxter region and a microtexture surface with shorter features will behave according to the Wenzel region. We can obtain an intersection threshold value θ_c that obeys both regimes by equating equations 4.3-1 and 4.3-2 giving:

$$\cos \theta_c = \frac{(\Phi_s - 1)}{(r - \Phi_s)} \quad (4.3-3)$$

By linear curve fitting the Cassie-Baxter and Wenzel lines (as shown in figure 4.3-2) and then solving the empirical equations, a threshold angle, θ_c is found to be $\sim 129^\circ$. From equation (4.3-1), for $\theta^* = 129^\circ$ and $\theta = 92^\circ$ (the measured value), we obtain a roughness factor, $r \sim 18$. Similarly, from equation (4.3-2), for $\theta^* = 129^\circ$ and $\theta = 92^\circ$, we obtain $\Phi_s \sim 0.38$. However, for CA of 154° , Φ_s is about 0.1; in this case the water drop is in contact with about 10% of the total area available. From solving two empirical equations obtained from fitting two straight line curves for Wenzel and Cassie regime we also get the transition microtexture height needed to enter Cassie

mode from Wenzel mode is about 4.2 μm . This transition at a microtexture height of 4.2 μm agrees well with the value of 4.5 μm reported by Yeh et al. using advancing and receding contact angle measurements [147] for microtextured surfaces.

As noted earlier in section 2.2 the Wenzel model is applicable for small values of the r factor. The reported r value at transition region using stylus profilometer have indicated a smaller number possibly due to difficulties in measurement of micro-scale deep structures [148].

Both contact angle and sliding angle are predictors of superhydrophobic behavior. The above analysis discusses contact angle, an experiment was also conducted to measure how sliding angle can be predicted from microtexture height. Table 4.3-1 below tabulates the results of the sliding angle experiments where we measured the sliding angle for samples with different microtexture heights.

Table 4.3-1. Sliding angle for water on replicated PDMS surface for different microtexture heights.

Texture height (μm)	Contact Angle (degrees)	Sliding Angle (degrees)
0	92	Pinned
1	102.4	Pinned
1.6	108.7	Pinned
3.3	119.3	Pinned
6.4	130.6	Pinned
15.3	139.4	<90
25.5	148.3	<15
35.8	154.2	<6

It can be seen that the drop is pinned (not mobile) for microtexture heights up to and including $\sim 6 \mu\text{m}$ which indicates that superhydrophobic behavior is associated with taller microtexture features. For taller microtexture features ($\sim 30 \mu\text{m}$) the sliding angle is less than 6° . This result is consistent with the Cassie-Baxter model as the tall microstructure features create the traps necessary to minimize the air-solid interface area [14].

The dynamic characteristics of water droplets were also studied for the replicated microtexture surface and the values for the advancing and receding dynamic contact angles were found to be 157° and 151° respectively for a sample with a microtexture height of $35.8\ \mu\text{m}$ giving a contact angle hysteresis of 6° .

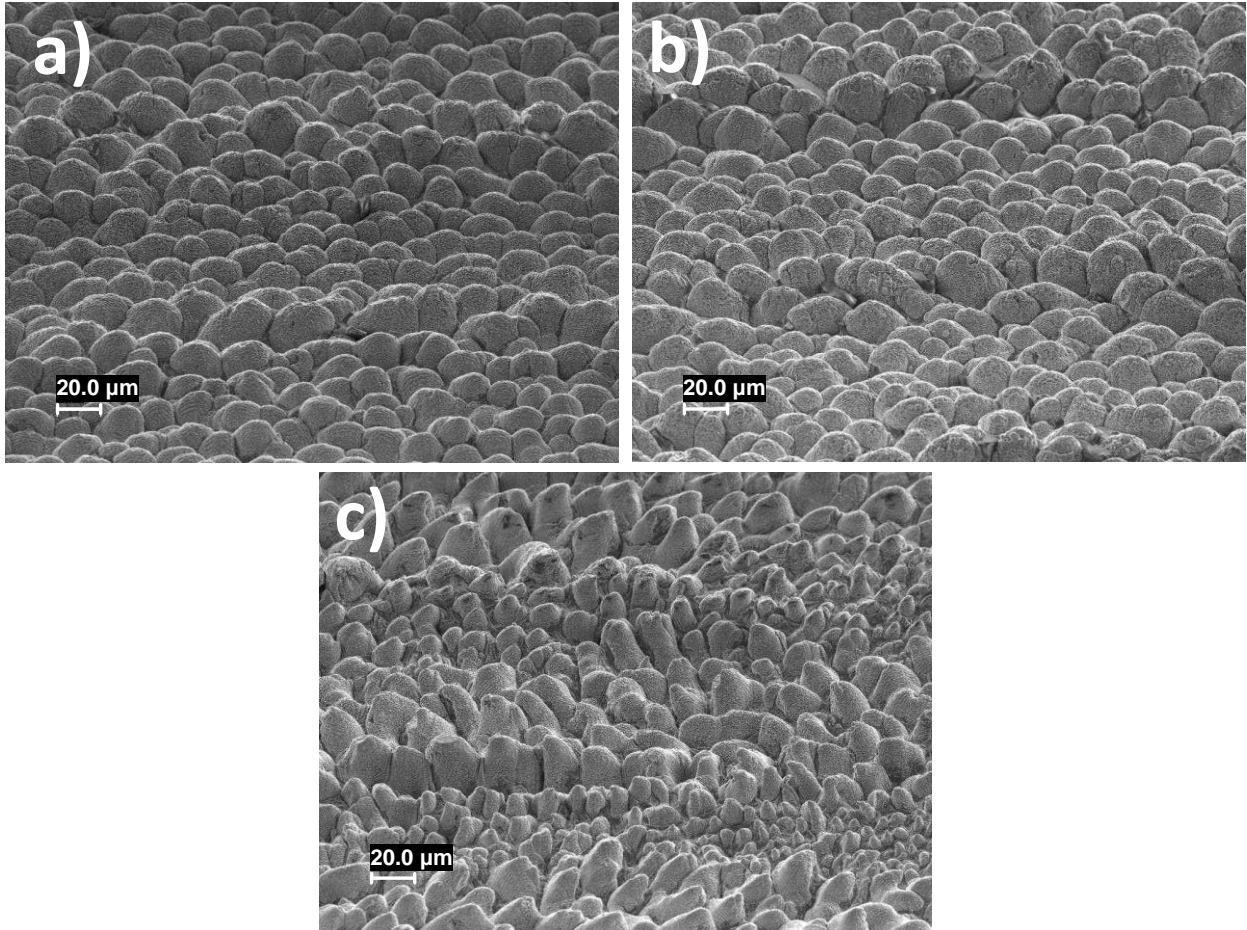


Figure 4.3-3. SEM image of Ti master after number of replications, (a) 5, (b) 10, and (c) 25.

Surface degradation of the master caused by repeated replications was investigated and the SEM images of Figure 4.3-3 were captured for masters with various numbers of replications. The analysis of the images shows no apparent degradation for up to 25 replications. There are several factors that can influence this lack of degradation but the main factors are the softness of the PDMS material compared to the hardness of the masters, the fact that no additional external loading was applied during the replication process and also the fact PDMS presents up to 3%

shrinkage [149] during the curing process which aids removal of the replicated surface from the master.

Details of the addition of MWCNTs into the PDMS polymer matrix were discussed in section 3.5. Although the primary purpose of such addition was to investigate the change in conductivity that is discussed in section 4.4, the changes to contact angle were also investigated. A series of samples were prepared with a range of MWCNT from 0.45 - 4.1 wt % bulk loading and found no evidence to support any hypothesis that the addition of MWCNTs to the PDMS polymer matrix affected contact angle within the accuracy of our equipment ($\sim 2\%$).

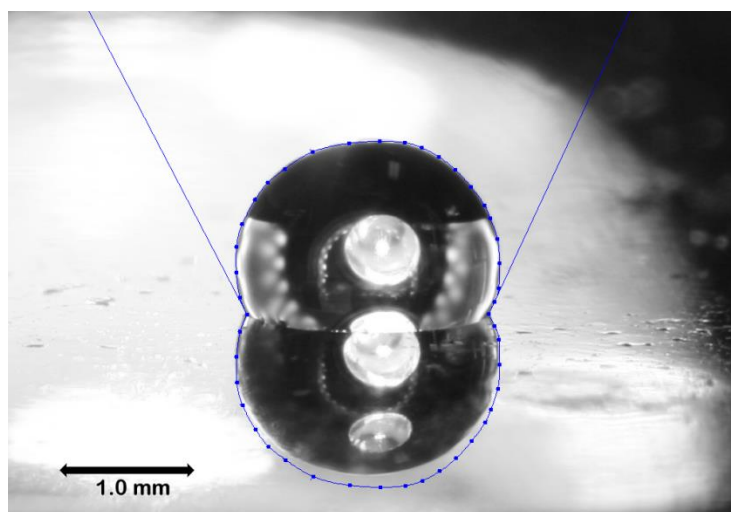


Figure 4.3-4. Image of water droplet on surface of non-textured conductive MW-CNT/PDMS composite.

A sample of conductive polymer was prepared without the addition of microtexture and was analyzed to determine contact angle similar to that shown in figure 4.3-4 and the contact angle was determined to be 110° with a contact angle hysteresis of 23° . Similarly figure 4.3-5 shows a microtextured PDMS-MWCNT nanocomposite sample being analyzed for contact angle and the results were found to have an advancing contact angle value of 161° with a sliding angle of 6° and a contact angle hysteresis of 3° . These results compare favorably with our earlier results for microtextured PDMS (no MWCNT) of 154° , 6° and 6° respectively [44], so the addition of 4.1 wt % loading of MWCNT did not enhance contact angle significantly.

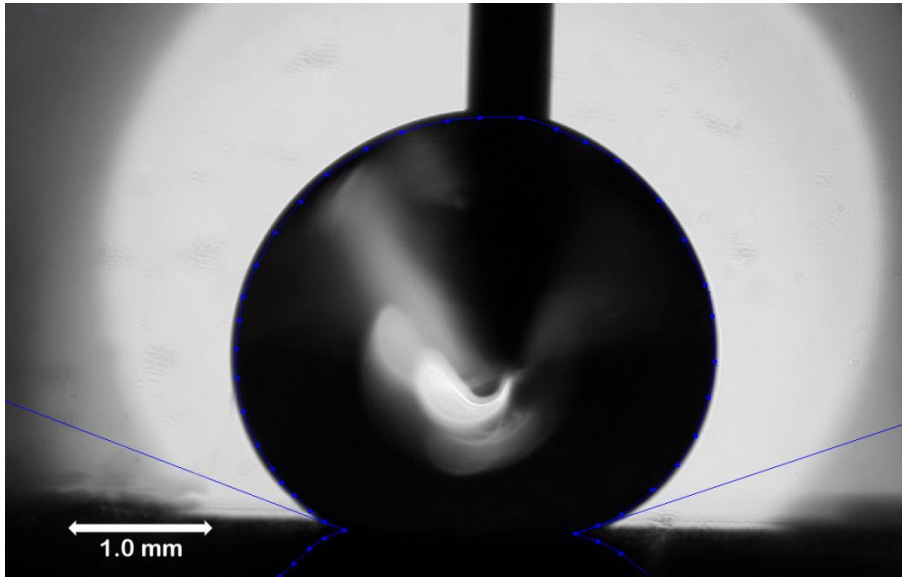


Figure 4.3-5. Image of water droplet on surface of conductive PDMS microtextured surface displaying a contact angle of 161°.

4.4. Electrical conductivity measurement results and analysis

As discussed in chapter 3, resistivity measurements are made in accordance with ASTM D-257 [142] using a Keithley 6105 resistivity adapter [141].

Table 4.4-1. MWCNT products.

Product	Length (μm)	Diameter (nm)	Structure	Packing Density (g/cm ³)	Resistivity at 1 %wt (Ω-cm)
PD15L15-20	15-20	15	Hollow	0.032	7 x 10 ⁴
BPD30	20	30	Bamboo	0.025	3 x 10 ⁴
PD30	20	30	Hollow	0.070	>2 x 10 ¹⁶
PD15L1-5	1-5	15	Hollow	0.100	>2 x 10 ¹⁶

Table 4.4-1 above summarizes the MWCNT parameters such as CNT lengths and diameters that were utilized to produce samples to determine the effect on conductivity by the addition of MWCNT to the PDMS polymer matrix. Both hollow and bamboo MWCNT products were

investigated and in total four different products were evaluated, the products differing mainly in packing density, which is seen to vary by a factor of four. The bamboo type product was evaluated as bamboo structure MWCNTs have been reported in literature as having a higher degree of structural defects [150, 151]. The MWCNT products with lower packing density were found to be more difficult to mix with PDMS and this in particular led to the selection of the PD15L15-20 product for conductivity experiments.

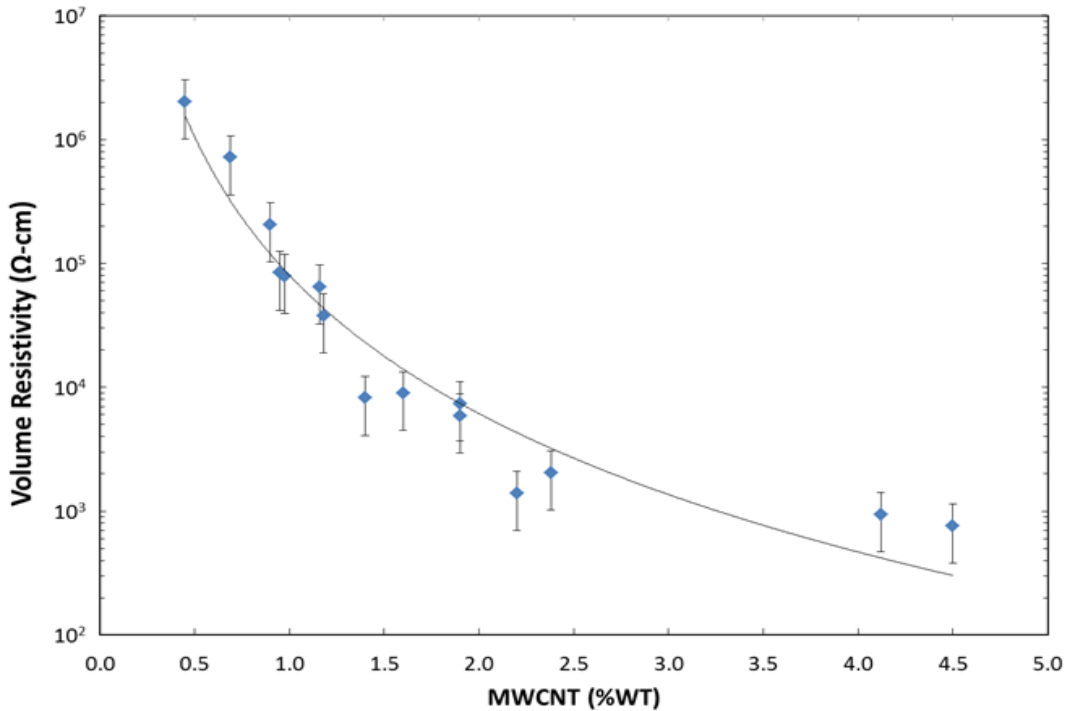


Figure 4.4-1. Graph of volume resistivity vs. % weight MWCNT loading (note: sample is non-textured).

Results are shown in Figure 4.4-1 above for the experiment measuring volume resistivity of these samples of PDMS nanocomposite with a bulk loading of between 0.45 and 4.4 wt % of MWCNT for the PD15L15-20 product. It was found that the minimum volume resistivity was 761 Ω cm. This result is significantly lower at low bulk loading levels (less than 5 %) to the results published by Engel et al. [152] by more than a factor of 100 and is lower to that of non-impregnated PDMS by a factor of more than 10^{11} .

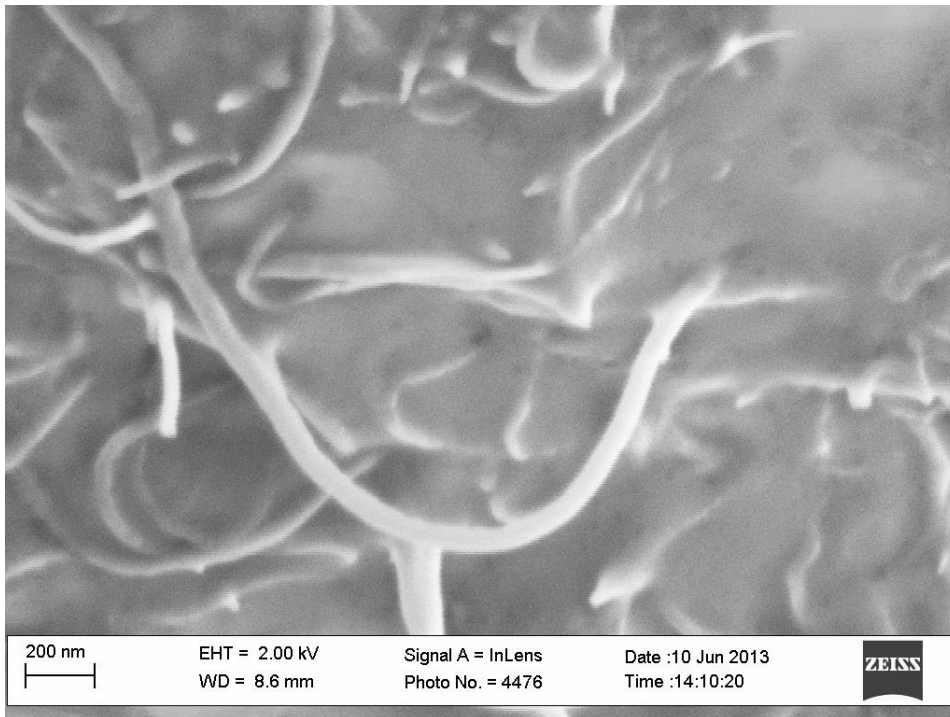


Figure 4.4-2. SEM image of conductive PDMS matrix showing interconnecting MWCNT.

Figure 4.4-2 above shows a high magnification SEM image of the PDMS-MWCNT nanocomposite sample with a 2.4 wt % bulk loading of PD15L15-20 that shows interconnection of the MWCNT's. This interconnection of the carbon nanotubes forms a network [68] that is responsible for the lower conductivity. At what has become known as the percolation threshold [68], a large increase in conductivity is seen due to the interconnection of the nanotubes, that can be seen in figure 4.4-2. After this percolation threshold, 2 wt % in our case from figure 4.4.-1, a significant exponential decrease in resistance can be seen in figure 4.4-1.

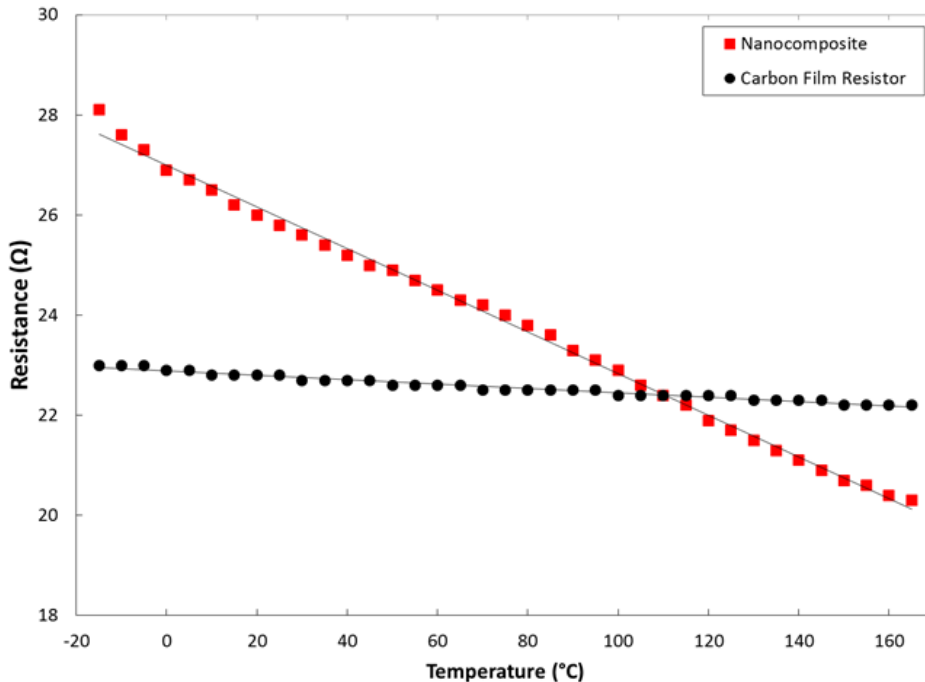


Figure 4.4-3. Graph of resistance vs. temperature for conducting nanocomposite and control resistor (note: nanocomposite sample is non-textured).

Nanocomposites based on BPD30, PD30, and PD15L1-5 failed to produce usable low resistance samples mainly due to inability to mix effectively so a study was performed using PD15L15-20 MWCNT to determine the temperature dependence on resistance for the resulting nanocomposite. The results of this study are shown above in figure 4.4-3. The nanocomposite for this experiment consisted of 4.1 wt % PD15L15-20 and the temperature was varied from -15°C to 165°C while resistance measurements were recorded. A 5% tolerance resistor was used as a control for this experiment and this control resistor exhibited a very small negative temperature coefficient (NTC) of resistance of $\alpha = 193 \times 10^{-6}$ (4.4 mΩ/K). The MWCNT nanocomposite by comparison has a NTC of $\alpha = 1.43 \times 10^{-3}$ (35.5 mΩ/K). Performing a literature search for the temperature coefficient of resistance for a platinum thermistor finds a positive temperature coefficient (PTC) of resistance of $\alpha = 3.7 \times 10^{-3}$ [79]. Platinum is very desirable for this application because of its linear response, however due to the expense of platinum, cheaper alternatives such as semiconductor thermistors have become popular despite a non-linear response. In comparison the NTC response of the PDMS-MWCNT nanocomposite of Figure 4.4-3 is linear within the tested range and the broad operating range of PDMS (-55°C to 200°C) with

long lifetime in harsh conditions (PDMS is used as a solar cell encapsulant) makes the PDMS MWCNT nanocomposite an attractive material where temperature sensing is required in addition to other properties.

4.5. Electrowetting results and analysis

Young's equation was introduced in chapter 2 and is repeated below as equation 4.5-1. Young's equation can be used calculate the contact angle of a liquid on a solid non-textured surface

$$\cos\theta = \frac{\gamma_{SV} - \gamma_{SL}}{\gamma_{LV}} \quad (4.5-1)$$

In this context θ represents the contact angle, sometimes referred to as the Young's contact angle and the three interfacial forces are γ_{SV} which represents the surface-vapor interface, γ_{SL} is the surface-liquid interface and γ_{LV} is the liquid-vapor interface.

For this work on electrowetting we are mainly concerned with the interaction of liquid water on a solid PDMS surface. Therefore, to quantify Young's equation for this condition we can place numeric values into Young's equation using values of γ_{SV} of 24 mN/m[120], γ_{SL} of 41 mN/m[120], and γ_{LV} of 72.8 mN/m[100] we obtain a distilled water-PDMS contact angle of 102.7° which is well in agreement with the range reported by Ismail [120].

Lippmann is credited [101] as being the first to report that an electrostatic charge can change the contact angle at a solid-liquid interface [102]. Electrowetting phenomena are explained by the addition of a modification to Young's equation [103, 133, 153, 154] that adds a force to modify the surface tension as in eq. 4.5-2.

$$\cos\theta = \frac{\gamma_{SV} - \gamma_{SL}}{\gamma_{LV}} = \cos\theta_0 + \frac{1}{2} \frac{CV^2}{\gamma_{LV}} \quad (4.5-2)$$

This modification is on the order of CV^2 where $C = \epsilon/d$ and V is the applied electrowetting potential. C is the capacitance per unit area, and ϵ is the permittivity of the material, in this case PDMS. θ_0 is the initial contact angle or the Young's contact angle. For rough or microtextured surfaces Young's equation no longer applies and one must apply either the Wenzel model (eq. 4.5-3) [121] or the Cassie-Baxter model (eq. 4.5-4) [134] as explained in chapter 2. In the

Wenzel model the Young's contact angle is modified by a roughness factor r , a multiplication factor that represents the surface roughness area divided by the geometric surface area

$$\cos \theta^* = r \cos \theta_c \quad (4.5-3)$$

Here θ^* is the apparent contact angle, θ_c is the equilibrium contact angle or Young's contact angle. As with Young's theory an example helps to make the application of Wenzel's model clear. If we, for example, assume a Wenzel roughness factor of 2, meaning that the roughness doubles the surface area, then using this value of r in eq. 4.5-3 and using the value of Young's contact angle calculated above of 102.7° , this gives an apparent contact angle of 116.1° .

$$\cos \theta^* = -1 + \phi_s (1 + \cos \theta_c) \quad (4.5-4)$$

The Cassie-Baxter model is shown above in eq. 3. With this model, the liquid is no longer in complete contact with the solid but is partly supported by the surface tension of the liquid. Φ_s is a dimensionless number that represents fraction of solid in contact with the liquid, θ_c is called the effective contact angle and is also the Young's contact angle and θ^* is the observed contact angle.

In a similar way to Young's model, the Cassie-Baxter model can be expanded to include electrowetting phenomena [155] as in eq. 4.5-5 where β represents the Cassie-Baxter fraction of solid in contact with liquid, as above $C = \epsilon/d$, V is the applied electrowetting potential, C is the capacitance per unit area, and ϵ is the permittivity of the material.

$$\cos \theta = \cos \theta_o + \frac{1}{2} \frac{\beta C V^2}{\gamma_{LV}} \quad (4.5-5)$$

Figure 4.5-2 shows images captured from video for textured (a) and (b) and non-textured PDMS (c) and (d). In this figure the samples are manufactured from PDMS without the addition of nanomaterials. For each set of images, the first image is taken before the excitation voltage is applied. It can be clearly seen that the change in excitation voltage from 0 V to 2 KV has a greater effect on the contact angle for the textured sample where the CA changes from 162° to 144° , compared to that of the non-textured sample where the CA changes from 111° to 112° .

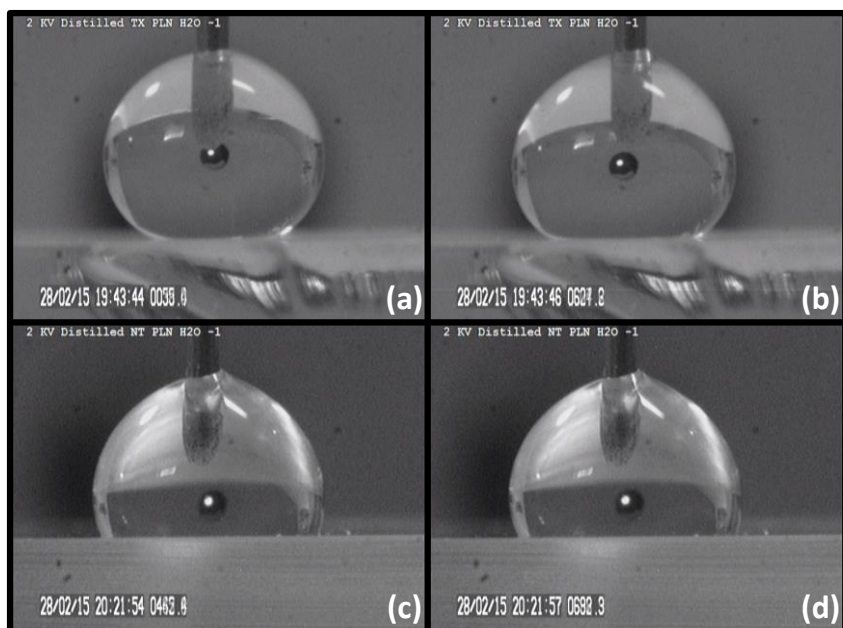


Figure 4.5-2. Images captured from video for distilled water droplet on microtextured (a) and (b) and non-textured PDMS (c) and (d).

Similarly Figure 4.5-3 shows images captured from video for microtextured (a) and (b) and non-textured PDMS nanocomposite (c) and (d). For each set of images the first image is taken before the excitation voltage is applied. Again it can be clearly seen that the change in excitation voltage from 0 V to 800 V has a greater effect on the contact angle of the textured sample where the CA changes from 158° to 139°, compared to contact angle of the non-textured sample where the CA changes from 94° to 91°. It should be noted that the PDMS nanocomposite sample shows little or no reversible electrowetting behavior, and that the excitation voltage for the nanocomposite testing was limited to 800 V to limit the creation of bubbles due to electrolysis.

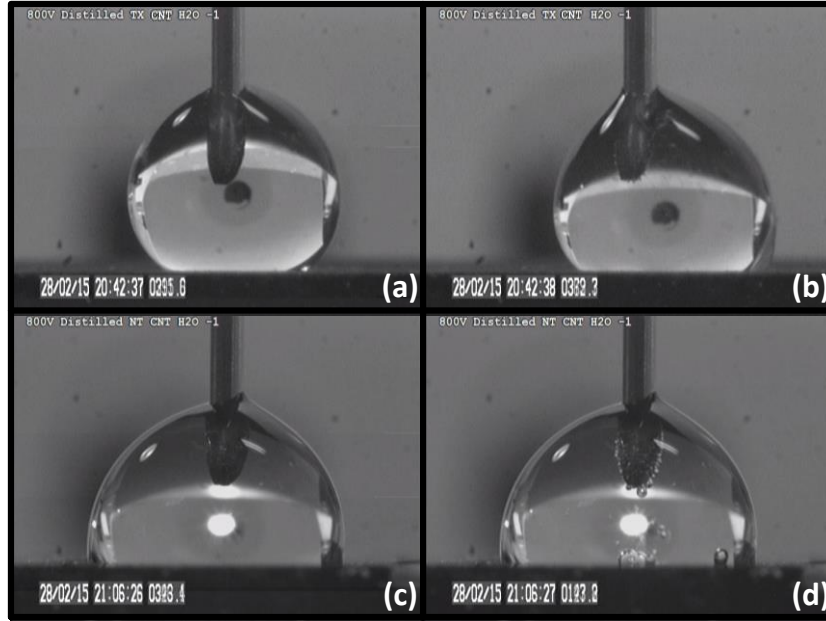


Figure 4.5-3. Images captured from video for distilled water droplet on textured (a) and (b) and non-textured PDMS conductive nanocomposite (c) and (d).

Figure 4.5-4 shows how contact angle for microtextured and non-textured PDMS vary as the applied voltage is increased from 0 V to 2000 V, the textured and non-textured up data sets, and returned to 0 V the textured and non-textured dn data sets. Figure 4.5-5 similarly shows the response for microtextured and non-textured MWCNT-PDMS nanocomposite as the voltage is increased from 0 V to 800 V and returned to 0 V.

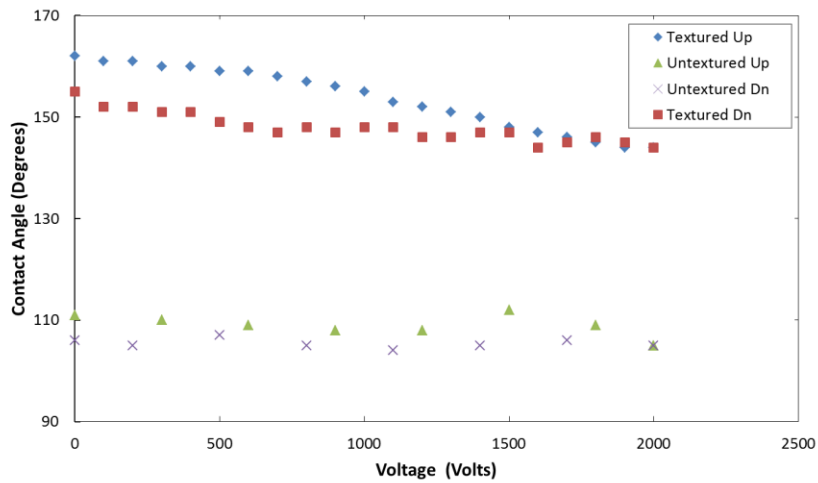


Figure 4.5-4. Graph of contact angles for distilled water droplet on PDMS as a function of voltage

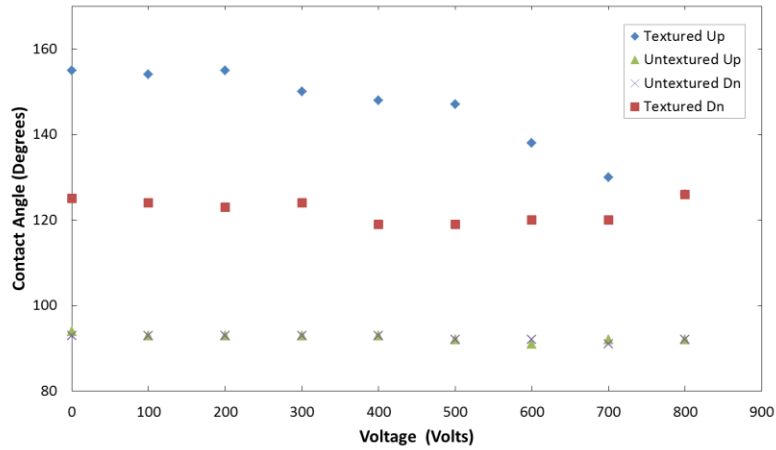


Figure 4.5-5. Graph of contact angles for distilled water droplet on PDMS conductive nanocomposite as a function of voltage

For the measurements presented in figure 4.5-4 and 4.5-5 distilled water is used during the experiment. For figure 4.5-6 and 4.5-7 the same experiment repeated for a 0.05 M solution of NaCl used to simulate biological saline solutions interfacing to the microtextured surfaces similar to Han et al. [81].

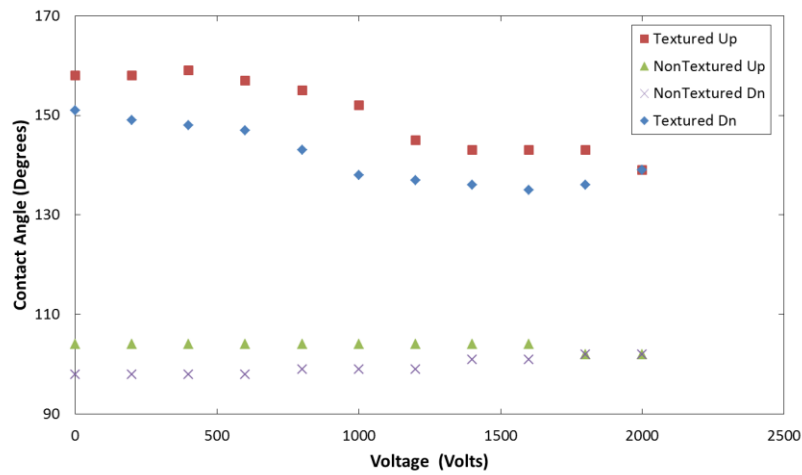


Figure 4.5-6. Graph of contact angles for 0.05 M solution NaCl droplet on PDMS as a function of voltage

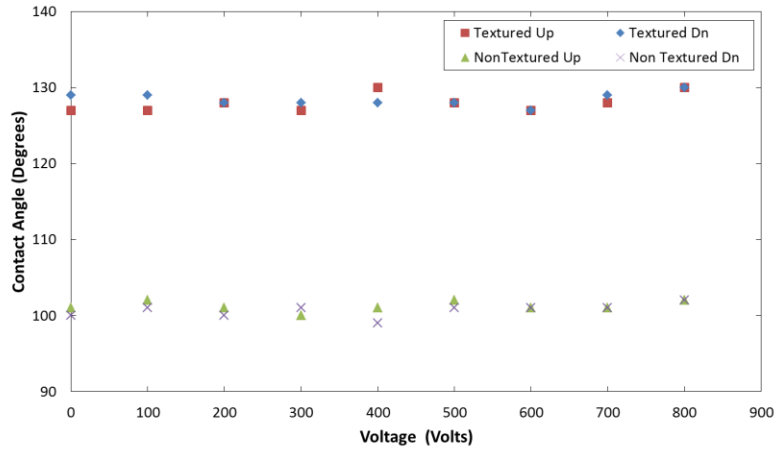


Figure 4.5-6. Graph of results for contact angles for 0.05 M solution NaCl droplet on PDMS conductive nanocomposite vs. voltage

Looking at the measured data for textured PDMS which is the textured up curve of Figure 4, and substituting values into eq. 4.5-5 with θ , the final CA = 144° , θ_s the initial CA = 162° , $V = 2000$ V, $\gamma_{SA} = 24$ N/m [120] and $\beta = 0.1$ from our earlier work [44] we find a value for C of 17.04 nF and can then develop a model for the system using eq. 4.5-5 as we change the voltage from 0 V to 2000 V as shown expanded in figure 8. The value for the capacitance of the droplet-PDMS dielectric combination of 17.04 nF is identical to the value obtained by Zhu et al. [100] for aligned carbon nanotube films and is significantly larger, as expected, than the value of 21 pF developed by Verheijen et al. [154] for a non-textured surface with a 90° contact angle.

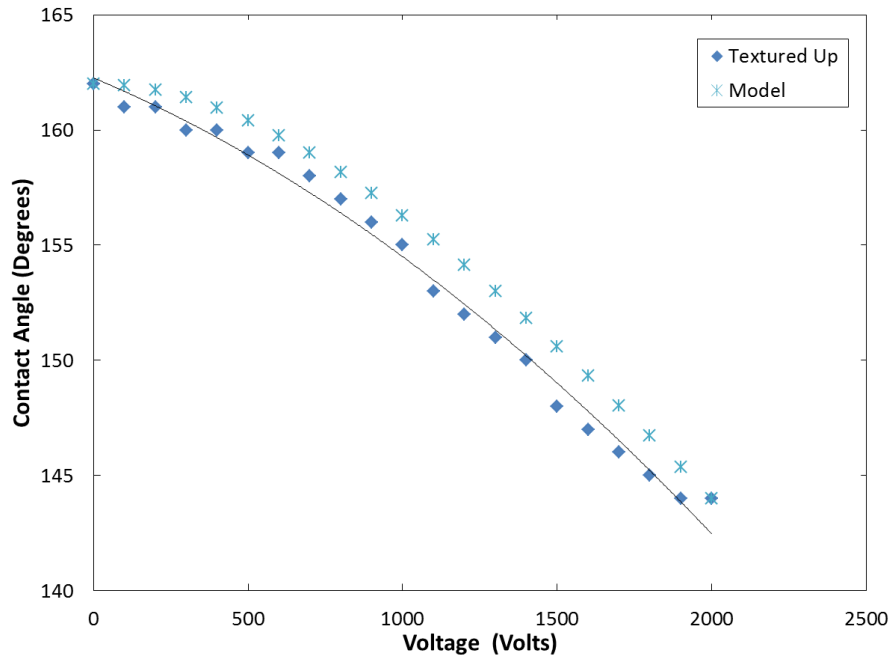


Figure 4.5-8. Graph of results for contact angles for distilled water droplet on PDMS vs. voltage and prediction from model.

The response shown in figure 4.5-4 is repeatable and the drop can be seen to move down as the voltage is increased and move back to the original position after the initial pass. The initial pass condition is explained by the contact angle hysteresis between the advancing and receding contact angles. As discussed earlier in the literature search, this reversible electrowetting behavior has been observed in other surfaces and fluid combinations, but only in limited circumstances such as with the addition of oil [93] or heating of the substrate [26] or by the use of special coatings [86, 91, 94] and more lately on silicon nanofibers [93] and silicon nanowires[92].

An analysis was performed to determine the dynamic performance of the system to AC high voltage. The test fixture of figure 3.7-1 was modified similar to figure 4.5-5 with the high voltage power supply modulated by the 0 – 10 V output from the signal generator. The camera and stroboscope tachometer were used to verify the drop oscillation frequency.

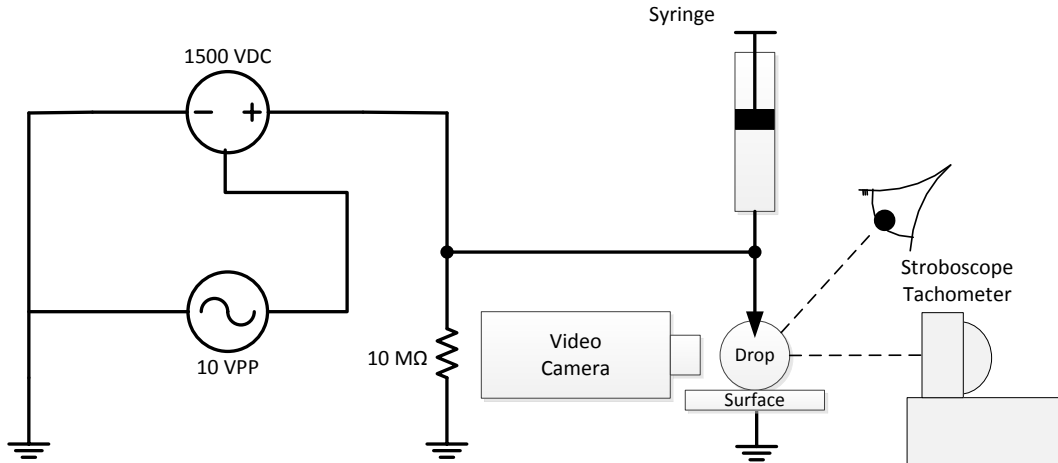


Figure 4.5-5. Test apparatus used to generate 1.0 Hz excitation for electrojetting testing.

The results shown in table 4.5-1 were obtained with the signal generator set to a 1.0 Hz frequency.

Table 4.5-1. Drop height and contact angle repeated changes for 1.0 Hz 1.5 KV excitation.

Voltage (V)	Drop Height (mm)	Contact Angle (degrees)
0	2.16	148
1500	2.05	137

This test results suggest an application described in the future work section such as that of figure A3-3 in appendix 3 where a laser can be modulated by an externally controller variable frequency. An analysis of the design difficulties of such a test fixture is included.

4.6. Contact angle measurements for different fluids

Surfaces with a high degree of microtexture have demonstrated resilience to ice buildup [156]. This potential use of the microtextured superhydrophobic surface that was discussed in chapter

4.3 is for anti-icing for the aviation industry where much expense is currently employed in the distribution and use of anti-icing equipment and supplies. In chapter 1 we described that a busy airport can spend over \$1,000,000 per day on de-icing equipment, manpower and fluid [110]. With this potential application in mind an analysis was performed on a selection of fluids that might be found at a typical airport and in particular types of fluids used for de-icing [157].



Figure 4.6-1. Typical fluids that might be found at an airfield.

These fluids were analyzed using the contact angle goniometer and the table of results below was produced that shows both advancing and receding contact angle and sliding angle where measured. The advancing contact angles can be used as the static contact angle if needed.

Table 4.6-1. Contact angle and sliding angle of typical fluids.

Sample	Advancing CA	Receding CA	Sliding Angle
Water (Distilled)	161.3	157.0	4°
Kerosene	wets	wets	-
Gasoline	wets	wets	-
Ethyl Alcohol	84.5	68.9	25°
Isopropyl Alcohol	wets	wets	-
Oil (10W30)	81.4	50	25°
Naphtha	wets	wets	-
Ethylene Glycol 50%	144.2	134.3	25°

Looking at Table 4.6-1 it can be seen that the microtextured PDMS surface is only superhydrophobic for water, degrades to hydrophobic for ethylene glycol and shows oleophilic behavior for the common oils and hydrocarbons tested above. The oleophilic response of the microtextured PDMS to hydrocarbon oils is expected to enhance its hydrophobic behavior since such oils are typically used to enhance hydrophobic behavior [92, 93, 133].

4.7. Durability of microtextured surfaces

The mechanical durability of the pulsed laser microtextured surface was investigated by Steele et al. [158]. A titanium master was prepared and coated with a fluoropolymer to produce a superhydrophobic microtextured surface with a contact angle of about 165°. The surface was then subjected to repeated abrasive wear testing and the contact angle was found to degrade below 150° after three abrasive testing cycles of 350 g load. This reduction in contact angle can be explained by the abrasive removal of the hydrophobic fluoropolymer coating exposing the hydrophilic titanium surface and the breaking of the microtexture. The degradation of the master due to multiple replications has been examined in our earlier work [44] and was determined to be minimal for up to 25 repetition cycles (see figure 4.3-3). It was discussed earlier in section 3.1 that the environmental stability (exposure to UV light primarily) is one of the key factors why PDMS is used as a solar cell encapsulant to produce modules. Premium solar panels are guaranteed for up to 25 years. A laser microtextured replicated sample was provided to PBI

Corporation, a major satellite dish antenna manufacturer, for UV stability test to simulate outdoor sun exposure. Test results showed no measurable degradation after three and a half years of equivalent sun exposure.

Chapter 5. Conclusions and Future work

5.1. Key findings

The first key finding of this research is that laser generated surface microtexture can be replicated to a high degree of fidelity using a very simple and inexpensive technique that is readily scalable to industrial applications. An experimental setup was designed to measure wetting properties and it was found that the replicated microtextured surface displays superhydrophobic properties. The results were analyzed using the Wenzel and Cassie-Baxter models and it was found that minimum texture height of about 4.2 μm is needed for the replicated surfaces to enter into the Cassie-Baxter regime. Having a high static contact angle in the Cassie-Baxter region combined with a low value of contact angle hysteresis and a low sliding angle would help in achieving anti-icing and anti-corrosion properties [4, 8, 9, 124]. No additional processing such as coatings are required to achieve contact angles greater than 161°. It was also found that the contact angle can be controlled by changing the height of the replicated microtexture. The optical properties of the replicated microtexture were analyzed and it was found that the replicated microtextured PDMS, when applied on a silicon surface showed that surface reflectance can be suppressed over 55% compared to the control value. The process demonstrated is directly applicable to other polymer and plastic materials and has since been demonstrated on polycarbonate by other members of our research group [105]. Another key finding is that we can take the aforementioned microtextured PDMS surface and the addition of multi-walled carbon nanotubes to the polymer matrix can produce a superhydrophobic and conductive nanocomposite that when analyzed for its wetting properties was found to retain the superhydrophobic properties of the PDMS microtextured surface. This superhydrophobic nanocomposite demonstrated a huge increase in conductivity of more than 10^{11} over the base polymer with a bulk loading of less than 5 wt % with an operating temperature range from -15°C to 165°C and a negative temperature coefficient of resistance of $\alpha = 1.43 \times 10^{-3}$ (35.5 m Ω /K). The combined characteristics of a conductive, superhydrophobic nanocomposite with linear temperature coefficient of resistance have exciting potential for applications in the packaging area.

This research has provided a better understanding of superhydrophobic properties of microtextured surfaces. This understanding and demonstration of extremely high contact angle, low sliding angle and low hysteresis would help in applications of microtextured superhydrophobic surfaces for anti-icing, anti-corrosion, self-cleaning and anti-biofouling etc.

The electrowetting properties of the non-impregnated replicated microtextured surface demonstrate greater than 10° of reversible electrowetting behavior without the use of additional oils or coatings and suggest applications for MEMS. The microtextured nanocomposite surface was not found to be a useful surface for demonstrating electrowetting phenomena.

These superhydrophobic surfaces also demonstrates a small contact angle hysteresis of 6° and low sliding angle of 6° both known as predictors of anti-icing properties. The combined characteristics of these surfaces suggest many applications including anti icing, anti-biofouling, smart electrically shielded enclosures with internal electronic temperature sensing, electro mechanic actuators and as a surface coating to improve the efficiency and cleaning properties of solar power modules.

5.2. Future work

Further improvement in the antireflection properties of the PDMS microtextured surface on silicon can be expected by finding a similar material to PDMS with a refractive index closer to 1.75 – 2.0. This material will be expected to have a refractive index close to 1.95 by the formula $n_2 = \sqrt{n_1 n_3}$ where n_1 is the refractive index of air (1.0) and n_3 is the refractive index of silicon (3.874) [159]. This will provide low reflectance over a broad wavelength and angular range.

The light-coupling phenomenon discussed in chapter 4 from the integrating sphere experiments where light is coupled by the surface texture and effectively wave-guides through the PDMS media should be investigated for possible use as a fiber-optic coupling device.

Some initial investigation was performed on the replicated microtextured surface to determine the effectiveness of the material as a light diffuser and to examine the scattering properties.

The electrowetting investigation can be expanded to other microtextured surfaces including polycarbonate suggested by our research team in recent work [105] that demonstrates microtexture replication and superhydrophobic properties..

In section 3.8 we demonstrated electrowetting behavior for replicated microtextured surfaces and further suggested applications in the area of electromechanical systems to control high speed movement of a drop with possible application as a high speed shutter for laser systems. One difficulty of such an application is how to control or modulate the high voltage power supply to achieve response times faster than 1 Hz using the Stanford Research Systems PS325 being driven by the 0 – 10V output of the Stanford Research Systems DS345 synthesized function generator. When we originally set up the test system of figure 4.5-5 we found that the frequency response was limited to approximately 2.0 Hz by the slew rate on the input of the PS325 (The PS325 has an external voltage set maximum update rate of 16 Hz with a maximum slew rate of 0.3s for zero to full scale [160]). A discrete circuit should be built to modulate the output of the PS325 with a frequency response as fast as 1KHz so the dynamic frequency response of the electrowetting system can be investigated at these frequencies. Details of this test fixture design are included in appendix 3.

Anti-icing and anti-corrosion are two additional aspects of this thesis that have been discussed as potential applications of superhydrophobic microtextured surfaces but have not as yet been fully demonstrated. Work has been done on fabrication of washers out of microtextured PDMS film with the aim of providing an anti-corrosive demonstration and that work is ongoing, see figure 5.2-1. Anti-icing as an application has been tested on the small scale in the laboratory, targeting the satellite dish antenna market however, due to lack of large size samples no data is yet available on actual field test.



Figure 5.2-1. Washers made from microtextured PDMS film for corrosion prevention.

List of Publications

- P. O. Caffrey, B. K. Nayak, and M. C. Gupta, "Ultrafast laser-induced microstructure/nanostructure replication and optical properties," *Appl. Opt.*, vol. 51, pp. 604-609, 2012.
- B. K. Nayak, P. O. Caffrey, C. R. Speck, and M. C. Gupta, "Superhydrophobic surfaces by replication of micro/nano-structures fabricated by ultrafast-laser-microtexturing," *Applied Surface Science*, vol. 266, pp. 27-32, 2013.
- P. O. Caffrey and M. C. Gupta, "Electrically conducting superhydrophobic microtextured carbon nanotube nanocomposite," *Applied Surface Science*, vol. 314, pp. 40-45, 2014.

Patents

- M. C. Gupta, B. K. Nayak, and P. Caffrey, "Ultrafast laser induced micro/nano structures replication and optical properties and related method", U.S. Provisional Patent Application No. US 20130189485 A1, 2013.
- P.O. Caffrey, "Wind turbine with wireless pitch control", U.S. Patent No. US 8202050 B2, 2012.
- P.O. Caffrey, J.A. Petzen, D.B. King, F.L. Kerr, "Control systems and method of providing the same", U.S. Patent No. US 8315718 B2, 2012.
- P.O. Caffrey, W.B. Noto, J. Middendorf, Systems and methods for monitoring and controlling wind turbines within a wind farm, U.S. Patent Application, 2014.
- P.O. Caffrey, A. Galbraith, K. Kuruvilla, "Systems and methods for adaptive possible power determination in power generating systems", U.S. Patent Application No. US 20130096856 A1, 2011.
- P.O. Caffrey, W. Pearson, J. Casteel, D. Fowley, Web-based operator control interface to generator control systems, U.S. Patent Application No. US 20130018490 A1, 2013.
- P. O. Caffrey, M. Daniels, and M. Asfaw, "Loop containment enhancement", U.S. Patent Application No. US 20130176893 A1, 2013.
- P. O. Caffrey, and J. Selvey, "Dynamic virtual LANs to segregate data", U.S. Patent Application No. US 20130177022 A1, 2013.

- P. O. Caffrey, M. Asfaw, A. Bhatt, and K. Mazumder, "Redundant ethernet connection system and method", U.S. Patent Application No. US 20130177022 A1, 2013.
- P. Caffrey, W. Noto, J. Hagmann, "System and method for monitoring and controlling wind turbines within a wind farm", U.S. Patent Application No. US 20140521661, 2014.
- P. Caffrey, W. Noto, D. Korim, M. Shah, "Automatic deployment of code", U.S. Patent Application No. US 20150019208, 2015.
- P. Caffrey, W. Noto, T. Cribbs, C. Tschappatt, "Autonomous yaw control for a wind turbine", U.S. Patent Application No. US 14702997, 2015.

Presentations

- P. Caffrey, Layer-2 or bust! 2011 Mission critical network design seminar, Dallas TX, 2011. (Keynote Speaker along with Eric Byres)

References

- [1] A. Lafuma and D. Quere, "Superhydrophobic states," *Nat Mater*, vol. 2, pp. 457-460, 2003.
- [2] S. Wang and L. Jiang, "Definition of superhydrophobic states," *Advanced Materials*, vol. 19, pp. 3423-3424, 2007.
- [3] L. Gao and T. J. McCarthy, "Contact angle hysteresis explained," *Langmuir*, vol. 22, pp. 6234-6237, 2006.
- [4] M. Miwa, A. Nakajima, A. Fujishima, K. Hashimoto, and T. Watanabe, "Effects of the surface roughness on sliding angles of water droplets on superhydrophobic surfaces," *Langmuir*, vol. 16, pp. 5754-5760, 2000.
- [5] W. Barthlott and C. Neinhuis, "Purity of the sacred lotus, or escape from contamination in biological surfaces," *Planta*, vol. 202, pp. 1-8, 1997.
- [6] H. Zhou, H. Wang, H. Niu, A. Gestos, X. Wang, and T. Lin, "Fluoroalkyl silane modified silicone rubber/nanoparticle composite: A super durable, robust superhydrophobic fabric coating," *Advanced Materials*, vol. 24, pp. 2409-2412, 2012.
- [7] M. Yu, G. Gu, W.-D. Meng, and F.-L. Qing, "Superhydrophobic cotton fabric coating based on a complex layer of silica nanoparticles and perfluorooctylated quaternary ammonium silane coupling agent," *Applied Surface Science*, vol. 253, pp. 3669-3673, 2007.
- [8] L. Cao, A. K. Jones, V. K. Sikka, J. Wu, and D. Gao, "Anti-icing superhydrophobic coatings," *Langmuir*, vol. 25, pp. 12444-12448, 2009.
- [9] C. Antonini, M. Innocenti, T. Horn, M. Marengo, and A. Amirfazli, "Understanding the effect of superhydrophobic coatings on energy reduction in anti-icing systems," *Cold Regions Science and Technology*, vol. 67, pp. 58-67, 2011.
- [10] J. Genzer and K. Efimenko, "Recent developments in superhydrophobic surfaces and their relevance to marine fouling: a review," *Biofouling*, vol. 22, pp. 339-360, 2006.
- [11] J. Chapman and F. Regan, "Nanofunctionalized superhydrophobic antifouling coatings for environmental sensor applications—advancing deployment with answers from nature," *Advanced Engineering Materials*, vol. 14, pp. B175-B184, 2012.
- [12] G. Zorpette, "The do-it-all display [2013 Tech to watch]," *Spectrum, IEEE*, vol. 50, pp. 40-66, 2013.
- [13] L. Shu. *Amazon buys Samsung's Liguavista display subsidiary, hints of possible new Kindle tech*. Available: <http://www.digitaltrends.com/mobile/amazon-acquires-liquivista-from-samsung/#ixzz3WXZmaB4J>
- [14] D. Öner and T. J. McCarthy, "Ultrahydrophobic surfaces. Effects of topography length scales on wettability," *Langmuir*, vol. 16, pp. 7777-7782, 2000.
- [15] Z. Burton and B. Bhushan, "Hydrophobicity, adhesion, and friction properties of nanopatterned polymers and scale dependence for micro- and nanoelectromechanical systems," *Nano Letters*, vol. 5, pp. 1607-1613, 2005.
- [16] J.-Y. Shiu, C.-W. Kuo, P. Chen, and C.-Y. Mou, "Fabrication of tunable superhydrophobic surfaces by nanosphere lithography," *Chemistry of Materials*, vol. 16, pp. 561-564, 2004.

- [17] K. K. S. Lau, J. Bico, K. B. K. Teo, M. Chhowalla, G. A. J. Amaratunga, W. I. Milne, *et al.*, "Superhydrophobic carbon nanotube forests," *Nano Letters*, vol. 3, pp. 1701-1705, 2003.
- [18] L. Zhu, Y. Xiu, J. Xu, P. A. Tamirisa, D. W. Hess, and C.-P. Wong, "Superhydrophobicity on two-tier rough surfaces fabricated by controlled growth of aligned carbon nanotube arrays coated with fluorocarbon," *Langmuir*, vol. 21, pp. 11208-11212, 2005.
- [19] L. Feng, S. Li, H. Li, J. Zhai, Y. Song, L. Jiang, *et al.*, "Super-hydrophobic surface of aligned polyacrylonitrile nanofibers," *Angewandte Chemie International Edition*, vol. 41, pp. 1221-1223, 2002.
- [20] N. J. Shirtcliffe, G. McHale, M. I. Newton, and C. C. Perry, "Intrinsically superhydrophobic organosilica sol-gel foams," *Langmuir*, vol. 19, pp. 5626-5631, 2003.
- [21] K. Tadanaga, J. Morinaga, A. Matsuda, and T. Minami, "Superhydrophobic-superhydrophilic micropatterning on flowerlike alumina coating film by the sol-gel method," *Chemistry of Materials*, vol. 12, pp. 590-592, 2000/03/01 2000.
- [22] K. Tadanaga, K. Kitamuro, A. Matsuda, and T. Minami, "Formation of superhydrophobic alumina coating films with high transparency on polymer substrates by the sol-gel method," *Journal of Sol-Gel Science and Technology*, vol. 26, pp. 705-708, 2003/01/01 2003.
- [23] H. Liu, L. Feng, J. Zhai, L. Jiang, and D. Zhu, "Reversible wettability of a chemical vapor deposition prepared ZnO film between superhydrophobicity and superhydrophilicity," *Langmuir*, vol. 20, pp. 5659-5661, 2004.
- [24] J. C. Love, B. D. Gates, D. B. Wolfe, K. E. Paul, and G. M. Whitesides, "Fabrication and wetting properties of metallic half-shells with submicron diameters," *Nano Letters*, vol. 2, pp. 891-894, 2002.
- [25] A. Nakajima, K. Hashimoto, T. Watanabe, K. Takai, G. Yamauchi, and A. Fujishima, "Transparent superhydrophobic thin films with self-cleaning properties," *Langmuir*, vol. 16, pp. 7044-7047, 2000.
- [26] T. N. Krupenkin, J. A. Taylor, T. M. Schneider, and S. Yang, "From rolling ball to complete wetting: The dynamic tuning of liquids on nanostructured surfaces," *Langmuir*, vol. 20, pp. 3824-3827, 2004.
- [27] M. Jin, X. Feng, L. Feng, T. Sun, J. Zhai, T. Li, *et al.*, "Superhydrophobic aligned polystyrene nanotube films with high adhesive force," *Advanced Materials*, vol. 17, pp. 1977-1981, 2005.
- [28] S. Wang, L. Feng, and L. Jiang, "One-step solution-immersion process for the fabrication of stable bionic superhydrophobic surfaces," *Advanced Materials*, vol. 18, pp. 767-770, 2006.
- [29] M. Li, J. Zhai, H. Liu, Y. Song, L. Jiang, and D. Zhu, "Electrochemical deposition of conductive superhydrophobic zinc oxide thin films," *The Journal of Physical Chemistry B*, vol. 107, pp. 9954-9957, 2003.
- [30] S. Shibuichi, T. Yamamoto, T. Onda, and K. Tsujii, "Super water- and oil-repellent surfaces resulting from fractal structure," *Journal of Colloid and Interface Science*, vol. 208, pp. 287-294, 1998.
- [31] A. Nakajima, A. Fujishima, K. Hashimoto, and T. Watanabe, "Preparation of transparent superhydrophobic boehmite and silica films by sublimation of aluminum acetylacetonate," *Advanced Materials*, vol. 11, pp. 1365-1368, 1999.

- [32] N. Michael and B. Bhushan, "Hierarchical roughness makes superhydrophobic states stable," *Microelectronic Engineering*, vol. 84, pp. 382-386, 2007.
- [33] M. Nosonovsky and B. Bhushan, "Hierarchical roughness optimization for biomimetic superhydrophobic surfaces," *Ultramicroscopy*, vol. 107, pp. 969-979, 2007.
- [34] Y. Xiu, L. Zhu, D. W. Hess, and C. P. Wong, "Hierarchical silicon etched structures for controlled hydrophobicity/superhydrophobicity," *Nano Letters*, vol. 7, pp. 3388-3393, 2007.
- [35] Y. Kwon, N. Patankar, J. Choi, and J. Lee, "Design of surface hierarchy for extreme hydrophobicity," *Langmuir*, vol. 25, pp. 6129-6136, 2009.
- [36] T. H. Her, R. J. Finlay, C. Wu, and E. Mazur, "Femtosecond laser-induced formation of spikes on silicon," *Applied Physics A: Materials Science & Processing*, vol. 70, pp. 383-385, 2000.
- [37] B. K. Nayak, M. C. Gupta, and K. W. Kolasinski, "Spontaneous formation of nanospiked microstructures in germanium by femtosecond laser irradiation," *Nanotechnology*, vol. 18, p. 195302, 2007.
- [38] B. K. Nayak, M. C. Gupta, and K. W. Kolasinski, "Formation of nano-textured conical microstructures in titanium metal surface by femtosecond laser irradiation," *Applied Physics A: Materials Science & Processing*, vol. 90, pp. 399-402, 2008.
- [39] B. K. Nayak and M. C. Gupta, "Self-organized micro/nano structures in metal surfaces by ultrafast laser irradiation," *Optics and Lasers in Engineering*, vol. 48, pp. 940-949, 2010.
- [40] K. K. C. Lee, P. R. Herman, T. Shoa, M. Haque, J. D. W. Madden, and V. X. D. Yang, "Microstructuring of polypyrrole by maskless direct femtosecond laser ablation," *Advanced Materials*, vol. 24, pp. 1243-1246, 2012.
- [41] T. Baldacchini, J. E. Carey, M. Zhou, and E. Mazur, "Superhydrophobic surfaces prepared by microstructuring of silicon using a femtosecond laser," *Langmuir*, vol. 22, pp. 4917-4919, 2006.
- [42] T. O. Yoon, H. J. Shin, S. C. Jeoung, and Y.-I. Park, "Formation of superhydrophobic poly(dimethylsiloxane) by ultrafast laser-induced surface modification," *Opt. Express*, vol. 16, pp. 12715-12725, 2008.
- [43] C. Dong, Y. Gu, M. Zhong, L. Li, K. Sezer, M. Ma, *et al.*, "Fabrication of superhydrophobic Cu surfaces with tunable regular micro and random nano-scale structures by hybrid laser texture and chemical etching," *Journal of Materials Processing Technology*, vol. 211, pp. 1234-1240, 2011.
- [44] B. K. Nayak, P. O. Caffrey, C. R. Speck, and M. C. Gupta, "Superhydrophobic surfaces by replication of micro/nano-structures fabricated by ultrafast-laser-microtexturing," *Applied Surface Science*, vol. 266, pp. 27-32, 2013.
- [45] Solar Energy Facts: 2013 Year in review. U.S. PV market installed 4,751 MW; Largest year on record. Available:
<http://www.seia.org/sites/default/files/YIR%202013%20SMI%20Fact%20Sheet.pdf>
- [46] P. Campbell and M. A. Green, "Light trapping properties of pyramidally textured surfaces," *Journal of Applied Physics*, vol. 62, pp. 243-249, 1987.
- [47] J. M. Gee, W. K. Schubert, H. L. Tardy, T. D. Hund, and G. Robison, "The effect of encapsulation on the reflectance of photovoltaic modules using textured multicrystalline-silicon solar cells," in *Photovoltaic Energy Conversion, 1994., Conference Record of the Twenty Fourth. IEEE Photovoltaic Specialists Conference - 1994, 1994 IEEE First World Conference on*, 1994, pp. 1555-1558 vol.2.

- [48] D. H. Macdonald, A. Cuevas, M. J. Kerr, C. Samundsett, D. Ruby, S. Winderbaum, *et al.*, "Texturing industrial multicrystalline silicon solar cells," *Solar Energy*, vol. 76, pp. 277-283, 2004.
- [49] J. Zhao, A. Wang, P. Campbell, and M. A. Green, "22.7% efficient silicon photovoltaic modules with textured front surface," *Electron Devices, IEEE Transactions on*, vol. 46, pp. 1495-1497, 1999.
- [50] V. V. Iyengar, B. K. Nayak, and M. C. Gupta, "Optical properties of silicon light trapping structures for photovoltaics," *Solar Energy Materials and Solar Cells*, vol. 94, pp. 2251-2257, 2010.
- [51] J. Yoo, G. Yu, and J. Yi, "Black surface structures for crystalline silicon solar cells," *Materials Science and Engineering: B*, vol. 159–160, pp. 333-337, 2009.
- [52] Y. Xia, J. A. Rogers, K. E. Paul, and G. M. Whitesides, "Unconventional methods for fabricating and patterning nanostructures," *Chemical Reviews*, vol. 99, pp. 1823-1848, 1999.
- [53] P. N. Vinod and M. Lal, "Surface and optical characterization of the porous silicon textured surface," *Journal of Materials Science: Materials in Electronics*, vol. 16, pp. 1-6, 2005.
- [54] P. Papet, O. Nichiporuk, A. Kaminski, Y. Rozier, J. Kraiem, J. F. Lelievre, *et al.*, "Pyramidal texturing of silicon solar cell with TMAH chemical anisotropic etching," *Solar Energy Materials and Solar Cells*, vol. 90, pp. 2319-2328, 2006.
- [55] W. Sparber, O. Schultz, D. Biro, G. Emanuel, R. Preu, A. Poddey, *et al.*, "Comparison of texturing methods for monocrystalline silicon solar cells using KOH and Na/sub 2/CO/sub 3," in *Photovoltaic Energy Conversion, 2003. Proceedings of 3rd World Conference on*, 2003, pp. 1372-1375 Vol.2.
- [56] M. Tucci, R. De Rosa, and F. Roca, "CF₄/O₂ dry etching of textured crystalline silicon surface in a-Si:H/c-Si heterojunction for photovoltaic applications," *Solar Energy Materials and Solar Cells*, vol. 69, pp. 175-185, 2001.
- [57] J. Y. Chen, W. L. Chang, C. K. Huang, and K. W. Sun, "Biomimetic nanostructured antireflection coating and its application on crystalline silicon solar cells," *Opt. Express*, vol. 19, pp. 14411-14419, 2011.
- [58] M. Nam, J. Lee, and K.-K. Lee, "Efficiency improvement of solar cells by importing microdome-shaped anti-reflective structures as a surface protection layer," *Microelectronic Engineering*, vol. 88, pp. 2314-2318, 2011.
- [59] J. Escarré, K. Söderström, C. Battaglia, F.-J. Haug, and C. Ballif, "High fidelity transfer of nanometric random textures by UV embossing for thin film solar cells applications," *Solar Energy Materials and Solar Cells*, vol. 95, pp. 881-886, 2011.
- [60] N. Yamada, O. N. Kim, T. Tokimitsu, Y. Nakai, and H. Masuda, "Optimization of anti-reflection moth-eye structures for use in crystalline silicon solar cells," *Progress in Photovoltaics: Research and Applications*, vol. 19, pp. 134-140, 2011.
- [61] T.-F. Yao, P.-H. Wu, T.-M. Wu, C.-W. Cheng, and S.-Y. Yang, "Fabrication of anti-reflective structures using hot embossing with a stainless steel template irradiated by femtosecond laser," *Microelectronic Engineering*, vol. 88, pp. 2908-2912, 2011.
- [62] B. K. Nayak, M. C. Gupta, and K. W. Kolasinski, "Ultrafast-laser-assisted chemical restructuring of silicon and germanium surfaces," *Applied Surface Science*, vol. 253, pp. 6580-6583, 2007.

- [63] D. M. Bigg, "The effect of compounding on the conductive properties of EMI shielding compounds," *Advances in Polymer Technology*, vol. 4, pp. 255-266, 1984.
- [64] *FCC Title 47 - Telecommunication (Part 15-2009)*. Available: <http://www.gpo.gov/fdsys/pkg/CFR-2009-title47-vol1/pdf/CFR-2009-title47-vol1-part15.pdf>
- [65] J. T. Hoback and J. J. Reilly, "Conductive coatings for EMI shielding," *Journal of Elastomers and Plastics*, vol. 20, pp. 54-69, January 1, 1988 1988.
- [66] J. Huang, "EMI shielding plastics: a review," *Advances in Polymer Technology*, vol. 14, pp. 137-150, 1995.
- [67] Y. Yang, M. C. Gupta, K. L. Dudley, and R. W. Lawrence, "Conductive carbon nanofiber-polymer foam structures," *Advanced Materials*, vol. 17, pp. 1999-2003, 2005.
- [68] Y. Yang, M. C. Gupta, K. L. Dudley, and R. W. Lawrence, "The fabrication and electrical properties of carbon nanofibre-polystyrene composites," *Nanotechnology*, vol. 15, pp. 1545 -1548, 2004.
- [69] Y. Yang, M. C. Gupta, K. L. Dudley, and R. W. Lawrence, "Novel carbon nanotube-polystyrene foam composites for electromagnetic interference shielding," *Nano Letters*, vol. 5, pp. 2131-2134, 2005.
- [70] D. Qian, E. C. Dickey, R. Andrews, and T. Rantell, "Load transfer and deformation mechanisms in carbon nanotube-polystyrene composites," *Applied Physics Letters*, vol. 76, pp. 2868-2870, 2000.
- [71] C.-F. Wang, W.-Y. Chen, H.-Z. Cheng, and S.-L. Fu, "Pressure-proof superhydrophobic films from flexible carbon nanotube/polymer coatings," *The Journal of Physical Chemistry C*, vol. 114, pp. 15607-15611, 2010.
- [72] C.-F. Wang and S.-J. Lin, "Robust superhydrophobic/superoleophilic sponge for effective continuous absorption and expulsion of oil pollutants from water," *ACS Applied Materials & Interfaces*, vol. 5, pp. 8861-8864, 2013.
- [73] S. S. Madaeni, S. Zinadini, and V. Vatanpour, "Preparation of superhydrophobic nanofiltration membrane by embedding multiwalled carbon nanotube and polydimethylsiloxane in pores of microfiltration membrane," *Separation and Purification Technology*, vol. 111, pp. 98-107, 2013.
- [74] L. Zhao, W. L. Liu, L. D. Zhang, J. S. Yao, W. H. Xu, X. Q. Wang, *et al.*, "Fabrication of superhydrophobic and conductive surface based on carbon nanotubes," *Colloids and Surfaces A: Physicochemical and Engineering Aspects*, vol. 423, pp. 69-76, 2013.
- [75] S. Talaemashhadi, M. Sansotera, C. Gambarotti, A. Famulari, C. L. Bianchi, P. Antonio Guarda, *et al.*, "Functionalization of multi-walled carbon nanotubes with perfluoropolyether peroxide to produce superhydrophobic properties," *Carbon*, vol. 59, pp. 150-159, 2013.
- [76] I. S. Bayer, A. Steele, and E. Loth, "Superhydrophobic and electroconductive carbon nanotube-fluorinated acrylic copolymer nanocomposites from emulsions," *Chemical Engineering Journal*, vol. 221, pp. 522-530, 2013.
- [77] H. Yao, C.-C. Chu, H.-J. Sue, and R. Nishimura, "Electrically conductive superhydrophobic octadecylamine-functionalized multiwall carbon nanotube films," *Carbon*, vol. 53, pp. 366-373, 2013.
- [78] S.-H. Park, E.-H. Cho, J. Sohn, P. Theilmann, K. Chu, S. Lee, *et al.*, "Design of multi-functional dual hole patterned carbon nanotube composites with superhydrophobicity and durability," *Nano Research*, vol. 6, pp. 389-398, 2013.

- [79] J. A. Becker, C. B. Green, and G. L. Pearson, "Properties and uses of thermistors--- thermally sensitive resistors," *American Institute of Electrical Engineers, Transactions of the*, vol. 65, pp. 711-725, 1946.
- [80] Y. Luo and X. Liu, "High temperature NTC BaTiO₃-based ceramic resistors," *Materials Letters*, vol. 59, pp. 3881-3884, 2005.
- [81] Z. Han, B. Tay, C. Tan, M. Shakerzadeh, and K. Ostrikov, "Electrowetting control of cassie-to-wenzel transitions in superhydrophobic carbon nanotube-based nanocomposites," *ACS Nano*, vol. 3, pp. 3031-3036, 2009.
- [82] G. Londe, A. Chunder, L. Zhai, and H. J. Cho, "An analytical model for the wettability switching characteristic of a nanostructured thermoresponsive surface," *Applied Physics Letters*, vol. 94, pp. -, 2009.
- [83] E. Bormashenko, R. Pogreb, G. Whyman, Y. Bormashenko, and M. Erlich, "Vibration-induced Cassie-Wenzel wetting transition on rough surfaces," *Applied Physics Letters*, vol. 90, pp. -, 2007.
- [84] Z. Wang, C. Lopez, A. Hirsra, and N. Koratkar, "Impact dynamics and rebound of water droplets on superhydrophobic carbon nanotube arrays," *Applied Physics Letters*, vol. 91, pp. -, 2007.
- [85] R. I. Revilla, L. Guan, X.-Y. Zhu, B.-G. Quan, Y.-L. Yang, and C. Wang, "Electrowetting phenomenon on nanostructured surfaces studied by using atomic force microscopy," *The Journal of Physical Chemistry C*, vol. 116, pp. 14311-14317, 2012.
- [86] M. W. Lee, S. S. Latthe, A. L. Yarin, and S. S. Yoon, "Dynamic electrowetting-on-dielectric (DEWOD) on unstretched and stretched teflon," *Langmuir*, vol. 29, pp. 7758-7767, 2013.
- [87] G. Beni, S. Hackwood, and J. L. Jackel, "Continuous electrowetting effect," *Applied Physics Letters*, vol. 40, pp. 912-914, 1982.
- [88] G. Beni and S. Hackwood, "Electro-wetting displays," *Applied Physics Letters*, vol. 38, pp. 207-209, 1981.
- [89] B. Berge and J. Peseux, "Variable focal lens controlled by an external voltage: An application of electrowetting," *The European Physical Journal E*, vol. 3, pp. 159-163, 2000.
- [90] F. Lapierre, V. Thomy, Y. Coffinier, R. Blossey, and R. Boukherroub, "Reversible electrowetting on superhydrophobic double-nanotextured surfaces," *Langmuir*, vol. 25, pp. 6551-6558, 2009.
- [91] E. Seyrat and R. A. Hayes, "Amorphous fluoropolymers as insulators for reversible low-voltage electrowetting," *Journal of Applied Physics*, vol. 90, pp. 1383-1386, 2001.
- [92] N. Verplanck, E. Galopin, J.-C. Camart, V. Thomy, Y. Coffinier, and R. Boukherroub, "Reversible electrowetting on superhydrophobic silicon nanowires," *Nano Letters*, vol. 7, pp. 813-817, 2007.
- [93] M. S. Dhindsa, N. R. Smith, J. Heikenfeld, P. D. Rack, J. D. Fowlkes, M. J. Doktycz, *et al.*, "Reversible electrowetting of vertically aligned superhydrophobic carbon nanofibers," *Langmuir*, vol. 22, pp. 9030-9034, 2006.
- [94] B. P. Cahill, A. T. Giannitsis, R. Land, G. Gastrock, U. Pliquet, D. Frense, *et al.*, "Reversible electrowetting on silanized silicon nitride," *Sensors and Actuators B: Chemical*, vol. 144, pp. 380-386, 2010.
- [95] E. Siegenthaler, P. Wurtz, and R. Groner, "Improving the usability of e-book readers," *J. Usability Studies*, vol. 6, pp. 25-38, 2010.

- [96] M. Katayama, "TFT-LCD technology," *Thin Solid Films*, vol. 341, pp. 140-147, 1999.
- [97] B. Comiskey, J. D. Albert, H. Yoshizawa, and J. Jacobson, "An electrophoretic ink for all-printed reflective electronic displays," *Nature*, vol. 394, pp. 253-255, 07/16/print 1998.
- [98] J. F. R. Hayes. *Electrowetting displays*. Available: <http://www.liquavista.com/media/772/LQV0905291LL5-15.pdf>
- [99] R. A. Hayes and B. J. Feenstra, "Video-speed electronic paper based on electrowetting," *Nature*, vol. 425, pp. 383-385, 2003.
- [100] L. Zhu, J. Xu, Y. Xiu, Y. Sun, D. W. Hess, and C.-P. Wong, "Electrowetting of aligned carbon nanotube films," *The Journal of Physical Chemistry B*, vol. 110, pp. 15945-15950, 2006.
- [101] C. Quilliet and B. Berge, "Electrowetting: a recent outbreak," *Current Opinion in Colloid & Interface Science*, vol. 6, pp. 34-39, 2001.
- [102] G. Lippmann, "Relations entre les phénomènes électriques et capillaires," Gauthier-Villars, 1875.
- [103] F. Mugele and J.-C. Baret, "Electrowetting: from basics to applications," *Journal of Physics: Condensed Matter*, vol. 17, p. R705, 2005.
- [104] P. O. Caffrey, B. K. Nayak, and M. C. Gupta, "Ultrafast laser-induced microstructure/nanostructure replication and optical properties," *Appl. Opt.*, vol. 51, pp. 604-609, 2012.
- [105] S. D. Bhagat and M. C. Gupta, "Superhydrophobic microtextured polycarbonate surfaces," *Surface and Coatings Technology*, vol. 270, pp. 117-122, 2015.
- [106] P. O. Caffrey and M. C. Gupta, "Electrically conducting superhydrophobic microtextured carbon nanotube nanocomposite," *Applied Surface Science*, vol. 314, pp. 40-45, 2014.
- [107] C. Wang, T. Fuller, W. Zhang, and K. J. Wynne, "Thickness dependence of ice removal stress for a polydimethylsiloxane nanocomposite: Sylgard 184," *Langmuir*, vol. 30, pp. 12819-12826, 2014.
- [108] Y. H. Yeong, E. Loth, J. Sokhey, and A. Lambourne, "Ice adhesion performance of superhydrophobic coatings in aerospace icing conditions," SAE Technical Paper 0148-7191, 2015.
- [109] *Aircraft Owners and Pilots Association*. Available: <http://www.aopa.org/asf/publications/sa11.pdf>
- [110] *Airliners.net - De-Icing B747*. Available: http://www.airliners.net/aviation-forums/tech_ops/read.main/270990/
- [111] Wind power in the United States. [Online]. Available: http://en.wikipedia.org/wiki/Wind_power_in_the_United_States
- [112] R. Wiser and M. Bolinger. Annual report on U.S. wind power installation, cost, and performance trends: 2007. Available: <http://www.nrel.gov/docs/fy08osti/43025.pdf>
- [113] NACE. Cost of corrosion study. Available: <http://www.nace.org/Publications/Cost-of-Corrosion-Study/>
- [114] E. Herzberg. Impact of corrosion on cost and availability to DoD. *DoD Maintenance Symposium*. Available: http://www.sae.org/events/dod/presentations/2012/impact_of_corrosion_on_cost_and_availability_to_dod.pdf
- [115] Global Corrosion Inhibitors – Water & Oil Based, Organic & Inorganic Type, Applications, Raw Materials Trends & Forecasts (2010 – 2015). *Markets and Markets*.

Available:

http://www.researchandmarkets.com/reports/1574191/global_corrosion_inhibitors_water_and_oil

- [116] J. Lee, H. Moon, J. Fowler, T. Schoellhammer, and C.-J. Kim, "Electrowetting and electrowetting-on-dielectric for microscale liquid handling," *Sensors and Actuators A: Physical*, vol. 95, pp. 259-268, 2002.
- [117] S. J. Martin, K. O. Wessendorf, C. T. Gebert, G. C. Frye, R. W. Cernosek, L. Casaus, *et al.*, "Measuring liquid properties with smooth and textured surface resonators," in *Frequency Control Symposium, 1993. 47th., Proceedings of the 1993 IEEE International*, 1993, pp. 603-608.
- [118] T. Young, "An essay on the cohesion of fluids," *Philosophical Transactions of the Royal Society of London*, vol. 95, pp. 65-87, 1805.
- [119] H. Kamusewitz, W. Possart, and D. Paul, "The relation between Young's equilibrium contact angle and the hysteresis on rough paraffin wax surfaces," *Colloids and Surfaces A: Physicochemical and Engineering Aspects*, vol. 156, pp. 271-279, 1999.
- [120] A. E. Ismail, G. S. Grest, D. R. Heine, M. J. Stevens, and M. Tsige, "Interfacial structure and dynamics of siloxane systems: PDMS-vapor and PDMS-water," *Macromolecules*, vol. 42, pp. 3186-3194, 2009.
- [121] R. N. Wenzel, "Resistance of solid surfaces to wetting by water," *Industrial & Engineering Chemistry*, vol. 28, pp. 988-994, 1936.
- [122] L. Feng, S. Li, Y. Li, H. Li, L. Zhang, J. Zhai, *et al.*, "Super-hydrophobic surfaces: From natural to artificial," *Advanced Materials*, vol. 14, pp. 1857-1860, 2002.
- [123] N. Jarvis and W. Zisman, "Surface chemistry of fluorochemicals," DTIC Document 1965.
- [124] A. Nakajima, K. Hashimoto, and T. Watanabe, "Recent studies on super-hydrophobic films," *Monatshfte für Chemie / Chemical Monthly*, vol. 132, pp. 31-41, 2001.
- [125] C. Neinhuis and W. Barthlott, "Characterization and distribution of water-repellent, self-cleaning plant surfaces," *Annals of Botany*, vol. 79, pp. 667-677, 1997.
- [126] H. Tavana, A. Amirfazli, and A. W. Neumann, "Fabrication of superhydrophobic surfaces of n-hexatriacontane," *Langmuir*, vol. 22, pp. 5556-5559, 2006.
- [127] W. Rasband. *ImageJ* [ONLINE]. Available: <http://rsb.info.nih.gov/ij/>
- [128] A. F. Stalder, G. Kulik, D. Sage, L. Barbieri, and P. Hoffmann, "A snake-based approach to accurate determination of both contact points and contact angles," *Colloids and Surfaces A: Physicochemical and Engineering Aspects*, vol. 286, pp. 92-103, 2006.
- [129] "ASTM Standard D7334, 2008, "Standard practice for surface wettability of coatings, substrates and pigments by advancing contact angle measurement," ASTM International, West Conshohocken, PA, 2008," ed.
- [130] J. Groten and J. Rühle, "Surfaces with combined microscale and nanoscale structures: A route to mechanically stable superhydrophobic surfaces?," *Langmuir*, 2013.
- [131] G. McHale, N. J. Shirtcliffe, and M. I. Newton, "Contact-angle hysteresis on superhydrophobic surfaces," *Langmuir*, vol. 20, pp. 10146-10149, 2004.
- [132] E. Pierce, F. J. Carmona, and A. Amirfazli, "Understanding of sliding and contact angle results in tilted plate experiments," *Colloids and Surfaces A: Physicochemical and Engineering Aspects*, vol. 323, pp. 73-82, 2008.
- [133] J. Heikenfeld and M. Dhindsa, "Electrowetting on superhydrophobic surfaces: present status and prospects," *Journal of Adhesion Science and Technology*, vol. 22, pp. 319-334, 2008.

- [134] A. B. D. Cassie and S. Baxter, "Wettability of porous surfaces," *Transactions of the Faraday Society*, vol. 40, pp. 546-551, 1944.
- [135] Dow Corning Sylgard® 184 Silicone Elastomer Available: <http://www4.dowcorning.com/DataFiles/090007c8803bb6a1.pdf>
- [136] L. Krogh and P. Asberg, "My little guide to soft lithography (or Soft lithography for dummies)," *Linköping University, website*, http://www.ifm.liu.se/~petas/mikrosystem/Links/Material_files/Soft_Lithography_for_Dummies.pdf, 2003.
- [137] J. C. McDonald and G. M. Whitesides, "Poly(dimethylsiloxane) as a material for fabricating microfluidic devices," *Accounts of Chemical Research*, vol. 35, pp. 491-499, 2002.
- [138] C. Liu, "Recent developments in polymer MEMS," *Advanced Materials*, vol. 19, pp. 3783-3790, 2007.
- [139] M. C. Gupta, L. Wang, C. Rothenbach, and K. Sun, "Diode Pumped Solid State Lasers for Surface Microtexture," *JOURNAL OF LASER MICRO NANOENGINEERING*, vol. 8, pp. 124-130, 2013.
- [140] L. Chao-Xuan and C. Jin-Woo, "Patterning conductive PDMS nanocomposite in an elastomer using microcontact printing," *Journal of Micromechanics and Microengineering*, vol. 19, p. 085019, 2009.
- [141] Keithley Model 6105 Resistivity Adapter Instruction Manual. Available: <http://www.keithley.com/data?asset=953>
- [142] "ASTM Standard D257, 2007, "Standard test methods for DC resistance or conductance of insulating materials," ASTM International, West Conshohocken, PA, 2007," ed.
- [143] S. Blank, "Why the lean startup changes everything," *Harvard Business Review*, 2013.
- [144] E. Ries, *The lean startup: How today's entrepreneurs use continuous innovation to create radically successful businesses*: Crown Publishing Group, 2011.
- [145] B. Sopori, J. Madjdpour, Y. Zhang, and W. Chen, "Optical modeling of a-si solar cells," *NREL*, 1999.
- [146] N. J. Shirtcliffe, G. McHale, S. Atherton, and M. I. Newton, "An introduction to superhydrophobicity," *Advances in Colloid and Interface Science*, vol. 161, pp. 124-138, 2010.
- [147] K.-Y. Yeh, L.-J. Chen, and J.-Y. Chang, "Contact angle hysteresis on regular pillar-like hydrophobic surfaces," *Langmuir*, vol. 24, pp. 245-251, 2007.
- [148] K. Krishnan, "Droplet-droplet, droplet-wall and microorganism-wall collisions," M.S. thesis, MAE, University of Virginia, Charlottesville, VA, 2013.
- [149] S. Lee and S. Lee, "Shrinkage ratio of PDMS and its alignment method for the wafer level process," *Microsystem Technologies*, vol. 14, pp. 205-208, 2008.
- [150] Y. Y. Wang, G. Y. Tang, F. A. M. Koeck, B. Brown, J. M. Garguilo, and R. J. Nemanich, "Experimental studies of the formation process and morphologies of carbon nanotubes with bamboo mode structures," *Diamond and Related Materials*, vol. 13, pp. 1287-1291, 2004.
- [151] B. G. Sumpter, V. Meunier, J. M. Romo-Herrera, E. Cruz-Silva, D. A. Cullen, H. Terrones, *et al.*, "Nitrogen-mediated carbon nanotube growth: diameter reduction, metallicity, bundle dispersability, and bamboo-like structure formation," *ACS Nano*, vol. 1, pp. 369-375, 2007.
- [152] J. Engel, J. Chen, C. Nannan, S. Pandya, and L. Chang, "Multi-walled carbon nanotube filled conductive elastomers: materials and application to micro transducers," in *Micro*

- Electro Mechanical Systems, 2006. MEMS 2006 Istanbul. 19th IEEE International Conference on*, 2006, pp. 246-249.
- [153] W. J. J. Welters and L. G. J. Fokkink, "Fast electrically switchable capillary effects," *Langmuir*, vol. 14, pp. 1535-1538, 1998.
- [154] H. J. J. Verheijen and M. W. J. Prins, "Contact angles and wetting velocity measured electrically," *Review of Scientific Instruments*, vol. 70, pp. 3668-3673, 1999.
- [155] A. Torkkeli, *Droplet microfluidics on a planar surface*: VTT Technical Research Centre of Finland, 2003.
- [156] M. Sarshar, C. Swartz, S. Hunter, J. Simpson, and C.-H. Choi, "Effects of contact angle hysteresis on ice adhesion and growth on superhydrophobic surfaces under dynamic flow conditions," *Colloid and Polymer Science*, vol. 291, pp. 427-435, 2013.
- [157] Dow. *UCAR™ Endurance EG106 aircraft deicing/anti-icing fluid*. Available: http://www.dow.com/aircraft/products/type_four/e106.htm
- [158] S. Adam, K. N. Barada, D. Alexander, C. G. Mool, and L. Eric, "Linear abrasion of a titanium superhydrophobic surface prepared by ultrafast laser microtexturing," *Journal of Micromechanics and Microengineering*, vol. 23, p. 115012, 2013.
- [159] B. E. Saleh and M. Teich, "Fundamentals of photonics wiley series in pure and applied optics," NY, NY, 1991.
- [160] *Stanford Research Systems high voltage power supplies - PS300 Series — DC high voltage power supplies to 20 kV*. Available: <http://www.thinksrs.com/downloads/PDFs/Catalog/PS300c.pdf>
- [161] T. R. Kuphaldt. *Lessons in electric circuits, volume III – semiconductors*. Available: <http://www.allaboutcircuits.com/pdf/SEMI.pdf>
- [162] M. T. Bernius and A. Chutjian, "High-voltage, full-floating 10-MHz square-wave generator with phase control," *Review of Scientific Instruments*, vol. 60, pp. 779-782, 1989.
- [163] M. T. Bernius and A. Chutjian, "Improved high-voltage, high-frequency square-wave generator," *Review of Scientific Instruments*, vol. 61, pp. 925-927, 1990.
- [164] R. E. Continetti, D. R. Cyr, and D. M. Neumark, "Fast 8 kV metal-oxide semiconductor field-effect transistor switch," *Review of Scientific Instruments*, vol. 63, pp. 1840-1841, 1992.
- [165] R. J. Baker and B. P. Johnson, "Stacking power MOSFETs for use in high speed instrumentation," *Review of Scientific Instruments*, vol. 63, pp. 5799-5801, 1992.

Appendix 1 - MATLAB® program listings for models

Program 1.

This program is used to calculate and plot reflectance versus angles of incidence for silicon (or PDMS). Used to produce graphs of predictions for figure 4.2-3.

```
%
% Copied from Phys 531 Homework 4, Problem 2.
% Was Plot Reflectance vs. Angle of incidence for Nickel (at 560nm)
% POC 9/29/2004
%
% Refreshed for reflectance data for Figure 5 of Paper1
% POC 8/6/2011
%
n_i = 1.0;                % Index of Air
n_t = 3.874 + 0.015i;    % Index of Si
n_t = 3.882 + 0.019i;    %
%Index of Si
n_t = 1.412              % Index of PDMS
n_t = 3.874 + 0.015i;    % Index of Si
rtd = 360 / ( 2*pi );    % Conversion factor radians to degrees
%
% Allocate space for Theta vector
theta_i = linspace( 0, pi/2, 90 );

%
% Calculate theta_t
theta_t = asin( (n_i/n_t) * sin(theta_i) );

%
% Fresnel amplitude coefficients r_prp and r_par
r_prp = ((n_i*cos(theta_i) - n_t*cos(theta_t)) ./ (n_i*cos(theta_i) +
n_t*cos(theta_t)));
r_par = ((n_t*cos(theta_i) - n_i*cos(theta_t)) ./ (n_i*cos(theta_t) +
n_t*cos(theta_i)));

%
% Reflectances
R_prp = abs( r_prp ).^2;
R_par = abs( r_par ).^2;

%
% Plot the resulting graph
plot( theta_i.*rtd ,R_prp ); hold; text(42, 0.4, 'R_p_r_p');
plot( theta_i.*rtd ,R_par ); hold; text(80, 0.05, 'R_p_a_r'); hold;
xlabel( 'Angle of Incidence (degrees)' ); ylabel( 'Reflectance (R)' );
```

Program 2.

This program is used to generate the graph of figure 2.4-1 where the apparent contact angle is graphed against the effective contact angle for various settings for the Cassie-Baxter wetting factor (ϕ_s).

```
%
% Plot Contact Angle vs. Wenzel Roughness
% POC 5/18/2014
%
clear;

%
% This is the real Contact Angle ala young
%
Theta_c=linspace( 0, 180, 181 );

%
% Loop for each degree
% This could be done as a dot operation but I use a loop for simplicity
%
for i=1:181
    %
    % Compute cosine
    %
    Cos_Theta_c(i) = cosd( Theta_c(i) );

    for r=[1,5,10,15,20]
        %
        % Determine apparent CA for wenzel roughnesss for the various roughness
        %
        Cos_Theta_s_r(i,r) = r*Cos_Theta_c(i);
        Theta_s_r(i,r)=acosd(Cos_Theta_s_r(i,r));
    end
end;

%
% Plot output Graph
%
plot(Theta_c(60:120),Theta_s_r((60:120),1),'color','k');hold on;
plot(Theta_c(60:120),Theta_s_r((60:120),5),'color','b');
plot(Theta_c(60:120),Theta_s_r((60:120),10),'color','r');
plot(Theta_c(60:120),Theta_s_r((60:120),15),'color','g');
plot(Theta_c(60:120),Theta_s_r((60:120),20),'color','m');
axis([70 110 0 180]);
text(78,82,'r = 1');
text(82,55,'r = 5');
text(84.4,43,'r = 10');
text(85.1,20,'r = 15');
text(88,33,'r = 20');
text(95,40,'More Hydrophobic');
text(75,120,'More Hydrophilic');
text(88,33,'r = 20');
```

```
x=[90,90];y=[0,180];line('XData',x,'YData',y, 'LineStyle','--');
xlabel('Apparent Contact Angle (\Theta_c) (Degrees)');
ylabel('Observed Contact Angle(\theta_*) (Degrees) ');
%title('Wenzel Roughness (r), Cos\theta_*=rCos\theta_c');
hold off;

%
% Plot Contact Angle vs. Cassie-Baxter Factor
% POC 5/18/2015
%
clear;
```

Program 3.

This program is used to generate the graph of figure 2.4-2 where the apparent contact angle is graphed against the effective contact angle for various instances of Wenzel roughness (r). The area on the graph to the left of 90° shows the increase in hydrophilic behavior with increasing roughness whereas the area to the right shows the increase in hydrophobic behavior with increasing roughness.

```
%  
% This is the real Contact Angle ala young  
%  
Theta_c=linspace( 0, 180, 181 );  
phi_array=[0.1,0.2,0.3,0.4,0.5,0.6,0.7,0.8,0.9,1.0];  
  
%  
% Loop for each degree  
% This could be done as a dot operation but I use a loop for simplicity  
%  
for i=1:181  
    %  
    % Compute cosine  
    %  
    Cos_Theta_c(i) = cosd( Theta_c(i) );  
  
    for j=1:10  
        %  
        % Determine apparent CA for various Cassie-Baxter factor values  
        %  
        phi_s=phi_array(j);  
        Cos_Theta_s_phi(i,j) = -1 + phi_s*(1+Cos_Theta_c(i));  
        Theta_s_phi(i,j)=acosd(Cos_Theta_s_phi(i,j));  
    end  
  
end;  
  
%  
% Plot output Graph  
%  
plot(Theta_c(1:180),Theta_s_phi((1:180),1),'color','k');hold on;  
plot(Theta_c(1:180),Theta_s_phi((1:180),2),'color','y');  
plot(Theta_c(1:180),Theta_s_phi((1:180),4),'color','b');  
plot(Theta_c(1:180),Theta_s_phi((1:180),6),'color','r');  
plot(Theta_c(1:180),Theta_s_phi((1:180),8),'color','g');  
plot(Theta_c(1:180),Theta_s_phi((1:180),10),'color','m');  
axis([0 180 0 180]);  
text(60,48,'\Phi_s = 1');  
text(20,50,'\Phi_s = .8');  
text(20,90,'\Phi_s = .6');  
text(20,110,'\Phi_s = .4');  
text(20,135,'\Phi_s = .2');  
text(20,152,'\Phi_s = .1');
```

```
xlabel('Apparent Contact Angle (\Theta_c) (Degrees)');  
ylabel('Observed Contact Angle(\theta_*) (Degrees)');  
%title('Cassie-Baxter Factor (\Phi_s)  
hold off;
```

Appendix 2 – C code program to control GPIB power supply

```
/*
 * Filename - Simple.c
 *
 * This application demonstrates how to read from and write to the
 * Tektronix PS2520G Programmable Power Supply.
 *
 * To build open the MS Visual C++ Command prompt and issue the following command
 * cl /I"%NIEXTCCOMPILERSUPP%\include" StepUp.c
"%NIEXTCCOMPILERSUPP%\lib32\msvc\ni4882.obj" /MD
 * or use the build.bat batch file to build
 *
 * This sample application is comprised of three basic parts:
 *
 * 1. Initialization
 * 2. Main Body
 * 3. Cleanup
 *
 * The Initialization portion consists of getting a handle to a
 * device and then clearing the device.
 *
 * In the Main Body, this application queries a device for its
 * identification code by issuing the '*IDN?' command. Many
 * instruments respond to this command with an identification string.
 * Note, 488.2 compliant devices are required to respond to this
 * command.
 *
 * The last step, Cleanup, takes the device offline.
 */

#include <stdio.h>
#include <stdlib.h>
#include <malloc.h>
#include <windows.h>

#include "ni4882.h"

#include <sys/types.h>
#include <sys/timeb.h>
#include <time.h>

#define ARRAY_SIZE          1024      // Size of read buffer

#define BDINDEX             0         // Board Index
#define PRIMARY_ADDR_OF_PPS 14       // Primary address of device
#define NO_SECONDARY_ADDR   0        // Secondary address of device
#define TIMEOUT             T10s     // Timeout value = 10 seconds
#define EOTMODE             1        // Enable the END message
#define EOSMODE             0        // Disable the EOS mode

int  Dev;
char ValueStr[ARRAY_SIZE + 1];
char ErrorMnemonic[29][5] = { "EDVR", "ECIC", "ENOL", "EADR", "EARG",
                             "ESAC", "EABO", "ENEB", "EDMA", "",
                             "EOIP", "ECAP", "EFSO", "", "EBUS",
                             "ESTB", "ESRQ", "", "", "",
                             "ETAB", "ELCK", "EARM", "EHDL", "",
                             "", "EWIP", "ERST", "EPWR" };

```

```

void GPIBCleanup(int Dev, const char * ErrorMessage);

int __cdecl main(void)
{
    /*
    * =====
    *
    * INITIALIZATION SECTION
    *
    * =====
    */

    //
    // Since this is C code make some local variables
    //
    int i;
    int j;
    char VoutCommand[20];

    //
    // For time keeping
    //
    struct _timeb timebuffer;
    char timeline[26];
    errno_t err;

    //
    // Make a few constants
    //
    const int MaxVoltage=2000;    // The Max Voltage
    const int DelayMS=0;         // Delay between each minor step

    //
    // The step delay is how long to wait at the modulo 100 voltage plateau
    // Since the video is 29 FPS, the best accuracy is +/- 35 ms for the video
    // The PC is using the Meinberg NTP client code which has been +/- 5 ms or less
    // So the total time accuracy is +/- 40 ms
    // ==> the delay at the plateau should be ~100 ms
    //
    const int StepDelayMS=100;    // The delay at each plateau
    const int Msize=200;         // The Steps between Measurements
    const int VoltageStep=5;     // The voltage step size

    /*
    * The application brings the power supply online using ibdev. A
    * device handle, Dev, is returned and is used in all subsequent
    * calls to the device.
    */
    Dev = ibdev(BDINDEX, PRIMARY_ADDR_OF_PPS, NO_SECONDARY_ADDR,
               TIMEOUT, EOTMODE, EOSMODE);
    if (Ibsta() & ERR)
    {
        printf("Unable to open device\nibsta = 0x%x iberr = %d\n",
              Ibsta(), Iberr());
        return 1;
    }

    /*
    * Clear the internal or device functions of the device. If the
    * error bit ERR is set in ibsta, call GPIBCleanup with an error
    * message.
    */
}

```

```

ibclr(Dev);
if (Ibsta() & ERR)
{
    GPIBCleanup(Dev, "Unable to clear device");
    return 1;
}

/*
 * =====
 *
 * MAIN BODY SECTION
 *
 * In this application, the Main Body communicates with the instrument
 * by writing a command to it and reading its response. This would be
 * the right place to put other instrument communication.
 *
 * =====
 */

/*
 * The application issues the '*IDN?' command to the power supply.
 */
ibwrt(Dev, "*IDN?\n", 6L);
if (Ibsta() & ERR)
{
    GPIBCleanup(Dev, "Unable to write to the Power Supply");
    return 1;
}

/*
 * The application reads the identification code in the form of an
 * ASCII string from the power supply into the ValueStr variable.
 */
ibrd(Dev, ValueStr, ARRAY_SIZE);
if (Ibsta() & ERR)
{
    GPIBCleanup(Dev, "Unable to read data from Power Supply");
    return 1;
}

/*
 * Assume that the returned string contains ASCII data. NULL
 * terminate the string using the value in ibcnt1 which is the
 * number of bytes read in. Use printf to display the string.
 */
ValueStr[Ibcnt() - 1] = '\0';

printf("Data read: %s\n", ValueStr);

//
// First set the supply off
//
ibwrt(Dev, "HVOF\n", 5L );

//
// Set the voltage to Zero
//
ibwrt(Dev, "VSET0\n", 6L );

//
// For this test we make a 100V amplitude square wave at 0.1 Hz
//

```

```

//
// Set the supply on
//
ibwrt(Dev, "HVON\n", 5L );

//
// Ramp the voltage up
//
for( i=0; i<=MaxVoltage ; i+=VoltageStep)
{
    //
    // Set the voltage
    //
    sprintf( VoutCommand, "VSET%03d\n", i);
    ibwrt(Dev, VoutCommand, 8L );

    //
    // Print out Timestamp every 100V
    //
    if(!(i%Msize))
    {
        _ftime( &timebuffer );
        err = ctime_s( timeline, 26, & ( timebuffer.time ) );
        printf( "%4dV at %.19s.%03d\n", i, timeline, timebuffer.millitm );
        Sleep( StepDelayMS );
    }
    Sleep( DelayMS );
}

//
// Now ramp the voltage back down
//
for( ; i>=0 ; i-=VoltageStep)
{
    //
    // Set the voltage
    //
    sprintf( VoutCommand, "VSET%03d\n", i);
    ibwrt(Dev, VoutCommand, 8L );

    //
    // Print out Timestamp every 100V
    //
    if(!(i%Msize))
    if(i!=MaxVoltage) // don't delay another StepDelayMS at the top
    {
        _ftime( &timebuffer );
        err = ctime_s( timeline, 26, & ( timebuffer.time ) );
        printf( "%4dV at %.19s.%03d\n", i, timeline, timebuffer.millitm );
        Sleep( StepDelayMS );
    }
    Sleep( DelayMS );
}

//
// Set the voltage to Zero
//
ibwrt(Dev, "VSET0\n", 6L );

//
// Set the supply off
//
ibwrt(Dev, "HVOF\n", 5L );

```

```

/*
 * =====
 *
 * CLEANUP SECTION
 *
 * =====
 */

/*
 * The device is taken offline.
 */
ibonl(Dev, 0);

return 0;
}

/*
 * After each GPIB call, the application checks whether the call
 * succeeded. If an NI-488.2 call fails, the GPIB driver sets the
 * corresponding bit in the global status variable. If the call
 * failed, this procedure prints an error message, takes the device
 * offline and exits.
 */
void GPIBCleanup(int Dev, const char * ErrorMessage)
{
    printf("Error : %s\nibsta = 0x%x iberr = %d (%s)\n",
          ErrorMessage, Ibsta(), Iberr(), ErrorMnemonic[Iberr()]);
    if (Dev != -1)
    {
        printf("Cleanup: Taking device off-line\n");
        ibonl(Dev, 0);
    }
}

```

Appendix 3 – Experimental details of future electrowetting fixture.

Initially we attempted to use an SCR device to switch the PS325 output similar to a chopper-type circuit. The intent was that we would strive to keep the current below the holding current threshold and thus would not need any snubber circuit to turn the SCR off. However it was found that the majority of commercial SCR packages (including our samples) include an internal resistance between the gate and the cathode that limited operation to relatively high current applications as shown in figure A3-1.

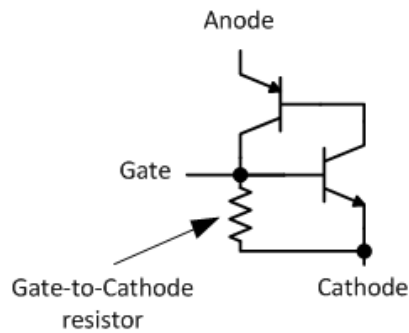


Figure A3-1. Equivalent SCR circuit showing Gate-to-Cathode resistor [161]

Given the lack of success with the use of an SCR device to modulate the PS325 high voltage output it was decided to research the use of high power MOSFETS for this application. Commercially available MOSFETS are typically available with a voltage rating of 500 V or less so in order to modulate or switch voltages as high as 1500 V multiple devices must be utilized. There is literature available in the area of high-frequency switching using MOSFETS [162, 163] and also using MOSFETS in a stacked configuration for high voltage [164, 165] and using these references the test fixture of figure 5.2-2 is proposed.

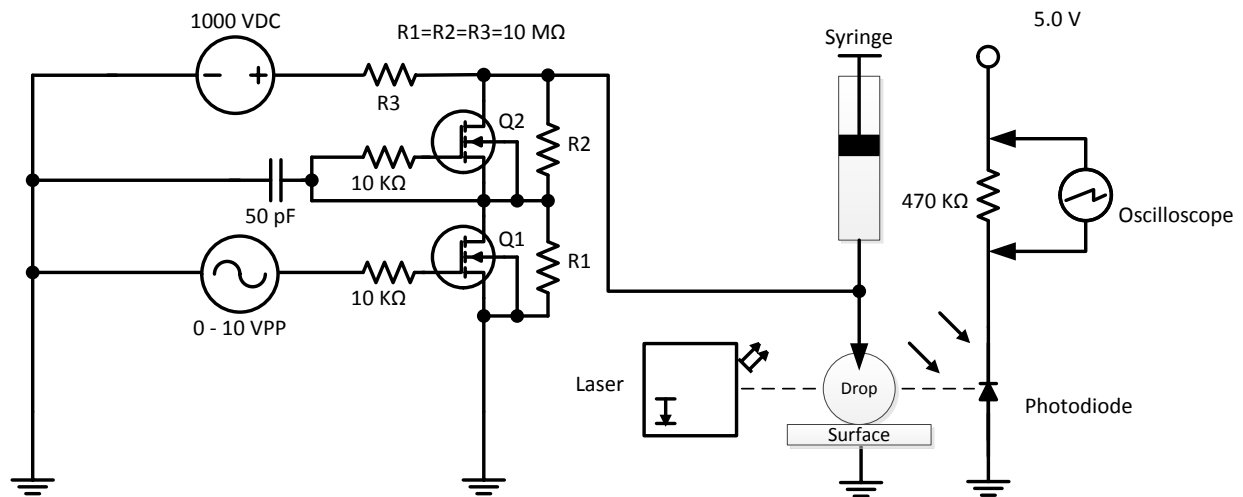


Figure A3-2. Test apparatus to generate variable frequency excitation for electrojetting testing of laser shutter application using stacked MOSFET circuit.

The values of the resistance are initial values only with the intent that the variability of the zero – 10 V output from the DS345 synthesized function generator would be utilized until final values are fixed. In addition the circuits of Baker [165] show additional capacitors and resistors for impedance matching that have been omitted due to the high impedance of our application and these may be added if necessary.

One future enhancement to the contact goniometer measurement system that would have broad impact would be the addition of an automated image recognition system that would automatically analyze a captured image and rather than using the drop image plugin for ImageJ that requires the user to “snake” the contour of the drop would automate this step, thus eliminating the human subjective analysis of the image contour boundaries from the error budget of the system. This would of course require extensive image processing techniques but would have application in any situation that utilizes the drop image plugin.

Appendix 4 – Published papers.

Ultrafast laser-induced microstructure/nanostructure replication and optical properties

Paul O. Caffrey, Barada K. Nayak, and Mool C. Gupta*

Charles L. Brown Department of Electrical and Computer Engineering, University of Virginia,
Charlottesville, Virginia 22904, USA

*Corresponding author: mgupta@virginia.edu

Received 22 August 2011; revised 6 November 2011; accepted 7 November 2011;
posted 7 November 2011 (Doc. ID 153248); published 7 February 2012

This paper demonstrates replication of ultrafast laser-induced micro/nano surface textures on poly(dimethylsiloxane) (PDMS). The surface texture replication process reduces the processing steps for microtexturing while improving light trapping. Two methods are demonstrated to replicate surface microtexture, a simple mold method and an embossing method. The laser microtextured silicon and titanium surfaces with micro to nanoscale features have been successfully replicated. Optical characterization of the replicated microtextured PDMS surfaces is performed and the results agree with model predictions. The replicated microtextured PDMS film is applied on a silicon surface and optical characterization shows that surface reflectance can be suppressed over 55% compared to the control value. © 2012 Optical Society of America

OCIS codes: 220.4000, 320.7090, 220.4241, 160.4760, 310.1210, 160.5470.

1. Introduction

There are many potential applications for surfaces with texture at the microscale or nanoscale. These applications include in the electronics industry, where surface microtexture can be applied to novel sensors and devices [1], the solar energy industry, where surface microtexture plays an important role in adding to the efficiency of the solar cell [2,3], and the medical industry, where microtextured surfaces play many important roles by providing hydrophobic and hydrophilic surfaces where cell growth can be controlled [4].

Lately, surface microtexture has become a subject of much interest due to the phenomenal growth in the photovoltaic solar industry and the drive for more efficient solar cells [5–8]. Surface microtexture has been demonstrated to increase the efficiency of the solar cell module [2]. The addition of an antireflective surface layer is typically deployed in addition to surface microtexture but even with these mea-

asures, reflection losses typically amount to 5%–10% [7,9,10]. Although there are other methods of inducing surface microtexture [10–12], surface microtexture is typically generated by use of a chemical isotropic or anisotropic etching process [13–15]. This processing step is not only costly and time consuming, but it is not very effective for polycrystalline and thin film silicon solar cells. Poly(dimethylsiloxane) (PDMS) molding techniques have recently been demonstrated for solar cell and antireflection coating fabrication using multistep processes to reproduce texture on a variety of polymers, such as PDMS and poly(methyl methacrylate) (PMMA) [16,17], and on UV lacquer [18].

Recently, work has been reported on producing antireflecting coatings by utilizing a nanoimprint replication technique to produce nanotextured “moth-eye” surfaces [19]. Recent work has demonstrated replicated detail at the nanoscale using a multistep nanoimprint lithography process using PMMA [20], and even more recently, periodic parallel line nanostructures on stainless steel has been replicated on polycarbonate film [21]. These methods are simpler than the more traditional chemical etching

1559-128X/12/050604-06\$15.00/0
© 2012 Optical Society of America

604 APPLIED OPTICS / Vol. 51, No. 5 / 10 February 2012

techniques. However, the method demonstrated in this paper shows a simpler single step process for microtexture replication.

New methods of producing microtextured surfaces using ultrafast laser radiation [22–24] have been successfully developed that can produce microtexture or nanotexture surfaces on metals and semiconductors. This work demonstrates the replication and use of these microtextures using methods that are simple and are readily applicable to industrial processes.

This surface microtexture replication demonstrates a novel approach that serves two purposes. Surface microtexture replication reduces the processing step for texturing while improving light trapping. The surface microtexture layer also serves as the required protective layer, thus eliminating additional processing steps.

We show details of the microtexture replication process, the optical properties of the replicated surfaces, and their application for reduction of reflection from silicon surfaces.

2. Experiment

For this work, PDMS was obtained from Ellsworth Adhesives (Dow Corning Sylgard 184 Silicone Encapsulant). This is a two-part polymer comprised of a base and a hardener that are mixed together at a 10:1 ratio. Care should be taken when dispensing the base to minimize the addition of air bubbles, as any bubbles will need to be eliminated by vacuum desiccation.

The titanium master is prepared as follows. The Ti sheet is diced into small square pieces of 1 cm² in size and thickness in the range of 0.2–0.5 mm. The metal piece is then placed on a stage inside a vacuum chamber mounted on a high-precision computer-controlled X–Y stage. The samples are exposed to ~1 mJ energy laser pulses of 800 nm wavelength and 130 fs pulse duration at a repetition rate of 1 KHz from a regeneratively amplified Spectra Physics Ti:sapphire laser system [22]. Similarly, the Si masters are made according to the procedure outlined by Nayak *et al.* [23].

The initial investigation into the surface replication capabilities of PDMS were performed by making a simple mold using a 30 mm nylon washer placed in a 50 mm Petri dish with the microtextured master placed as shown in Fig. 1(a).

The Petri dish is placed on a hot plate to cure for 1.5 h in air at 80 °C. After curing, the PDMS is removed from the Petri dish and the master is carefully separated from the PDMS. In our experiment, the initial PDMS samples were made 3–5 mm thick to facilitate handling. This allowed the master to be separated from the PDMS by bending the PDMS sample slowly, taking care not to induce cracking.

A method was developed to similarly replicate surface microtexture on a substrate using an embossing technique. Several important variables were determined.

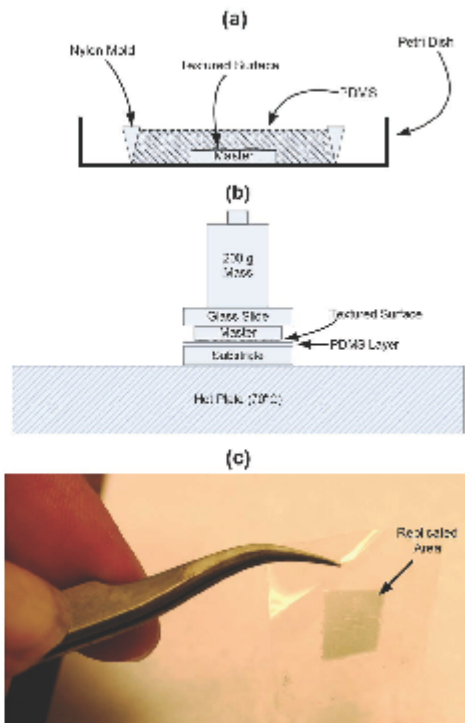


Fig. 1. (Color online) PDMS microsurface and nanosurface texture generation by (a) PDMS replication and (b) PDMS embossing, and (c) PDMS microtextured film produced from the embossing process.

1. The thickness of the initial PDMS coating, which is determined by the speed of the spin-coating process, 20 s at 1850 RPM gave a thickness of approximately 190 μm .
2. The overall cure temperature of 70 °C.
3. The duration of the delay to allow the thin film to spread prior to the initial cure of greater than 10 min.
4. The duration of the initial cure time prior to embossing, 3 min.
5. The amount of weight applied during the embossing process, 200 g.
6. The final cure time of greater than 15 min (at 70 °C).

The most critical of the above variables is item number 4, the initial cure time before the embossing. It was found that too much time resulted in little or no surface microtexture after embossing, whereas too little time resulted in a master firmly embedded in the PDMS layer, requiring careful and extensive cleanup.

The replication procedure [see Fig. 1(b)] involves spin coating approximately 190 μm of PDMS thin

film onto the substrate. This thin film must be allowed to spread from the spin-coating process to become of uniform thickness; the exact delay time is not critical, but should be greater than 10 min.

The substrate is then placed on the hot plate at 70 °C for 3 min. This pre-emboss cure prevents the PDMS from sticking to the master when the master is applied to the PDMS layer. After the pre-emboss cure, the master is placed on the substrate with the microtexture side face down on the PDMS layer. A glass slide was then placed over the master and a 200 g mass was placed on top to provide the embossing force. The complete stack, including the substrate, PDMS layer, master, glass slide, and the 200 g mass, are now left on the hot plate for the final cure time of at least 15 min at 70 °C, as shown in Fig. 1(b).

When the cure time is complete, the mass and glass slide are removed. The master is then carefully pried off the substrate using a very fine set of tweezers (Techni-Tool Type 2AB). It can be difficult to separate the master from the PDMS layer and care must be taken to avoid separation of the PDMS layer from the substrate. A priming agent, such as Dow Corning PR-1200, may be used to increase adhesion of the PDMS to the substrate.

Figure 1(c) shows an example of the results that can be obtained using the above procedure; this particular example shows a 190 μm film that has been embossed using a Ti master.

The optical properties of the PDMS microtextured surface are measured using an integrating sphere (Model RTC-060-SF from labSphere Inc.) with Spectralect coating. The experimental setup is shown in Fig. 2. Using this apparatus, the total integrated light scattering (TILS) power can be measured as shown in Fig. 2(a). The light scattering power can be further broken down into the reflected plus back-scattered power ($R + S_B$), as shown in Fig. 2(b), and the transmitted plus forward scattered power ($T + S_F$), as shown in Fig. 2(c). The integrating sphere also allows the angle of incidence to be adjusted to determine the effect of the angle of incidence on the various reflected and transmitted components. Two separate experiments are performed using the integrating sphere. First, the properties of the microtextured PDMS material are characterized to determine the dependence of reflectance on angle of incidence. For this experiment, the transmitted light component is absorbed by a black absorber that is independently characterized. The black absorber reflected component is subtracted from the result for PDMS and microtextured PDMS. The second experiment using the integrating sphere examines the light reflecting properties of the microtextured PDMS surface as applied to a polished silicon surface.

Optical measurements are carried out using light perpendicularly polarized from a helium–neon gas laser (JDS Uniphase Model 1508P-1, JDS Uniphase Corp., USA). The surface profile of the replicated surface microstructure height variation measure-

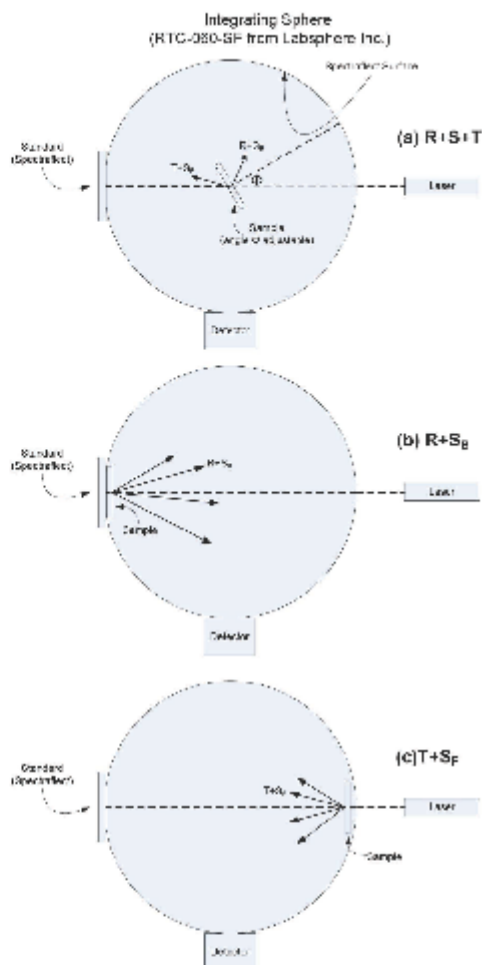


Fig. 2. (Color online) Optical characterization using Integrating sphere showing (a) the total unabsorbed power transmitted (T) plus scattered (S) plus reflected (R), (b) the reflected (R) power plus the back-scattered power (S_B), and (c) the transmitted (T) plus the forward scattered power (S_F).

ments are carried out using a SUPRA 40 scanning electron microscope (SEM) (Carl Zeiss, Germany) and a Dektak stylus profilometer (Veeco Instruments Inc., USA).

3. Results and Discussion

Figures 3(a) and (b) show SEM images of Ti and Si surfaces that have been microtextured with an ultra-fast laser source in a manner demonstrated previously [22–24]. The images in Figs. 3(c) and (d) show the replicated PDMS surface using Ti and Si microtextured surfaces as masters. These results

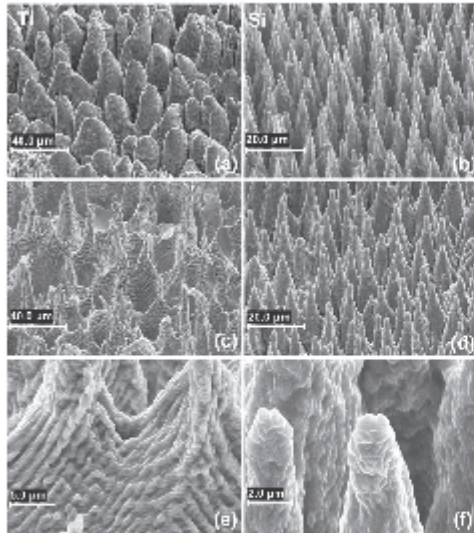


Fig. 3. SEM images of (a) ultrafast laser-treated surface showing the formation of microstructures and nanostructures on the Ti master, (b) the Si master, (c) replication in PDMS of microstructures and nanostructures that have been replicated from the Ti mold, (d) replication in PDMS of microstructures and nanostructures from the Si master, (e) higher magnification of PDMS showing detail of microstructures and nanostructures that have been replicated from the Ti mold, and (f) higher magnification of PDMS showing detail microstructures and nanostructures that have been replicated from the Si mold.

are demonstrated by producing a simple mold of the microtextured master as detailed in Section 2 using the mold method shown in Fig. 1(a). Upon detailed examination, it is seen that the submicrometer detail on the surface of the conical structures was replicated in the walls of the structures. This replicated submicrometer detail was visible in replications of both the Ti and Si as masters. This detail is visible in the SEM images of Figs. 3(e) and (f). These SEM images show detail replication at the nanoscale and higher magnification images of the PDMS surface shown in Figs. 3(c) and (d).

To determine the properties of the replicated surface, additional analysis of a cross section are performed using the SEM. Figure 4 shows the cross-section image for a replicated sample produced from a microtextured Si surface. In the cross section shown, the height of the surface features is measured as $17.1 \mu\text{m}$ and the typical distance between pillars is approximately $10 \mu\text{m}$, which is consistent with the detail seen on the Si master shown in Fig. 3(b).

In comparing the morphology of the replicated samples with their respective masters, it is seen that the Si replicated sample of Fig. 3(d) is a more faithful replication, with respect to similar feature size and distribution, to the master shown in Fig. 3(b). The

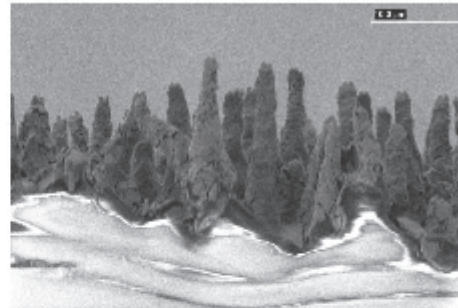


Fig. 4. Cross section of PDMS microtexture replicated from Si master.

features of the Ti replicated sample of Fig. 3(c), however, are seen to be different from the master shown in Fig. 3(a). The shape of the Ti replicated features is seen to be cup shaped, whereas the master features are seen to resemble egg shapes. The sticking of the PDMS during the replication process accounts for the fact that the Si replicated samples separated easily from the master, whereas the Ti replicated samples are quite difficult to separate from the master.

The simplicity of the replication process and the fidelity of the replication encouraged the development of an embossing process with the goal of replicating these features on the surface of some useful substrate, such as glass or Si.

An example of the results of the embossing process is shown in Fig. 1(c), which shows a film of PDMS with the embossed surface microtexture. This film was made on a glass substrate and the film was carefully removed from the substrate for analysis. The embossing replication process in PDMS is initially attempted using a glass substrate due to the availability, robustness, and optical characteristics of the glass (microscope slides). Optical analysis of microtextured silicon has been performed in the past using an integrating sphere [9]. It was decided that this microtexture might have applications as a light trapping structure for use on photovoltaic devices. A sample of polished silicon coated with PDMS film is embossed using the method depicted in Fig. 1(b).

The TILS power ($R + S + T$) is measured using the experimental fixture shown in Fig. 2(a) and described in Section 2. The scattering power is further broken down into the reflected plus backscattered power ($R + S_B$) and the transmitted plus forward scattered power ($T + S_F$), and these results are shown in Table 1. Several samples are analyzed, including PDMS with microtexture similar to the sample shown in Fig. 1(e), PDMS with microtexture on a glass substrate prepared using the embossing process, and PDMS with microtexture on a polished silicon substrate prepared using the embossing process. These results are compared to the results obtained from microtextured Ti and Si samples.

Table 1. Optical Characterization Results from Integrating Sphere Measurements* Carried Out for 633 nm Wavelength at Normal Incidence

Sample Type	$T + S_p$ (%)	$R + S_B$ (%)
PDMS texture	96.2	4.9
Glass + microtextured PDMS	93.1	5.2
Silicon + PDMS	0	25.6
Silicon + microtextured PDMS	0	15.7
Textured titanium	0	1.87
Textured silicon	0	2.04

*The measurement error is 1%–2%.

Of particular interest in Table 1 are the $R + S_B$ data. The results for the PDMS with microtexture on a polished silicon substrate are noteworthy since the reflectivity of uncoated polished Si is measured as 35% and is reduced to 25% with the addition of a 200 μm layer of PDMS. The reflectivity of Si is further reduced to 16% with the addition of PDMS microtextured film and, therefore, reflection of the Si substrate is decreased by more than 55% by the application of this simple PDMS microtextured coating. Further improvement in this result is expected by finding a similar material to PDMS with a refractive index better matched for use as an antireflective coating for use with silicon.

Figure 5 shows the results of the integrating sphere characterization of the microtextured PDMS surface. The dependence of angle of incidence on the reflectance is shown and comparison is shown among PDMS film, PDMS film predicted value, and microtextured PDMS. The predicted values were calculated using a MATLAB implementation of the Fresnel equations for reflection. The black paper used as an absorber for transmitted light, reflects/scatters an average of 8% of the incident light. The use of the absorber allows measurement of the angular dependence of the reflected/scattered light using

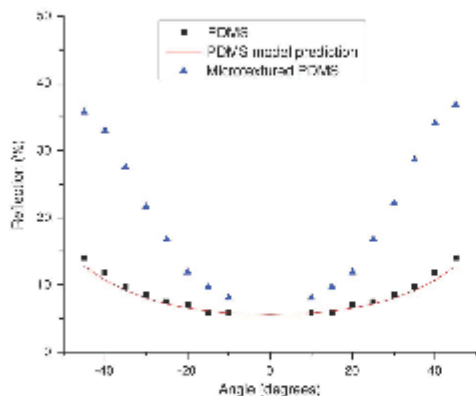


Fig. 5. (Color online) Reflection as a function of angle at 633 nm wavelength for PDMS film, PDMS film prediction, and microtextured PDMS. The reflection includes contributions from front and back surfaces.

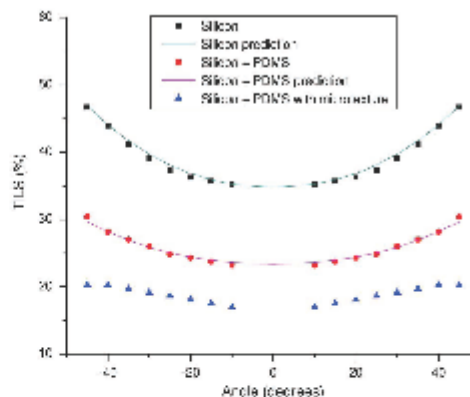


Fig. 6. (Color online) TILS as a function of angle at 633 nm wavelength for polished silicon, polished silicon prediction, silicon with PDMS film, silicon with PDMS film prediction, and silicon plus microtextured PDMS.

the integrating sphere. The total reflection for the microtextured PDMS is smaller than the data shown in Fig. 5 as there is a light-coupling phenomenon that allows light to escape from the edge of the film that is added to the integrating sphere power value. Additional details of this light coupling phenomenon will be presented in a future manuscript.

Based on the results of the integrating sphere characterization of the microtextured PDMS, a microtextured PDMS film is applied to a polished silicon surface as an antireflection-type layer for photovoltaic applications. The microtextured side of the PDMS film is applied facing up. TILS measurements are made while changing the angle of incidence of the laser light to determine the effect of angle of incidence upon the TILS power of the microtextured PDMS on the silicon surface. The measured values compare very well to the value generated from a PV Optics model simulation [25]. The results of these measurements are displayed in Fig. 6. The data show that the reflectivity is extremely flat over a wide range of angles of incidence and the measured values are very close to the predicted values.

4. Conclusions

Replication of ultrafast-laser-induced microstructures and nanostructures on PDMS is demonstrated. Different types of microstructures and nanostructures are replicated using two different types of masters, such as microtextured Ti and Si. The replicated microtextured PDMS film is applied on a silicon surface, and optical characterization shows that surface reflectance can be suppressed over 55% compared to the control value. This process may find many potential applications in photovoltaics, photodetectors, and other photonic devices, and it is relatively easy to adapt to industrial scale.

We acknowledge the NASA Langley Professor and National Science Foundation (NSF) Industry/University Cooperative Research Centers (I/UCRC) programs for their support.

References

1. S. J. Martin, K. O. Wesendorf, C. T. Gebert, G. C. Frye, R. W. Cernosek, L. Cassano, and M. A. Mitchell, "Measuring liquid properties with smooth- and textured-surface resonators," in *Proceedings of the IEEE International Symposium on Frequency Control* (IEEE, 1993), Vol. 47, pp. 603-608.
2. J. Zhao, A. Wang, P. Campbell, and M. A. Green, "22.7% efficient silicon photovoltaic modules with textured front surface," *IEEE Trans. Electron Devices* **46**, 1495-1497 (1999).
3. J. M. Gee, H. L. Tardy, T. D. Hund, R. Gordon, and H. Liang, "Reflectance control for multicrystalline-silicon photovoltaic modules using textured-dielectric coatings," in *IEEE Photovoltaic Specialists Conference* (IEEE, 1994), Vol. 2, pp. 1274-1277.
4. M. X. Su, A. J. Fleischman, S. Roy, R. A. Banks, S. K. Miller, and R. J. Michura, "Osteoblast attachment to a textured surface in the absence of exogenous adhesion proteins," *IEEE Trans. Nanobiosci.* **2**, 287-294 (2003).
5. P. Campbell and M. A. Green, "Light trapping properties of pyramidally textured surfaces," *J. Appl. Phys.* **62**, 243-249 (1987).
6. J. M. Gee, W. K. Schubert, H. L. Tardy, T. D. Hund, and G. Robison, "The effect of encapsulation on the reflectance of photovoltaic modules using textured multicrystalline-silicon solar cells," in *IEEE Photovoltaic Specialists Conference* (IEEE, 1994), Vol. 2, pp. 1555-1558.
7. D. H. Macdonald, A. Cuevas, M. J. Kerr, C. Samundsett, D. Ruby, S. Winderbaum, and A. Leo, "Texturing industrial multicrystalline silicon solar cells," *Solar Energy* **76**, 277-283 (2004).
8. T. Matsui, M. Tsukiji, H. Saika, T. Toyama, and H. Okamoto, "Influence of substrate texture on microstructure and photovoltaic performances of thin film polycrystalline silicon solar cells," *J. Non-Cryst. Solids* **299**, 1152-1156 (2002).
9. V. V. Iyengar, B. K. Nayak, and M. C. Gupta, "Optical properties of silicon light trapping structures for photovoltaics," *Sol. Energy Mater. Sol. Cells* **94**, 2251-2257 (2010).
10. J. Yoo, G. Yu, and J. Yi, "Black surface structures for crystalline silicon solar cells," *Mater. Sci. Eng. B* **159**, 333-337 (2009).
11. Y. Xia, J. A. Rogers, K. E. Paul, and G. M. Whitesides, "Unconventional methods for fabricating and patterning nanostructures," *Chem. Rev.* **99**, 1823-1848 (1999).
12. P. N. Vinod and M. Lal, "Surface and optical characterization of the porous silicon textured surface," *J. Mater. Sci. Mater. Electron.* **16**, 1-6 (2005).
13. P. Papet, O. Nichiporuk, A. Kaminaki, Y. Rozier, J. Kraiem, J.-F. Lelievre, A. Chaumartin, A. Fave, and M. Lemiti, "Pyramidal texturing of silicon solar cell with TMAH chemical anisotropic etching," *Sol. Energy Mater. Sol. Cells* **90**, 2319-2328 (2006).
14. W. Sparber, O. Schultz, D. Birol, G. Emanuel, R. Preu, A. Poddey, and D. Borchert, "Comparison of texturing methods for monocrystalline silicon solar cells using KOH and Na_2CO_3 ," in *Proceedings of 3rd World Conference on Photovoltaic Energy Conversion* (IEEE, 2003), Vol. 2, pp. 1372-1375.
15. M. Tucci, R. De Rosa, and F. Roca, " CF_4/O_2 dry etching of textured crystalline silicon surface in a Si:Hf-Si heterojunction for photovoltaic applications," *Sol. Energy Mater. Sol. Cells* **69**, 175-185 (2001).
16. J. Y. Chen, W.-L. Chang, C. K. Huang, and K. W. Sun, "Biomimetic nanostructured antireflection coating and its application on crystalline silicon solar cells," *Opt. Express* **19**, 14411-14419 (2011).
17. M. Nam, J. Lee, and K.-K. Lee, "Efficiency improvement of solar cells by importing microdome-shaped anti-reflective structures as a surface protection layer," *Microelectron. Eng.* **88**, 2314-2318 (2011).
18. J. Escarrié, K. Söderström, C. Battaglia, E.-J. Haug, and C. Ballif, "High fidelity transfer of nanometric random textures by UV embossing for thin film solar cells applications," *Sol. Energy Mater. Sol. Cells* **95**, 881-886 (2011).
19. N. Yamada, O. N. Kim, T. Tokimitsu, Y. Nakai, and H. Masuda, "Optimization of anti-reflection moth-eye structures for use in crystalline silicon solar cells," *Prog. Photovoltaics* **19**, 134-140 (2011).
20. J. Y. Chen, W.-L. Chang, C. K. Huang, and K. W. Sun, "Biomimetic nanostructured antireflection coating and its application on crystalline silicon solar cells," *Opt. Express* **19**, 14411-14419 (2011).
21. T. Yao, P. Wu, T. Wu, C. Cheng, and S. Yang, "Fabrication of anti-reflective structures using hot embossing with a stainless steel template irradiated by femtosecond laser," *Microelectron. Eng.* **88**, 2908-2912 (2011).
22. B. K. Nayak, M. C. Gupta, and K. W. Kolosinski, "Formation of nano-textured conical microstructures in titanium by femtosecond laser irradiation," *Appl. Phys. A* **90**, 399-402 (2008).
23. B. K. Nayak, M. C. Gupta, and K. W. Kolosinski, "Ultrafast-laser-assisted chemical restructuring of silicon and germanium surfaces," *Appl. Surf. Sci.* **253**, 6580-6583 (2007).
24. B. K. Nayak and M. C. Gupta, "Self-organized micro/nanostructures in metal surfaces by ultrafast laser irradiation," *Opt. Lasers Eng.* **48**, 940-949 (2010).
25. R. Sopori, J. Madajpour, Y. Zhang, W. Chen, S. Guha, J. Yang, A. Banerjee, and S. Hegedus, "Optical modeling of a Si solar cells," NREL/CP-520-25783, National Renewable Energy Laboratory, 1999.



Superhydrophobic surfaces by replication of micro/nano-structures fabricated by ultrafast-laser-microtexturing

Barada K. Nayak, Paul O. Caffrey, Christian R. Speck, Mool C. Gupta*

Charles L. Brown Department of Electrical and Computer Engineering, University of Virginia, Charlottesville, VA 22904, United States

ARTICLE INFO

Article history:

Received 7 May 2012

Received in revised form 24 October 2012

Accepted 12 November 2012

Available online 8 December 2012

Keywords:

Ultrafast lasers

Surface texture

Superhydrophobic surfaces

Contact angle

ABSTRACT

We report a simple and inexpensive method of producing superhydrophobic surfaces by directly replicating micro/nano-structures on to poly(dimethylsiloxane) (PDMS) from a replication master prepared by ultrafast-laser microtexturing process. No additional coatings on PDMS have been required to achieve contact angles greater than 154°. The contact angle can be controlled by changing the height of the microtextures in PDMS. Very low optical reflection properties of micro/nano textured surfaces combined with superhydrophobic characteristics make it an attractive encapsulating material for photovoltaics and other applications. Additionally, this replication method can be applied for large scale production of micro/nano textured superhydrophobic surfaces for commercial applications.

© 2012 Elsevier B.V. All rights reserved.

1. Introduction

Wetting properties of a material surface depends on both its surface energy and surface topography [1]. While lowering the surface energy of a substrate, by means of chemical coatings or treatments, can increase the contact angle (and hence decrease wettability); it is difficult to achieve water contact angle (CA) greater than 150° and sliding contact angle to less than 10° (the criterion for superhydrophobic surfaces) by surface treatment alone [2,3]. One of the most common examples of a superhydrophobic surface in nature is the lotus leaf (CA > 160°) [4]. When water falls on to the lotus leaf, it beads up to form spherical drops that roll off easily carrying away with it any dust particles on the surface. This effect is commonly referred to as the "Lotus Effect" [5,6]. This superhydrophobic behavior of the lotus leaf is attributed to the surface roughness created by randomly distributed micron scale surface features covered with nanometer scale hairs. Therefore, when water gets onto such a surface, it sits on the peaks of these surface features and beads up to form spherical droplets due to surface tension. It has been believed that appropriate surface texture is extremely important to achieve superhydrophobicity. Since decreased contact area between water and a superhydrophobic surface can reduce friction, eliminate surface contamination and lower the chances of corrosion, these superhydrophobic surfaces, therefore, have tremendous technological and industrial applications.

Numerous approaches have been employed in order to create appropriate surface microtexture for fabricating superhydrophobic surfaces. Some of those methods are lithographically patterned surfaces in combination with self-assembled monolayers or silanization [7–9], vertically aligned carbon nanotubes [10,11], electrodeposited ZnO [12], anodically oxidized aluminum [13], sublimation of aluminum acetylacetonate [14], aligned nanofiber and extruding of polymers [15,16], sol-gel method [17,18], vapor deposition [19–21], and other methods [22–24]. The common approach among all these techniques lies on creating certain surface roughness in micro/nano scale. Ultrafast laser irradiation is an effective technique to create micro/nano structures in semiconductors, metals as well as insulators [25–29]. Baldacchini et al. reported superhydrophobic surface preparation by coating fluoro-silane on femtosecond laser irradiated silicon [30]. Yoon et al. reported superhydrophobic surface in poly(dimethylsiloxane) (PDMS) by creating hemispherical nanostructures and microscaled papilla by ultrafast laser irradiation [31]. Here we report a simple and inexpensive process of fabricating superhydrophobic surface on PDMS by directly replicating self-organized micro/nano structures from a master prepared by ultrafast laser irradiation. No additional surface treatment or coatings have been required to achieve superhydrophobicity on the replicated PDMS surfaces and the master can be used multiple times for the replication process.

Recently there is growing interest in the photovoltaic community to consider using PDMS as encapsulating material in place of traditionally used ethylene vinyl acetate (EVA) due its exceptional natural stability. PDMS withstands thermal and ultraviolet light induced stress whereas chemical instability in EVA causes

* Corresponding author. Tel.: +1 434 924 6167; fax: +1 434 924 8818.
E-mail address: mgupta@virginia.edu (M.C. Gupta).

creep and/or delamination to occur [32]. In a recent communication we have shown that by applying a thin replicated-microtextured-PDMS film on polished silicon can suppress its surface reflectance over 55% at 633 nm wavelength [33]. Therefore, low reflection properties of microtextured surfaces combined with superhydrophobic characteristics make it an attractive encapsulating material for photovoltaic and other applications. Additionally, this replication method can be applied for large scale production of micro/nano textured surfaces for commercial applications.

2. Experimental procedure

Two types of microtextured masters are prepared for replication study: Si and Ti. Microtextured Si and Ti samples are prepared using a Ti-Sapphire ultrafast laser system operating at 800 nm wavelengths, 1 KHz repetition rate and 130 fs pulse width. The laser fluence is kept constant at 0.8 J/cm^2 for Si and 1 J/cm^2 for Ti. Large area masters are prepared by translating the samples under the laser beam and overlapping the laser processed lines for microtexture uniformity. Average number of laser shots at any given point on the sample surface is controlled by adjusting the translation speed of the sample. Keeping the fluence constant, the number of laser shots is varied to generate different texture heights. The details of textured replication master fabrication process can be found in the following references [26–28]. After microtexturing is completed, the master is ultrasonically cleaned in methanol and water and dried. The replication masters for this study are $1 \text{ cm} \times 1 \text{ cm}$ in size and are used to replicate micro/nano structures on to PDMS. The replication is carried out by embossing the microtextured masters on to PDMS and curing at 80°C . The detailed replication process is described in our recent communication [33].

Static contact angle measurements are carried out on replicated PDMS surfaces using the sessile drop method. A $10 \mu\text{l}$ distilled water droplet is gently positioned on the micro/nano structure replicated PDMS surface using a micro-syringe and images are captured to measure the contact angle. Successive measurements are reproducible within $\pm 1^\circ$. The mean CA value is calculated from at least five individual measurements. A stage attached to a rotation platform allows continuous inclination of the surface from horizontal and is used in order to determine the angle at which the drop starts to roll off, the so called “sliding angle”. A high resolution camera is used to record the drop images and value of CA is extracted by contouring the image using ImageJ software with the Drop Snake plug-in [34].

3. Results and discussion

Fig. 1(a) and (b) shows the SEM images of PDMS replicated surfaces produced from Ti and Si master respectively. Microtexture heights for these samples are $\sim 30 \mu\text{m}$, and spacing $\sim 20 \mu\text{m}$ for Ti and $\sim 10 \mu\text{m}$ for Si. These surfaces show superhydrophobic behavior with CA over 154° . Fig. 1(c) and (d) show the images of water drop on plane PDMS and replicated surfaces respectively. Fig. 2(a–f) show the replicated PDMS surfaces using Ti masters with different microtexture heights. These heights vary from $\sim 1 \mu\text{m}$ to $\sim 35 \mu\text{m}$ which corresponds to the Ti masters prepared with 60 to 450 laser shots. We measure the CA on each of these surfaces and the images of the water drops with simulated contour around are shown in the Fig. 3. A plot between CA versus texture height is drawn and is shown in Fig. 4. It is evident from the Fig. 4 that CA dependence curve has two distinct regions: a steep rise region (for lower texture height samples) and relatively slow rise regions (for higher texture height regions). It is a well-known fact that appropriate surface roughness plays an important role in producing superhydrophobic surfaces. The addition of surface microtexture can increase or

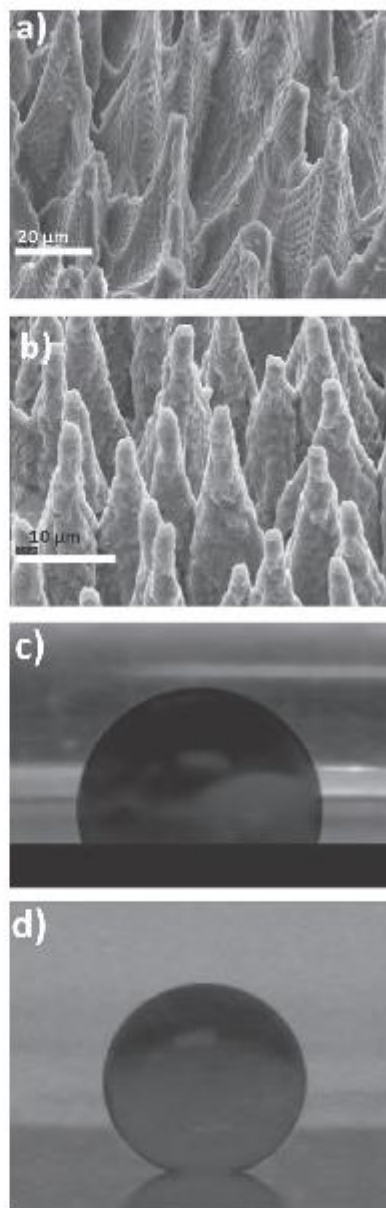


Fig. 1. SEM image of replicated micro/nano structures on PDMS surfaces from ultrafast laser textured masters: (a) Ti (b) Si. Optical images of water drop on: (c) plane PDMS (d) micro/nano structure replicated PDMS surface.

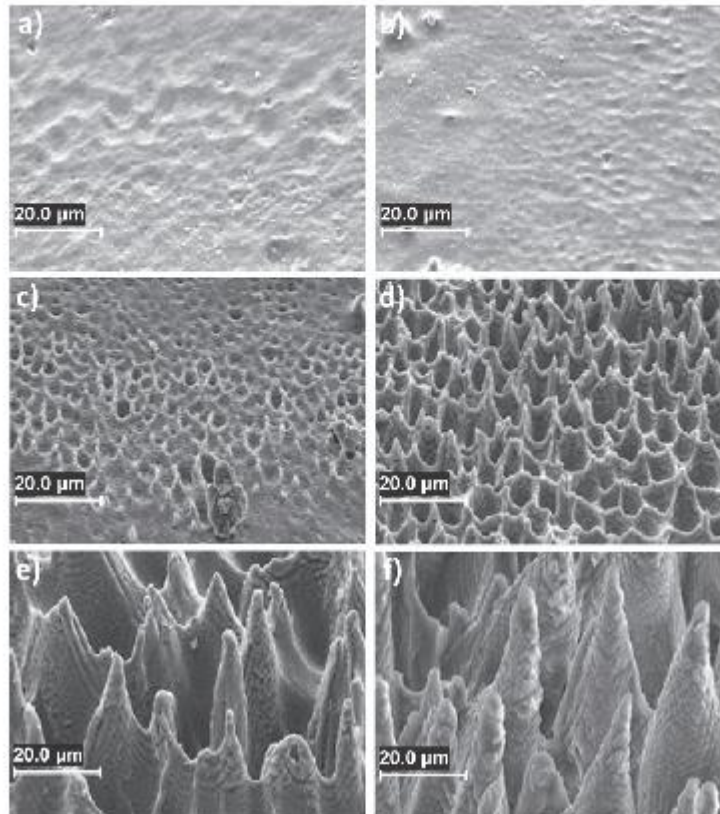


Fig. 2. SEM images of replicated PDMS surfaces created from textured Ti masters prepared at fluence 1.2 J/cm^2 for different number of laser shots (a) 60 (b) 125 (c) 175 (d) 250 (e) 350 (f) 450.

decrease CA depending on whether the “Lotus Effect” is attained or not. This can be explained by two models: the Wenzel model [35] and the Cassie-Baxter model [36] given by equations (1) and (2) respectively:

$$\cos \theta^* = r \cos \theta \text{ [Wenzel model]} \tag{1}$$

$$\cos \theta^* = -1 + \Phi_s(1 + \cos \theta) \text{ [Cassie – Baxter model]} \tag{2}$$

Where: θ^* is apparent CA for a droplet on a surface; θ is the equilibrium CA (determined on a flat surface); r is the ratio of the actual over the apparent surface area of the substrate (a number larger than 1); Φ_s is the fraction of solid in contact with liquid (a dimensionless quantity smaller than 1). In the Wenzel case, the liquid is in contact with the surface at all points and the hydrophobicity is enhanced due to an increase in the interfacial area between solid and liquid. In the Cassie-Baxter case, the surface contains air traps into which liquid is unable to penetrate, so that the interface between solid and liquid becomes a composite: solid/liquid and liquid/air. Therefore, a microtexture of taller in height will behave like a “Cassie” surface where as a texture which is shorter in height will act like a Wenzel surface. A threshold value θ_c that obeys both regimes can be obtained by equating equations (1) and (2):

$$\cos \theta_c = (\Phi_s - 1)/(r - \Phi_s) \tag{3}$$

where $\cos \theta_c$ is a quantity whose value is in between -1 and 0 . By linear curve fitting the Cassie and Wenzel lines (shown in Fig. 4) and solving the empirical equations, the threshold angle, θ_c is obtained to be $\sim 129^\circ$. From equation (1), for $\theta^* = 129^\circ$ and $\theta = 92^\circ$ (measured value), we obtain $r \sim 18$. Similarly, from equation (2), for $\theta^* = 129^\circ$ and $\theta = 92^\circ$, we obtain $\Phi_s \sim 0.38$. However, for CA of 154° , Φ_s is about 0.1 ; in this case the water drop is in contact with about 10% of the total area available. From solving two empirical equations obtained from fitting two straight line curves for Wenzel and Cassie regime we also get the transition texture height needed to enter Cassie mode from Wenzel mode is about $4.2 \mu\text{m}$. This transition at a microtexture height of $4.2 \mu\text{m}$ agrees well with the value of $4.5 \mu\text{m}$ reported by Yeh et al. using advancing and receding contact angle measurements [37] for textured surfaces. In Yeh et al. the advancing CA of 154° remains constant above a pillar height of $4.5 \mu\text{m}$. However we observe an advancing CA of only 129° for a pillar height of $4.2 \mu\text{m}$. So, for a microtextured surface like ours, the CA can continue to increase as observed in our results. The CA can also depend on the shape, sizing and spacing of the microstructures. This is why we continue to see a dependency on microtexture height above $4.5 \mu\text{m}$.

Based on our measurements we clearly observe two distinct regions (as shown in Fig. 4) when we varied texture height from

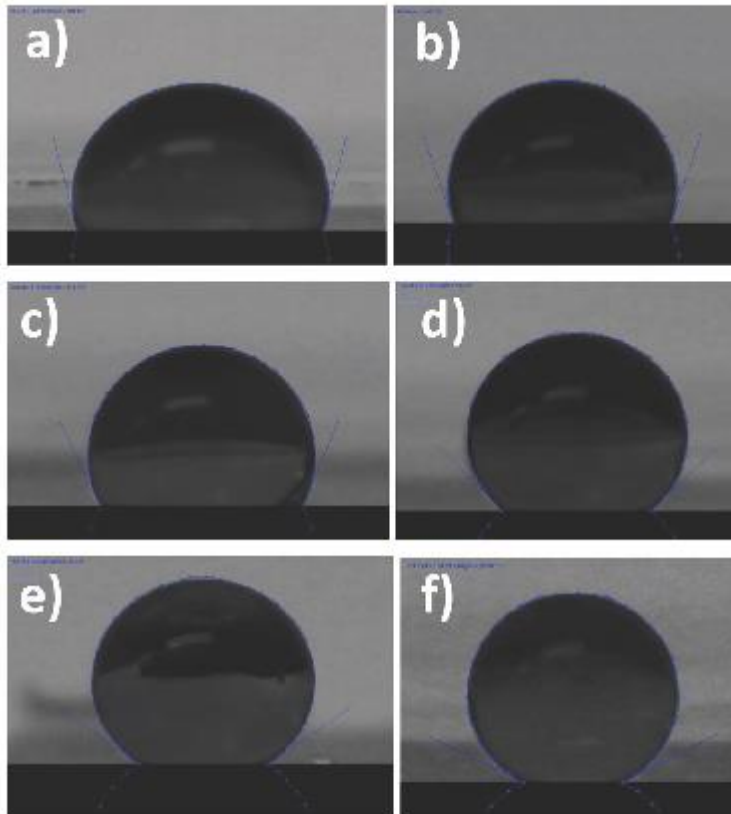


Fig. 3. Optical images of water drop for different texture heights (a) 1 μm (b) 1.6 μm (c) 3.3 μm (d) 6.4 μm (e) 25.5 μm (f) 35.8 μm .

1 μm to 35.8 μm . While the contact angle value for the texture height of 6.2 μm falls into the Cassie-Baxter region in our measurement, however, the drop is indeed observed to be pinned. The contact angle for 4.2 μm is 129.60° and the contact angle for 6.0 μm

is 131.27°, so the difference is 1.67°. Our contact angle measurements are reproducible to $\pm 1^\circ$. The difference between the contact angles at 4.2 μm and 6.0 μm is within experimental error. According to Roach et al. [38] on surfaces with a simple roughness both states are easy to define but multilayered or complex roughness (as in our case [33]) allow a mixture of the two equations to apply; and hence on these surfaces it is often difficult to determine a value for r and Φ_s .

In addition to CA greater than 154°, superhydrophobic surfaces also exhibit small sliding angles. We measured the sliding angles for the samples with different texture heights and results are tabulated in Table 1. It is clear that the drop is pinned even for texture height $\sim 6 \mu\text{m}$ indicating that taller pillars favor superhydrophobicity. However, for tall pillars ($\sim 30 \mu\text{m}$) the sliding angle is less than 6°. This situation is consistent with Cassie-Baxter model as the tall and sharp microtextures create the necessary air trapings to destabilize the water droplet [7]. The small contact area between water and the tip of the microtexture results in a small Φ_s . From equation (2), as Φ_s decreases, θ' increases and hence it becomes easy for the water droplet to roll-off from the taller microtextured surfaces. On the other hand, when the microtextures are not sufficiently tall, the water droplet becomes more stable causing the droplet to be pinned easily. We have also studied

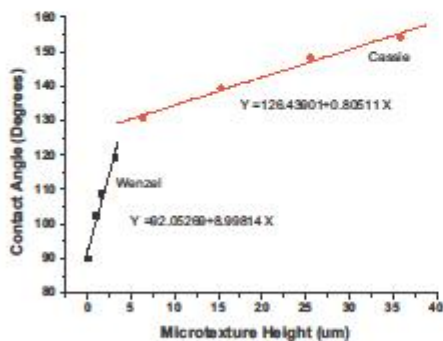


Fig. 4. Variation of contact angle with microtexture height.

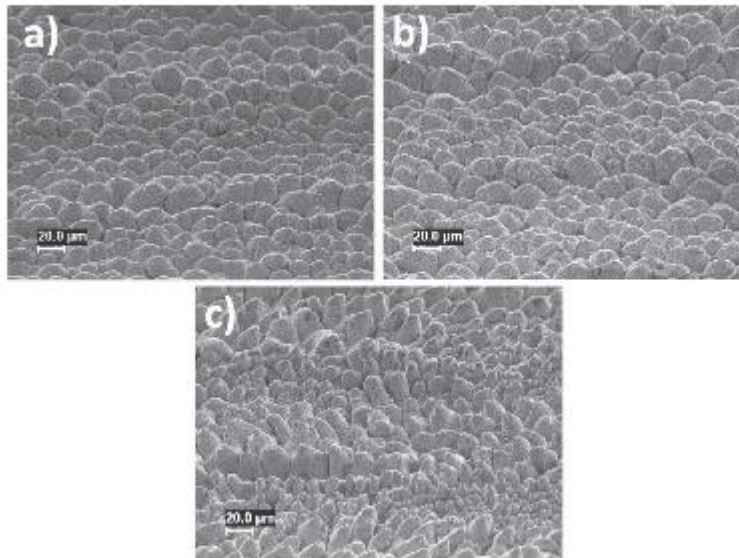


Fig. 5. SEM image of Ti master after various numbers of replications, (a) 5, (b) 10, and (c) 25.

the dynamic characteristics of water droplets on the replicated textured PDMS surface. The values for the advancing and receding contact angles are 157° and 151° respectively for the microtexture height of 35.8 μm – giving a contact angle hysteresis of 6°.

There is no apparent surface degradation of the master with repeated replications as seen in Fig. 5 where SEM images are taken of masters with various numbers of replications. This is due to the softness of the cured PDMS material compared to the hardness of the Ti master and also no external load was applied during the replication process. In addition PDMS exhibits up to 3% shrinkage [39] during the curing process which aids removal from the master.

In order to investigate the effect of water drop size on the CA, we measured CA of a water drop of 10 μl over 2 h time period. As the evaporation caused reduction in the size of the water droplet, the contact angle also started to reduce. Fig. 6(a) shows the effect of time on the CA for a water drop sitting on a textured PDMS surface. The CA drops quickly with time and then decreases very slowly while the volume of the water dropped almost linearly (as shown in Fig. 6(b)) over the entire 2 h duration. Our observation of the change in CA as the drop evaporates is consistent with the results observed by McHale et al. on a Su-8 surface [40] and by Moulinet et al. on a silicon surface coated with a fluoropolymer [41].

Table 1
Sliding angle for water on micro/nano structure replicated PDMS surfaces for different microtexture heights.

Texture height (μm)	Contact angle (degrees)	Sliding angle (degrees)
0	92	Pinned
1	102.4	Pinned
1.6	108.7	Pinned
3.3	119.3	Pinned
6.4	130.6	Pinned
15.3	139.4	<90
25.5	148.3	<15
35.8	154.2	<6

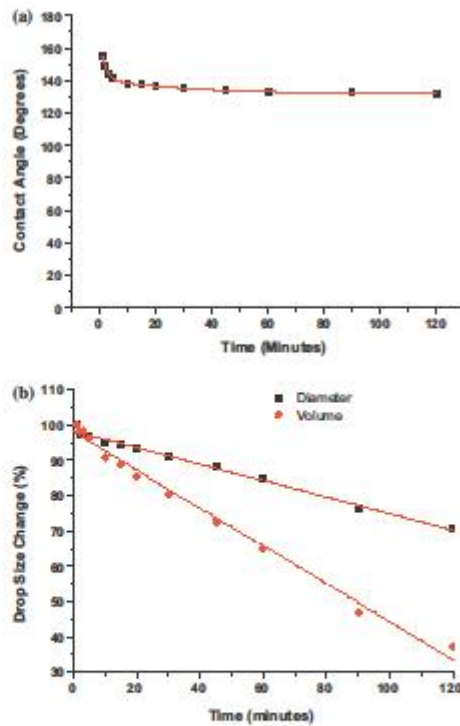


Fig. 6. Time dependence of (a) contact angle and (b) drop size of a water droplet sitting on the micro/nano structured PDMS surface.

4. Conclusions

In conclusion, we demonstrate a simple and inexpensive method of producing superhydrophobic surfaces by directly replicating micro/nano-structures on to PDMS from masters prepared by ultrafast-laser-microtexturing process. No additional coatings are required to achieve contact angles greater than 154°. The contact angle can be controlled by changing the height of the microtextures in PDMS and a minimum texture height of about 4.2 μm is needed for the replicated surfaces to enter into the Cassie regime. The replication process is applicable to other polymeric and plastic materials. Very low optical reflection properties of micro/nano textured surfaces combined with superhydrophobic characteristics make it an attractive encapsulating material for photovoltaics and other outdoor applications. Also, these superhydrophobic surfaces can be large-scale produced for commercial applications.

Acknowledgement

We acknowledge the NASA Langley Professor Program for the financial support.

References

- [1] A. Lahma, D. Quere, *Nature Materials* 2 (2003) 457–460.
- [2] T. Nishino, M. Meguro, K. Nakamae, M. Matsushita, Y. Ueda, *Langmuir* 15 (1999) 4321–4323.
- [3] Y. Xiu, L. Zhu, D.W. Hess, C.P. Wong, *Nano Letters* 7 (2007) 3388–3393.
- [4] C. Neinhuis, W. Barthlott, *Annals of Botany* 79 (1997) 667–677.
- [5] H. Tavana, A. Amirfazli, A.W. Neumann, *Langmuir* 22 (2006) 5556–5559.
- [6] W. Barthlott, C. Neinhuis, *Planta* 202 (1997) 1–8.
- [7] D. Öner, T.J. McCarthy, *Langmuir* 16 (2000) 7777–7782.
- [8] Z. Burton, B. Bhushan, *Nano Letters* 5 (2005) 1607–1613.
- [9] J.-Y. Shiu, C.-W. Kuo, P. Chen, C.-Y. Mou, *Chemistry of Materials* 16 (2004) 561–564.
- [10] K.K.S. Lau, J. Bico, K.B.K. Teo, M. Chhowalla, G.A.J. Amaralunga, W.I. Milne, G.H. McKinley, K.K. Gleason, *Nano Letters* 3 (2003) 1701–1705.
- [11] L. Zhu, Y. Xiu, J. Xu, P.A. Tamirisa, D.W. Hess, C.-P. Wong, *Langmuir* 21 (2005) 11208–11212.
- [12] M. Li, J. Zhai, H. Liu, Y. Song, L. Jiang, D. Zhu, *The Journal of Physical Chemistry B* 107 (2003) 9954–9957.
- [13] S. Shibuichi, T. Yamamoto, T. Onda, K. Tsujii, *Journal of Colloid and Interface Science* 208 (1998) 287–294.
- [14] A. Nakajima, A. Fujishima, K. Hashimoto, T. Watanabe, *Advanced Materials* 11 (1999) 1365–1368.
- [15] L. Feng, S. Li, H. Li, J. Zhai, Y. Song, L. Jiang, D. Zhu, *Angewandte Chemie* 114 (2002) 1269–1271.
- [16] L. Feng, Y. Song, J. Zhai, B. Liu, J. Xu, L. Jiang, D. Zhu, *Angewandte Chemie* 115 (2003) 824–826.
- [17] N.J. Shirtcliffe, G. McHale, M.I. Newton, C.C. Perry, *Langmuir* 19 (2003) 5626–5631.
- [18] K. Tadanaga, J. Morinaga, A. Matsuda, T. Minami, *Chemistry of Materials* 12 (2000) 590–592.
- [19] H. Liu, L. Feng, J. Zhai, L. Jiang, D. Zhu, *Langmuir* 20 (2004) 5659–5661.
- [20] J.C. Love, B.D. Gates, D.B. Wolfe, K.E. Paul, G.M. Whitesides, *Nano Letters* 2 (2002) 891–894.
- [21] A. Nakajima, K. Hashimoto, T. Watanabe, K. Takai, G. Yamauchi, A. Fujishima, *Langmuir* 16 (2000) 7044–7047.
- [22] T.N. Krupenkin, J.A. Taylor, T.M. Schneider, S. Yang, *Langmuir* 20 (2004) 3824–3827.
- [23] M. Jin, X. Feng, L. Feng, T. Sun, J. Zhai, T. Li, L. Jiang, *Advanced Materials* 17 (2005) 1977–1981.
- [24] S. Wang, L. Feng, L. Jiang, *Advanced Materials* 18 (2006) 767–770.
- [25] T.H. Her, R.J. Finlay, C. Wu, E. Mazur, *Applied Physics A: Materials Science & Processing* 70 (2000) 383–385.
- [26] B.K. Nayak, M.C. Gupta, K.W. Kolasinski, *Nanotechnology* 18 (2007) 195302.
- [27] B.K. Nayak, M.C. Gupta, K.W. Kolasinski, *Applied Physics A: Materials Science & Processing* 90 (2008) 399–402.
- [28] B.K. Nayak, M.C. Gupta, *Optics and Lasers in Engineering* 48 (2010) 940–940.
- [29] K.K.C. Lee, P.R. Herman, T. Shoa, M. Haque, J.D.W. Madden, V.X.D. Yang, *Advanced Materials* 24 (2012) 1243–1246.
- [30] T. Baldacchini, J.E. Carey, M. Zhou, E. Mazur, *Langmuir* 22 (2006) 4917–4919.
- [31] T.O. Yoon, H.J. Shin, S.C. Jeoung, Y.-I. Park, *Optics Express* 16 (2008) 12715–12725.
- [32] M.D. Kempe, *Photovoltaics International Journal* (2010) 170–177, 9th Edition.
- [33] P.O. Calfrey, B.K. Nayak, M.C. Gupta, *Applied Optics* 51 (2012) 604–609.
- [34] W. Rasband, Research Services Branch, National Institute of Mental Health, Bethesda, Maryland, USA, 2011.
- [35] R.N. Wenzel, *Industrial & Engineering Chemistry* 28 (1936) 988–994.
- [36] A.B.D. Cassie, S. Baxter, *Transactions of the Faraday Society* 40 (1944) 546–551.
- [37] K.-Y. Yeh, L.-J. Chen, J.-Y. Chang, *Langmuir* 24 (2007) 245–251.
- [38] P. Roach, N.J. Shirtcliffe, M.I. Newton, *Soft Matter* 4 (2008) 224–240.
- [39] S. Lee, S. Lee, *Microsystem Technologies* 14 (2008) 205–208.
- [40] G. McHale, S. Aqil, N.J. Shirtcliffe, M.I. Newton, H.Y. Erbil, *Langmuir* 21 (2005) 11053–11060.
- [41] S. Moulinet, D. Bartolo, *The European Physical Journal E: Soft Matter and Biological Physics* 24 (2007) 251–260.



Electrically conducting superhydrophobic microtextured carbon nanotube nanocomposite



Paul O. Caffrey, Mool C. Gupta*

Department of Electrical & Computer Engineering, University of Virginia, Charlottesville, VA 22904, USA

ARTICLE INFO

Article history:

Received 24 December 2013

Received in revised form 6 June 2014

Accepted 9 June 2014

Available online 17 June 2014

Keywords:

Surface microtexture

Superhydrophobic surfaces

Contact angle

Conductive polymer

Nanocomposite

ABSTRACT

We report a simple and inexpensive method of producing an electrically conductive superhydrophobic polymer surface by adding multiwall carbon nanotubes directly into the polymer poly(dimethylsiloxane) (PDMS) matrix and replicating micro/nanotexture using a replication master prepared by ultrafast-laser microtexturing process. No additional coatings on conducting PDMS are required to achieve water contact angles greater than 161° . The conductivity can be controlled by changing the percent MWCNT added to PDMS and at a bulk loading of 4.4 wt% we report a conductivity improvement over pure PDMS by a factor of more than 10^{11} with electrical resistivity $\rho = 761 \Omega \text{ cm}$. This combined behavior of a conductive, superhydrophobic nanocomposite has exciting applications for allowing a new class of enclosures providing EMI shielding, water repellency and sensing to provide built-in temperature feedback. The effect of temperature on the nanocomposite was investigated and a negative temperature coefficient of resistance ($-0.037 \Omega/\text{K}$) similar to that of a thermistor was observed.

© 2014 Elsevier B.V. All rights reserved.

1. Introduction

With the rapid growth of high-speed electronic devices operating in the 1–10 GHz frequency range, especially computing equipment, there is an ever-increasing need for effective electrical shielding both for and from this sensitive equipment. The Federal Communications Commission (FCC) specifically regulates emissions in the range 30 MHz–5 GHz [1,2] and since space, shape and weight are primary design factors in this class of equipment the enclosures tend to be created from polymer materials [3]. Traditionally EMI shielding is provided to an enclosure by adding a layer of metal foil either inside the enclosure or embedded as a layer in the polymer [4]. Other methods include bulk loading of conductive particles into the polymer matrix or the addition of a conductive finish coating [3,4]. More and more these devices are required to operate in harsh environments where the sensitive devices may be exposed to water. There has been work done on the use of conductive nanomaterials [5–7] for EMI shielding and structural applications [8] but there is a need for a light weight material that is not only electrically conducting, but also has superhydrophobic properties. Recently Wang et al. [9,10] and Madeani et al. [11] demonstrated the addition of MWCNTs in

PDMS to produce a superhydrophobic nanocomposite. Zhao et al. [12], Talaemashhadi et al. [13] and Bayer et al. [14] have also reported electrically conductive superhydrophobic materials based on MWCNTs embedded in copolymers. Yao et al. [15] reported electrically conductive superhydrophobic films based on functionalized MWCNTs. Park et al. [16] demonstrated replication of a complex surface using PDMS-MWCNT nanocomposite with superhydrophobic and conductive properties.

Conductive polymer materials typically have a positive temperature coefficient (PTC) of resistance and there has been interest in these materials due to the potential for self-regulation of temperature [17]; however the nanocomposites demonstrated in this work displays a negative temperature coefficient (NTC) of resistance similar to that of a thermistor. A thermistor is a thermally sensitive resistor [18] and can be fabricated from PTC materials such as platinum film, metals such as platinum being used because of their linear temperature coefficient of resistance over a wide temperature range [18]. It is more typical to fabricate thermistors from NTC semiconductor based materials [19] as these typically have a larger temperature coefficient of resistance and can be made at very low cost. These NTC devices find uses in many circuits where temperature compensation is required [19]. The operating premise of a NTC thermistor [18,20] is that as temperature rises more electrons are promoted into the conduction band and the resistance to current flow decreases. Little or no suitable explanation for NTC [21] nanocomposites materials has been suggested especially where the

* Corresponding author.

E-mail address: mgupta@virginia.edu (M.C. Gupta).

Table 1
MWCNT products.

Product	Length (μm)	Diameter (nm)	Structure	Packing Density (g/cm^3)	Resistivity at 1 wt% (Ωcm)
PD15L15-20	15–20	15	Hollow	0.032	7×10^4
BPD30	20	30	Bamboo	0.025	3×10^4
PD30	20	30	Hollow	0.070	$>2 \times 10^{16}$
PD15L1-5	1–5	15	Hollow	0.100	$>2 \times 10^{16}$

NTC occurs below or in absence of a PTC region as nanocomposites have been shown to have a NTC area at high temperature beyond their normal operating region [21].

Lee et al. [21] explores the effect of adding multi walled carbon nanotubes (MWCNT) to a polyethylene Carbon Black (CB) nanocomposite concluding that the addition of 0.5% MWCNT stabilized the positive temperature coefficient (PTC) response of the nanocomposites. Indeed the response seen by Lee et al. [21] shows a marked flattening of the response up to the PTC threshold indicating a negative temperature coefficient component added by the addition of the MWCNT. Zhang et al. [22] surveys the literature for explanations for both PTC and NTC phenomena concluding that although there is no conclusive theory that the most widely accepted explanation is based on the tunneling effect where electron tunneling occurs across the gaps between the nanotubes and the changes in resistivity occur due to the different thermal coefficients of expansion between the polymer matrix and the nanotubes. The polymer material we have used, PDMS and nanomaterial, MWCNTs, have a large difference in the coefficient of thermal expansion (CTE). PDMS CTE is given as 310 ppm/K [23,24], the CTE for MWCNT is in the range 16–26 ppm/K [25–27]. This difference in CTE of over an order of magnitude may indeed account for the strange behavior of NTC when compared with other polymer nanocomposites. Looking again at Zhang et al. [22] the polymer is polyethylene with a CTE of 180–200 ppm/K and the nanoparticles used are Carbon black nanoparticles which have a low aspect ratio. In fact, Wei et al. [28] found using molecular dynamics (MD) simulations that the addition of CNT to the polymer matrix caused an increase of 18% to the CTE. Yi et al. [29] presents a method for eliminating the NTC and discusses an operating theory for explaining the NTC where it is seen in a nanocomposites after the PTC. In another paper [30] Yi et al. show that polyethylene composites of vanadium suboxides (V_2O_3 and VO_2) exhibit strong NTC effects over a wide range of temperatures.

Recently poly(dimethylsiloxane) (PDMS) as a material for manufacturing devices on the micron scale has attracted much attention [31–33] due to the simplicity of the fabrication processes. The addition of carbon nanotubes as a filler for PDMS had become popular in the field of micro-electromechanical systems (MEMS) [33,34]. Our earlier work [35] explored the superhydrophobic properties of PDMS with replicated surface microtexture [36]. The use of other polymers combined with carbon nanotubes has also been investigated for their use in producing superhydrophobic conductive nanocomposites. Luo et al. [37] constructed a nanocomposite using nafion and carbon nanotubes that exhibits a high contact angle ($\text{CA} = 165^\circ$) and high electrical conductivity (1600 S m^{-1}). Nafion is a perfluorosulfonated polymer with similar properties to Teflon [37,38]. The highest contact angle Luo et al. reported was at a loading of 90.2% CNT with the polymer nafion accounting for 9.8% of the weight. Luo et al. also found that increasing the nafion content above 9.8% decreased the contact angle and that the nanocomposite was no longer superhydrophobic, with a contact angle of 149.5° at a nafion loading of 21.0 wt%. It should be considered that Luo et al. are producing a thin film rather than a bulk material. Comparing the process above to our earlier superhydrophobic work [35] from a practical perspective, nafion is special polymer

currently used in the production of fuel cells and is relatively expensive [39] compared to PDMS [40]. Also, loading levels in Luo et al. [37] require greater than 41 wt% CNT. We now build on our earlier work [35] to encompass PDMS composites with various amounts of MWCNT loading to provide electrical conductivity along with superhydrophobic properties. This will fill the need outlined above for a superhydrophobic conductive nanocomposite with low loading of CNT (~ 5 wt%) that will have wide applications in many industries.

2. Experimental

2.1. Materials

PDMS was obtained from Ellsworth Adhesives (Dow Corning Sylgard 184 Silicone Encapsulant). Carbon nanotubes of dimensions outlined in Table 1 were obtained from NanoLab Inc. (PD15L15-20, BPD30, PD30, and PD15L1-5). Agitation was accomplished using an ultrasonic processor (Qsonica Q500) and a small 3.8 V dc motor. Volume and surface resistivity measurements were made using a Keithley 6105 Resistivity Adapter and for current measurements either a Keithley 616 Digital Electrometer (p-Ammeter) or a UNI-T UT803 Multi-meter (μ -Ammeter). Voltage measurements were made using a Fluke 8012A Multi-meter. Voltage was applied using either a Keithley model 240 High voltage DC supply for voltages over 30 V and for less than 30 V, a Mwtech HY3005A DC Power supply was used. For replication of the microtextured surface, a Ti master was fabricated. The self-assembled microtexture was obtained through the direct laser processing method, and the details and the novelty of this self-assembled technique and the fabrication process can be found in the following Refs. [41–43].

2.2. Preparation of MWCNT-PDMS nanocomposites

The PDMS used is a two-part polymer comprised of a base and a hardener and is mixed together at a 10:1 ratio. The MWCNTs are added to the base and must be mixed such that the MWCNT are distributed uniformly. Several methods of agitation were investigated; agitation using an ultrasonic agitator was first attempted but it was found that the solution mixture heated up significantly and became viscous resulting in premature curing. Hand mixing using a glass rod was also attempted but the resulting electrical resistances of the samples were not sufficiently low due to the fact that we were unable to increase the bulk loading to more than 3 wt%. In another method MWCNTs were mixed in toluene, and then added the resulting suspension to a toluene diluted PDMS solution similar to Liu et al. [34] a bulk loading of 2 wt% was the limit for this method. The method that was found to be most effective was simple mechanical stirring with a low RPM dc motor and using this method we were able to reach a bulk loading of 4.4 wt% and relatively high electrical conductivity.

For the fabrication of the nanocomposite, 20 g PDMS base was measured in a 50 ml flask. MWCNT was added to achieve the desired weight percent bulk loading and the resulting mixture was agitated for one hour to achieve a uniform mixture. Two grams of PDMS hardener was then added and stirred for five minutes. Ten grams

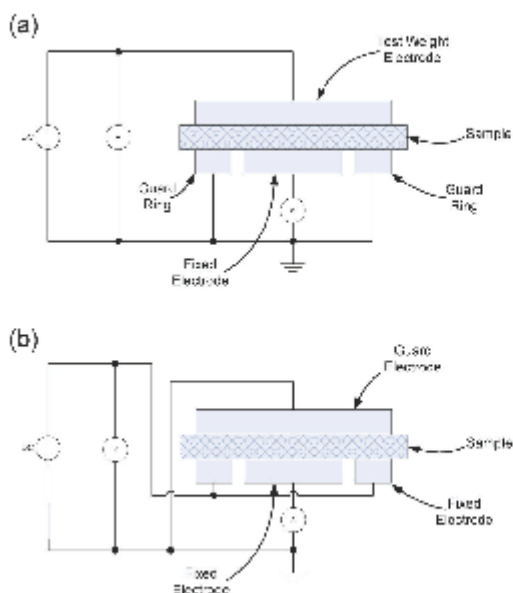


Fig. 1. Test fixture used to measure (a) volume resistivity and (b) surface resistivity.

of the resultant mixture was placed in a 75 mm diameter circular mold mounted in a 90 mm petri dish. The mold was prepared in accordance with our previously published procedure [36] and was heated for a minimum of two hours at 80 °C. This resulted in a sample thickness of 2.54 mm with a diameter of 70 mm. These dimensions are within the specifications of the resistivity adapter [44].

2.3. Characterization of MWCNT-PDMS nanocomposites

Resistivity measurements were made in accordance with ASTM D 257 [45]. Resistivity measurements, both volume and surface were made using the resistivity adapter as shown in Fig. 1(a) and (b) respectively. The resistivity adapter was first cleaned using alcohol and then a sample was placed in the adapter. Measurements were taken in accordance with the adapter instructions [44]. Three measurements were taken for each sample and averaged. A high voltage power supply and electrometer combination was used for high resistivity samples and a multi-meter and bench-top power supply was used for low resistivity samples.

Contact angle measurements were made by taking a digital image of a 10 μ l drop of water on the surface of the polymer in accordance with ASTM D 7334-08 [46]. The reading was made by loading the image in to the ImageJ software package [47] and measuring the contact angle using a drop-snake plugin [48] that allows contact angle to be directly determined from an image of a drop on the surface. Advancing and receding contact angles were measured by adding and removing volume from the drop while measuring contact angle.

In addition to contact angle, volume and surface measurements, a sample of the conductive polymer was prepared to determine the response of the nanocomposites to changes in temperature. For this experiment a sample was prepared in a rigid fixture (rigid to avoid changes in contact resistance). This fixture was heated to 165 °C and allowed to cool to -15 °C in a freezer while resistance

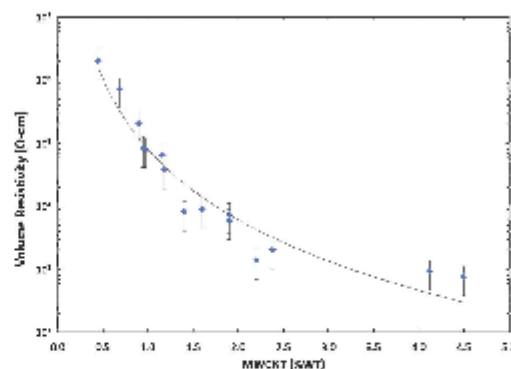


Fig. 2. Graph of volume resistivity vs. % weight MWCNT loading (note: sample is from PD15L15-20 product and is untextured).

measurements were recorded on a digital multimeter (Fluke 8012A). The control for this experiment was a 2.2 k Ω 1/4 W 5% carbon film resistor (Digikey).

3. Results and discussion

MWCNT samples of length and diameters shown in Table 1 were used to determine the effect on conductivity of the addition of MWCNT to PDMS. Four different products were tested, differing mainly in the packing density of the MWCNTs. We included a product with bamboo structure MWCNTs which have been reported [49,50] to have a higher degree of structural defects. Table 1 summarizes the dimensional and structural information on of these four MWCNT [51] products. Looking at the packing density column in Table 1 it varies by a factor of 4. The lower packing density MWCNT products were more difficult to mix with PDMS and also contributed to the selection of the specific type of MWCNT (PD15L15-20) to gather the conductivity data. The graph of Fig. 2 shows the results of measuring the volume resistivity of samples of PDMS nanocomposite with bulk loading of 0.45–4.4 wt% of MWCNT (PD15L15-20). The minimum volume resistivity measured was 761 Ω cm. This value of volume resistivity is significantly lower at low bulk loading levels (less than 5%) to that measured by Engel et al. [33] by a factor of more than 100 and is less than that of pure PDMS by a factor of more than 10¹¹. At a percolation threshold, a large increase [7] in conductivity is expected due to the interconnecting of the nanotubes. After the percolation threshold (2 wt%) a significant decrease in resistance is seen as shown by the exponential behavior in Fig. 2.

The other two MWCNT products shown in Table 1 were investigated to determine their suitability as a bulk additive for conductive nanocomposite. The BPD30 product had lower volume, was thicker (30 nm vs. 15 nm), and the resistivity of the resulting sample proved higher by a factor of more than three from the equivalent PD15L15-20 sample (3.3 k Ω cm @ 1.0 wt% loading vs. 761 Ω cm @ 4.5 wt% loading). The lower packing density of BPD30 made it impractical to increase the bulk loading beyond the 1.0 wt% value as mixing became impossible beyond that point. PD30 and PD15L1-5 are shown to have extremely high resistivity at the 1 wt% loading value compared to PD15L15-20 and BPD30. These two products had the highest packing density which may hinder the dispersion of the MWCNTs uniformly in the polymer.

Fig. 3 shows a high magnification SEM image of a PDMS-MWCNT nanocomposite sample of 2.4 wt% of MWCNT (PD15L15-20). The

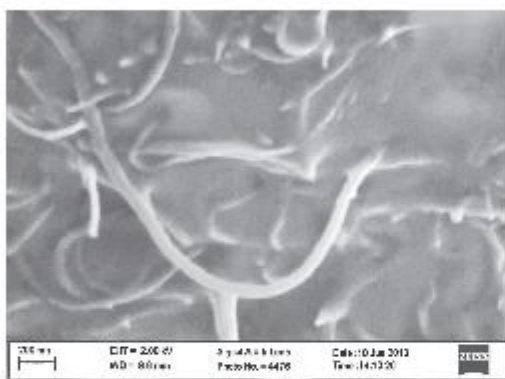


Fig. 3. SEM image of conductive PDMS matrix showing interconnecting MWCNT (note: sample is from PD15L15-20 product).

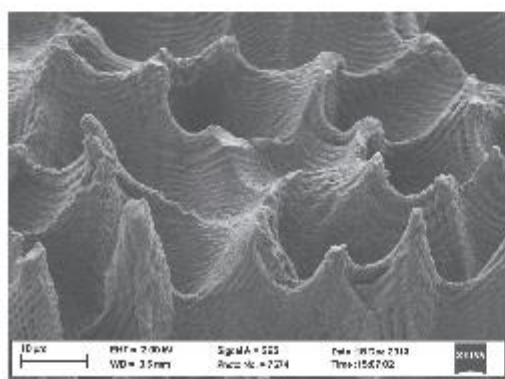


Fig. 4. SEM image of conductive PDMS microtextured surface showing microtexture features (note: sample is from PD15L15-20 product).

interconnecting of the nanotubes can be seen. This interconnecting of the conductive nanotubes forms a network [7] that is responsible for conduction [22]. Fig. 4 shows a SEM image of the PDMS-MWCNT nanocomposite that shows the microtextured surface. This sample was prepared from a microtextured Ti master and shows the characteristic cup shape imprints that come from the use of a Ti master [36]. Nanotexture can also be seen on the walls of the structures.

A study was performed to determine the contact angle of the PDMS-MWCNT nanocomposite. A series of samples were taken over the range of MWCNT loading under study and the contact angle was measured. It was observed that the contact angle did not vary with bulk loading of MWCNT within the measurement accuracy of our equipment (2%) [35]. A study was also performed on a sample of PDMS-MWCNT nanocomposite created with replicated surface microtexture similar to our earlier work [36]. Fig. 5 shows an image taken during a contact angle measurement of untextured PDMS-MWCNT nanocomposite, the measured contact angle was found to be 110° , with a contact angle hysteresis of 23° . No sliding angle measurement possible as the droplet was pinned. Fig. 6 shows an image taken during a contact angle measurement on microtextured PDMS-MWCNT nanocomposite, a value of 161° was found, with a sliding angle of 6° and a contact angle hysteresis of 3° . These

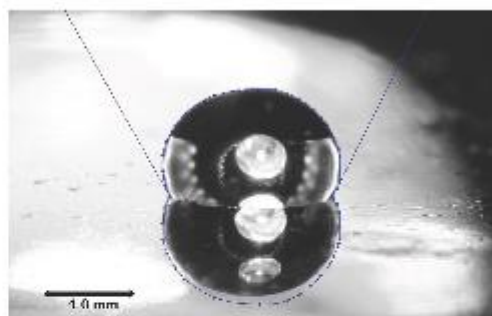


Fig. 5. Image of water droplet on surface of conductive PDMS surface displaying a contact angle of 115° (note: sample is from PD15L15-20 product and is untextured).

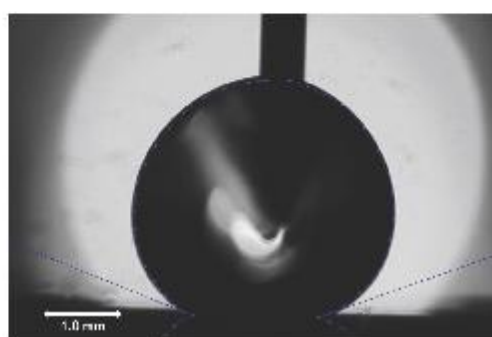


Fig. 6. Image of water droplet on surface of conductive PDMS microtextured surface displaying a contact angle of 161° (note: sample is from PD15L15-20 product).

results compare well to our earlier reported values of 154° , 6° and 6° respectively [35].

The nanocomposites based on BPD30, PD30, and PD15L1-5, failed to produce usable low resistance samples mainly due to the difficulties in mixing explained earlier so an experiment was performed to determine the temperature dependence of resistance for the nanocomposite fabricated from PD15L15-20. The results of the variation of resistance with temperature for an untextured nanocomposite comprised of 4.1 wt% of MWCNT (PD15L15-20) are shown in Fig. 7. For this experiment, the temperature was varied in five degree increments from -15°C to 165°C while resistance measurements were recorded. The control for this experiment was a carbon film resistor and its resistance was similarly recorded as the temperature was varied from -15°C to 165°C . Although the control resistor has a 5% tolerance, it shows a very small NTC of $\alpha = 193 \times 10^{-6}$ ($4.4\text{ m}\Omega/\text{K}$). By comparison the MWCNT nanocomposite displayed a NTC of $\alpha = 0.00143$ ($35.5\text{ m}\Omega/\text{K}$). From a literature search a platinum thermistor will have a PTC of $\alpha = 0.0037$ [18]. Platinum is desirable because of its linear temperature response but because of the expense of Platinum, semiconductor materials have become popular. The logarithmic response of semiconductor thermistors makes them less attractive for simple use. In comparison the linear temperature response of the PDMS-MWCNT nanocomposite shown in Fig. 7 was noted. Our equipment limited measurement range from -15°C to 165°C but PDMS has a broad operating temperature range of -55°C to 200°C [24]. PDMS is also designed for long lifetime operation in harsh conditions (PDMS is used as a solar cell encapsulant). This broad operating range

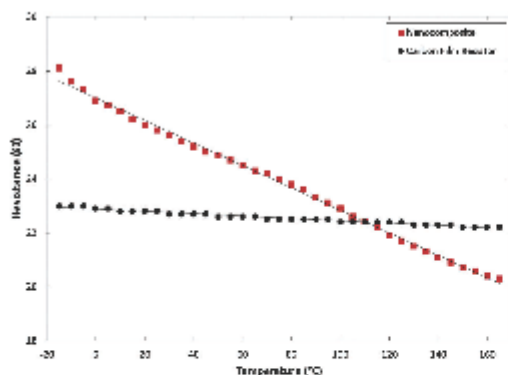


Fig. 7. Graph of resistance vs. temperature for conducting nanocomposite and control resistance (note: nanocomposite sample is from PD15L15-20 product and is untextured).

Table 2

Measurement summary for PD15L15-20 sample.

Measurement	Untextured	Textured
Static contact angle	110°	161°
Contact angle hysteresis	23°	3°
Sliding angle (10 μl drop size)	Pinned	6°
Temperature coefficient of resistance at 4.1 wt% (mΩ/K)	4.4	–
CNT loading (wt%)	0.5–4.5	–

in harsh conditions, combined with linear response and NCT makes this an attractive nanocomposite for use where temperature sensing is required.

Table 2 summarizes the key results of this study and shows the static contact angle, contact angle hysteresis, sliding angle (for 10 μl drop), and the temperature coefficient of resistance for PD15L15-20 MWCNT product. Table 1 summarizes the characteristics of the four MWCNT products used in this study and shows a comparison of their resistivity at a loading of 1 wt% MWCNT.

4. Conclusions

In conclusion, we report a novel MWCNT conductive nanocomposite with microtexture surface. The conductive properties of the nanocomposite have been analyzed and demonstrate a huge increase in conductivity of more than 10^{11} with low bulk loading of <5 wt% MWCNT. We have also demonstrated the superhydrophobic properties and report an advancing contact angle of 161°. We also demonstrate a linear negative temperature coefficient of resistance (0.00143) with an operating range of -15°C to 165°C . This combined behavior of a conductive, superhydrophobic nanocomposite and linear temperature coefficient of resistance has exciting applications for allowing a new class of enclosures providing EMI shielding, water repellency and sensing to provide built-in temperature feedback.

Acknowledgements

We acknowledge the NSF PF-AIR and iUCRC programs for the financial support of the research. Also, we acknowledge the support from Virginia Innovation Partnership (VIP) i6 and NASA Langley Professor Programs.

References

- [1] D.M. Bigg, The effect of compounding on the conductive properties of EMI shielding compounds, *Advances in Polymer Technology* 4 (1984) 255–266.
- [2] Federal Communications Commission Title 47 – Telecommunication (Part 15-2009). Available: <http://www.gpo.gov/fdsys/pkg/CFR-2009-title47-vol1/pdf/CFR-2009-title47-vol1-part15.pdf> (accessed: 03.07.14).
- [3] J.T. Hoback, J.J. Reilly, Conductive coatings for EMI shielding, *Journal of Elastomers and Plastics* 20 (1988) 54–60.
- [4] J. Huang, EMI shielding plastics: a review, *Advances in Polymer Technology* 14 (1995) 137–150.
- [5] Y. Yang, M.C. Gupta, K.L. Dudley, R.W. Lawrence, Conductive carbon nanofiber-polymer foam structures, *Advanced Materials* 17 (2005) 1999–2003.
- [6] Y. Yang, M.C. Gupta, K.L. Dudley, R.W. Lawrence, Novel carbon nanotube-polystyrene foam composites for electromagnetic interference shielding, *Nano Letters* 5 (2005) 2131–2134.
- [7] Y. Yang, M.C. Gupta, K.L. Dudley, R.W. Lawrence, The fabrication and electrical properties of carbon nanofiber-polystyrene composites, *Nanotechnology* 15 (2004) 1545–1548.
- [8] D. Qian, E.C. Dickey, R. Andrews, T. Rantell, Load transfer and deformation mechanisms in carbon nanotube-polystyrene composites, *Applied Physics Letters* 76 (2000) 2868–2870.
- [9] C.-F. Wang, W.-Y. Chen, H.-Z. Cheng, S.-L. Fu, Pressure-proof superhydrophobic films from flexible carbon nanotube/polymer coatings, *The Journal of Physical Chemistry C* 114 (2010) 15607–15611.
- [10] C.-F. Wang, S.-J. Lin, Robust superhydrophobic/superoleophobic sponge for effective continuous absorption and expulsion of oil pollutants from water, *ACS Applied Materials & Interfaces* 5 (2013) 8861–8864.
- [11] S.S. Madaeni, S. Zinadini, V. Vatanpour, Preparation of superhydrophobic nanofiltration membrane by embedding multiwalled carbon nanotube and polydimethylsiloxane in pores of microfiltration membrane, *Separation and Purification Technology* 111 (2013) 98–107.
- [12] L.Z. Hao, W.L. Liu, L.D. Zhang, J.S. Yao, W.H. Xu, X.Q. Wang, Y.Z. Wu, Fabrication of superhydrophobic and conductive surface based on carbon nanotubes, *Colloids and Surfaces A: Physicochemical and Engineering Aspects* 423 (2013) 69–76.
- [13] S. Taleaemashadi, M. Sansotera, C. Gambarotti, A. Famulari, C.L. Bianchi, P. Antonio Guardia, W. Navarini, Functionalization of multi-walled carbon nanotubes with perfluoropolyether peroxide to produce superhydrophobic properties, *Carbon* 50 (2013) 150–159.
- [14] I.S. Bayer, A. Steele, E. Loth, Superhydrophobic and electroconductive carbon nanotube-fluorinated acrylic copolymer nanocomposites from emulsions, *Chemical Engineering Journal* 221 (2013) 522–530.
- [15] H. Yao, C.-C. Chu, H.-J. Sae, R. Nishimura, Electrically conductive superhydrophobic octadecylamine-functionalized multiwall carbon nanotube films, *Carbon* 53 (2013) 366–373.
- [16] S.-H. Park, E.-H. Cho, J. Sohn, P. Theilmann, K. Chu, S. Lee, Y. Sohn, D. Kim, B. Kim, Design of multi-functional dual hole patterned carbon nanotube composites with superhydrophobicity and durability, *Nano Research* 6 (2013) 389–398.
- [17] Y.H. Hou, M.Q. Zhang, M.Z. Rong, Performance stabilization of conductive polymer composites, *Journal of Applied Polymer Science* 89 (2003) 2438–2445.
- [18] J.A. Becker, C.B. Green, G.L. Pearson, Properties and uses of thermistors—thermally sensitive resistors, *Transactions of the American Institute of Electrical Engineers* 65 (1946) 711–725.
- [19] Y. Luo, X. Liu, High temperature NTC BaTiO₃-based ceramic resistors, *Materials Letters* 59 (2005) 3881–3884.
- [20] J.D. Plummer, M.D. Deal, P.B. Griffin, *Silicon VLSI Technology: Fundamentals, Practice and Modeling*, Prentice Hall PTR, 2000.
- [21] J.-H. Lee, S.K. Kim, N.H. Kim, Effects of the addition of multi-walled carbon nanotubes on the positive temperature characteristics of carbon-black-filled high-density polyethylene nanocomposites, *Scripta Materialia* 55 (2006) 1119–1122.
- [22] C. Zhang, C.-A. Ma, P. Wang, M. Sumita, Temperature dependence of electrical resistivity for carbon black filled ultra-high molecular weight polyethylene composites prepared by hot compaction, *Carbon* 43 (2005) 2544–2553.
- [23] M.V. Kunnavaikkam, F.M. Houllhan, M. Schiav, J.A. Liddle, P. Kolodner, O. Nalamasu, J.A. Rogers, Low-cost, low-loss microcavities arrays fabricated by soft-lithography replication process, *Applied Physics Letters* 82 (2003) 1152–1154.
- [24] Dow Corning Sylgard® 184 Silicone Elastomer Available: <http://www4.dowcorning.com/DataFiles/090007c8803bb6a1.pdf> (accessed: 03.16.14).
- [25] Y. Maniwa, R. Fujiwara, H. Kira, H. You, E. Nishibori, M. Takata, M. Sakata, A. Fujiwara, X. Zhao, S. Iijima, Y. Ando, Multiwalled carbon nanotubes grown in hydrogen atmosphere: an X-ray diffraction study, *Physical Review B* 64 (2001) 073105.
- [26] C. Li, T.-W. Chou, Axial and radial thermal expansions of single-walled carbon nanotubes, *Physical Review B* 71 (2005) 235414.
- [27] R.S. Ruoff, D.C. Lorents, Mechanical and thermal properties of carbon nanotubes, *Carbon* 33 (1995) 925–930.
- [28] C. Wei, D. Srivastava, K. Cho, Thermal expansion and diffusion coefficients of carbon nanotube-polymer composites, *Nano Letters* 2 (2002) 647–650.
- [29] X.-S. Yi, G. Wu, D. Ma, Property balancing for polyethylene-based carbon black-filled conductive composites, *Journal of Applied Polymer Science* 67 (1998) 131–138.
- [30] X.-S. Yi, G. Wu, Y. Pan, Properties and applications of filled conductive polymer composites, *Polymer International* 44 (1997) 117–124.
- [31] C. Liu, Recent developments in polymer MEMS, *Advanced Materials* 19 (2007) 3783–3790.

- [32] J.C. McDonald, G.M. Whitesides, Poly(dimethylsiloxane) as a material for fabricating microfluidic devices, *Accounts of Chemical Research* 35 (2002) 491–499.
- [33] J. Engel, J. Chen, C. Nannan, S. Pandya, L. Chang, Multi-walled carbon nanotube filled conductive elastomers: materials and application to micro transducers, *Micro Electro Mechanical Systems, 2006. MEMS 2006 Istanbul. 19th IEEE International Conference on*, 2006, pp. 246–249.
- [34] L. Chao-Xuan, C. Jin-Woo, Patterning conductive PDMS nanocomposite in an elastomer using microcontact printing, *Journal of Micromechanics and Micro-engineering* 19 (2009) 085019.
- [35] B.K. Nayak, P.O. Caffrey, C.R. Speck, M.C. Gupta, Superhydrophobic surfaces by replication of micro/nano-structures fabricated by ultrafast-laser-microtexturing, *Applied Surface Science* 266 (2013) 27–32.
- [36] P.O. Caffrey, B.K. Nayak, M.C. Gupta, Ultrafast laser-induced microstructure/nanostructure replication and optical properties, *Applied Optics* 51 (2012) 604–609.
- [37] C. Luo, X. Zuo, L. Wang, E. Wang, S. Song, J. Wang, J. Wang, C. Fan, Y. Cao, Flexible carbon nanotube – polymer composite films with high conductivity and superhydrophobicity made by solution process, *Nano Letters* 8 (2008) 4454–4458.
- [38] K. Mauritz, R. Moore, State of understanding of nafion, *Chemical Reviews* 104 (2004) 4535–4585.
- [39] Nafion: LQ-1105 – 1100 EW at 5% weight, Ion Power Inc., Available: http://www.nafionstore.com/LQ_1105_g/lq-1105.htm (accessed 16.03.14).
- [40] Dow Corning Sylgard 182 Silicone Encapsulant, Elsworth Adhesives Inc., Available: <http://www.elsworth.com/dow-corning-sylgard-182-silicone-encapsulant-0-5kg-ldt-clear> (accessed: 16.03.14).
- [41] B.K. Nayak, M.C. Gupta, K.W. Kolasinski, Spontaneous formation of nanospliked microstructures in germanium by femtosecond laser irradiation, *Nanotechnology* 18 (2007) 195302.
- [42] B.K. Nayak, M.C. Gupta, K.W. Kolasinski, Formation of nano-textured conical microstructures in titanium metal surface by femtosecond laser irradiation, *Applied Physics A: Materials Science & Processing* 90 (2008) 399–402.
- [43] B.K. Nayak, M.C. Gupta, Self-organized micro/nano structures in metal surfaces by ultrafast laser irradiation, *Optics and Lasers in Engineering* 48 (2010) 940–949.
- [44] Keithley Model 6105 Resistivity Adapter Instruction Manual, Keithley Instruments Inc., 2009.
- [45] ASTM Standard D257, 2007, Standard Test Methods for DC Resistance or Conductance of Insulating Materials, ASTM, International, West Conshohocken, PA, 2007.
- [46] ASTM Standard D7334, 2008, Standard Practice for Surface Wettability of Coatings, Substrates and Pigments by Advancing Contact Angle Measurement, ASTM, International, West Conshohocken, PA, 2008.
- [47] W. Rasband, ImageJ, Research Services Branch, National Institute of Mental Health, 2011.
- [48] A.F. Stalder, G. Kulik, D. Sage, I. Barbieri, P. Hoffmann, A snake-based approach to accurate determination of both contact points and contact angles, *Colloids and Surfaces A: Physicochemical and Engineering Aspects* 286 (2006) 92–103.
- [49] Y.Y. Wang, G.Y. Tang, F.A.M. Koock, B. Brown, J.M. Garguilo, R.J. Nemanich, Experimental studies of the formation process and morphologies of carbon nanotubes with bamboo mode structures, *Diamond and Related Materials* 13 (2004) 1287–1291.
- [50] B.G. Sumpter, V. Meunier, J.M. Romo-Herrera, E. Cruz-Silva, D.A. Cullen, H. Terrones, D.J. Smith, M. Terrones, Nitrogen-mediated carbon nanotube growth: diameter reduction, metallicity, bundle dispersability, and bamboo-like structure formation, *ACS Nano* 1 (2007) 369–375.
- [51] Nanolab Inc, Multiwall Carbon Nanotubes, Available: <http://www.nano-lab.com/nanotubes-research-grade.html> (accessed: 10.03.14).